REPORT DOCUMENTATION PAGE

Public reporting burden for this collection of information is estimated to average 1 hour per response, including the time for reviewing instructions, searching existing data sources, gathering and maintaining the data needed, and completing and reviewing the collection of information. Send comments regarding this burden estimate or any other aspect of this collection of information, including suggestions for reducing this burden, to Washington Headquarters Services, Directorate for Information Operations and Reports, 1215 Jefferson Davis Highway, Suite 1204, Arlington, VA 22202-4302, and to the Office of Management and Budget, Paperwork Reduction Project (0704-0188), Washington, DC 20503.

1. AGENCY USE ONLY (Leave blank)	2. REPORT DATE Aug 1995	3. REPORT TYPE AND DATES COVERED

4. TITLE AND SUBTITLE

Diagnostic Developments for Velocity and Temperature Measurenments in Uni-Element Rocket Environments

5. FUNDING NUMBERS

6. AUTHOR(S)

Kenneth D. Philippart

7. PERFORMING ORGANIZATION NAME(S) AND ADDRESS(ES)

AFIT Students Attending:

The Pennsylvania State University — The Graduate School

8. PERFORMING ORGANIZATION REPORT NUMBER

9. SPONSORING/MONITORING AGENCY NAME(S) AND ADDRESS(ES)

DEPARTMENT OF THE AIR FORCE
AFIT/CI
2950 P STREET, BLDG 125
WRIGHT-PATTERSON AFB OH 45433-7765

10. SPONSORING/MONITORING AGENCY REPORT NUMBER

AFIT/CI/CIA
95-73

11. SUPPLEMENTARY NOTES

12a. DISTRIBUTION/AVAILABILITY STATEMENT

Approved for Public Release IAW AFR 190-1
Distribution Unlimited
BRIAN D. Gauthier, MSgt, USAF
Chief Administration

12b. DISTRIBUTION CODE

13. ABSTRACT (Maximum 200 words)

DTIC
SELECTED
SEP 13 1995
B

19950912 004

14. SUBJECT TERMS

15. NUMBER OF PAGES
114

16. PRICE CODE

17. SECURITY CLASSIFICATION OF REPORT	18. SECURITY CLASSIFICATION OF THIS PAGE	19. SECURITY CLASSIFICATION OF ABSTRACT	20. LIMITATION OF ABSTRACT

DTIC QUALITY INSPECTED 1

The Pennsylvania State University

The Graduate School

Department of Aerospace Engineering

DIAGNOSTIC DEVELOPMENTS FOR VELOCITY AND TEMPERATURE

MEASUREMENTS IN UNI-ELEMENT ROCKET ENVIRONMENTS

A Thesis in

Aerospace Engineering

by

Kenneth D. Philippart

Submitted in Partial Fulfillment
of the Requirements
of the Degree of

Master of Science

August 1995

I grant The Pennsylvania State University the nonexclusive right to use this work for the University's own purposes and to make single copies of the work available to the public on a not-for-profit basis if copies are not otherwise available.

Kenneth D. Philippart

We approve the thesis of Kenneth D. Philippart.

Date of Signature

Robert J. Santoro
Professor of Mechanical Engineering
Thesis Adviser

July 18, 1995

Thomas A. Litzinger
Associate Professor of
   Mechanical Engineering

18 July 1995

Dennis K. McLaughlin
Professor of Aerospace Engineering
Head of the Department of
   Aerospace Engineering

20 July 95

ABSTRACT

Velocity and temperature measurements were taken within a uni-element rocket combustion chamber for hydrogen-oxygen propellants using laser Doppler velocimetry, thermocouples, and a thermocouple-based temperature rake developed for this effort.

Velocity and turbulence profiles were obtained for firings with a gaseous oxygen (GO_2)/gaseous hydrogen (GH_2) coaxial shear injector at axial locations of 1.6 mm (0.063 in.), 6.4 mm (0.25 in.), 12.7 mm (0.5 in.), 25.4 mm (1 in.) and 50.8 mm (2 in.).

Significant effort went into attempting to reproduce earlier data. Hot-firings confirmed the qualitative behavior and profile shapes reported earlier at the 25.4 mm (1 in.) and 50.8 mm (2 in.) axial locations but could not repeat the velocity magnitudes. In general, the maximum velocities reported in this work were 10 to 20 percent lower than the values reported previously for the same positions.

Aluminum oxide particles of various sizes seeded the flow in an attempt to explain the discrepancies. While cold-flow simulations were promising, hot-fire results for the various particles were virtually identical and still lower than earlier data. The hot-firings were self-consistent and question the reproducibility of the previous data.

Velocity bias was examined. Time-weighted average and constant time interval correction methods were inconclusive. The data sets did not appear suited for the schemes. An argument was made that the data from this effort was less biased than the earlier work due to the higher signal-to-noise ratio (SNR) criterion.

Velocity measurements were made closer to the injector than the preceding work. Asymmetries were noted in all profiles. The shear layer displayed high turbulence levels. The central flow near the injector resembled turbulent pipe flow. Recirculation zones existed at the chamber walls and became smaller as the flow evolved downstream. The combusting flow region expanded with increasing axial distance.

A thermocouple-instrumented coaxial injector was fired with GO_2/GH_2 propellants. The injector exit plane boundary conditions were determined.

The feasibility of a thermocouple-based temperature rake was established. Tests at three axial positions for air/GH_2 firings revealed asymmetric profiles. Temperatures increased with increasing axial distance. The temperature profiles agreed qualitatively with Raman measurements at the same hot-fire conditions.

The probe experienced difficulty for a liquid oxygen/GH_2 swirl coaxial injector. The water coolant froze during the prefire cool-down phase and the rake only reached steady-state temperatures for a small portion of the firing. The results at the 76.2 mm (3 in) axial location were comparable to the air/GH_2 tests.

The rake was reconfigured for nitrogen cooling in a high mass flow LOX firing. The probe was destroyed and no temperature profile taken. Analysis suggested the probe did not overheat globally but was consumed when the thermocouple tips ignited and burned through the rake wall due to the extremely oxygen-rich environment.

TABLE OF CONTENTS

LIST OF FIGURES

LIST OF TABLES

NOMENCLATURE

Symbol	Description
A_1	Cross sectional area of thermocouple sheath
A_2	Cross sectional area of radiating surface
Al_2O_3	Aluminum oxide
CFD	Computational fluid dynamics
d	Beam separation distance
d	Diameter
d_f	Fringe spacing
f	Focal length
Fe_2O_3	Iron oxide
GH_2	Gaseous hydrogen
GN_2	Gaseous nitrogen
GO_2	Gaseous oxygen
h	Convection heat-transfer coefficient
k	Thermal conductivity
LDV	Laser Doppler velocimetry
LOX	Liquid oxygen
$\dot{m}$	Mass flow rate
N	Number of samples
PDPA	Phase Doppler particle analyzer

Pr	Prandtl number
r	Radius
r_0	Reference radius
Re_d	Reynolds number based on diameter
RMS	Root mean square
SiO_2	Silicon dioxide
SNR	Signal to noise ratio
t	Time
T	Temperature
TBD	Time between data points
TiO_2	Titanium dioxide
T_{tc}	Thermocouple temperature
T_∞	Free stream temperature
u	Velocity
u_{mean}	Mean axial velocity of LDV realizations
u_{rms}	Root mean square velocity of LDV realizations
u_∞	Free stream velocity
$\bar{u}$	Mean pipe flow velocity
U_{CL}	Centerline pipe flow velocity
z	Axial distance
Δt	Time interval

Δx Thermocouple length

Greeks

ε Emissivity

ϕ Half the beam crossing angle

λ Wavelength

μm Microns

ν_D Doppler frequency

ν_f Kinematic viscosity of fluid

σ Stefan-Boltzmann constant

ACKNOWLEDGMENTS

Chapter 1

INTRODUCTION

Motivation

It is one of the harshest environments imaginable: searing temperatures hot enough for steel to run like water; crushing pressures hundreds of times greater than the Earth's atmosphere; volatile chemicals caustically eating away at whatever they touch; gale-force winds howling with tremendous force, scouring everything in their path; violent, unpredictable outbursts of incredible energy capable of wreaking destruction. This is no scene from Dante's *Inferno*. Such conditions routinely exist in rocket combustion chambers.

Understanding these extremely harsh and complex environments is fraught with difficulty. The history of rocketry is replete with spectacular failures illustrating the lack of understanding of the complex interactions within a rocket engine. Of necessity, failures were often handled with assumptions and trial-and-error corrections as if the designers were making sacrifices of money and material to appease the rocketry gods.

Much was accomplished with this practical, empirical approach. Men ventured into space and onward to the Moon. Communications and weather satellites transformed the world. Long-range ballistic weapons revolutionized warfare. Along the way, bits of knowledge were gleaned about vexing issues of balancing high performance with stable combustion and reliability. Successes were many, but so were failures and each failure required an infusion of human and economic resources to overcome.

The rocket industry can no longer afford the expensive, time-consuming, labor-intensive "make it and break it" approach of the past. The watchwords for today are "faster, better, cheaper," a design philosophy which requires fundamental understanding of complex processes [1]. Fortunately, the confluence of high-speed computers and sophisticated laser-based diagnostics have made this vision practical.

Some tools are already available to the rocket designer. Computer codes such as FLUENT [2], SDER [3] and ROCCID [4] are useful, but are limited in their modeling of physical mechanisms.

Comprehensive computational fluid dynamic (CFD) models incorporating detailed descriptions of flowfield processes are under development [5, 6]. However, model development is inhibited by the lack of a comprehensive data base for code validation [7]. Experimental data including temperatures, velocities, and species concentrations at rocket combustion conditions are needed to validate CFD codes.

The same severe environment within a rocket combustion chamber that makes modeling imperative also complicates data collection. Intrusive measurements are difficult and of limited applicability at the elevated temperatures, pressures, heat transfer rates and turbulence levels typical of rocket combustors. Nonintrusive laser diagnostics promise to complement traditional techniques and expand the experimental data base dramatically.

Toward this end, research has been conducted at the Pennsylvania State University (PSU) Propulsion Engineering Research Center [8, 9, 10, 11]. Building upon previous work,

additional testing was conducted to expand the data base for CFD code validation. This treatise is the result.

Objectives

The objectives of the research effort were to:

1. examine the reproducibility of laser Doppler velocimetry (LDV) measurements within the PSU Cryogenic Combustion Laboratory's optically-accessible rocket chamber for a uni-element shear coaxial injector with gaseous oxygen (GO_2) and gaseous hydrogen (GH_2) propellants.

2. extend the LDV velocity measurements to axial locations in the near-injector region.

3. measure the temperature boundary conditions for the uni-element injector exit plane.

4. determine the feasibility of making temperature measurements within the uni-element rocket combustor with a thermocouple-based rake for comparison with measurements derived from laser-based techniques. Design and construct a temperature rake.

5. measure radial temperature distributions with the rake at various axial locations for both gas/gas shear coaxial and gas/liquid swirl coaxial injector elements.

6. gain insight into the combusting flowfields from the velocity and temperature data.

Background

Previous Work

The velocity measurements were a continuation of the work begun by Merenich [9]. Merenich measured axial and root mean square (RMS) velocities within the rocket combustor at positions 25.4 mm (1 in.), 50.8 mm (2 in.), and 127 mm (3 in.) downstream of the coaxial injector exit plane. It was desired to examine the reproducibility of these data and to measure velocities upstream in the near-injector region.

Thermocouple-based temperature rake measurements had not been conducted in the PSU rocket chamber prior to this work. Thermocouples have been used for decades to measure temperatures in combustors [12, 13] but had never been used in the uni-element rocket chamber at PSU. It was hoped such a temperature probe could ultimately complement non-intrusive temperature measurements conducted by other researchers.

Laser Doppler Velocimetry

Laser Doppler velocimetry (LDV) or laser Doppler anemometry, is a relatively mature diagnostic technique. The earliest use of LDV in fluid mechanics was by Yeh and Cummins in 1964 [14]. Since then much progress has been made in designing improved optical geometries, pre-aligned systems, signal processing equipment, and application strategies. Because of the mature state-of-the art of LDV, only a brief description of the technique will be given.

Basic laws of optics govern the operation of a LDV system. In a dual-beam LDV device, a splitter divides the source laser beam into two equal intensity beams. The split beams are spaced a distance, d, apart and are parallel to the optical axis of a spherical diffraction-limited lens. The beams pass through the lens and are brought to a focus. When the beams intersect, an interference pattern is formed due to the principle of superposition. The system is aligned so that the probe volume formed by the interference region lies in the fluid flow area for which measurements are to be made. When fluid passes through the probe volume, light is scattered from naturally-occurring or artificially-introduced particles within the flow. The light intensity will be maximum when the particle crosses a peak in the fringe pattern and minimum when the particle crosses a trough. The scattered light is collected by a photodetector where fluctuations in light intensity are revealed as voltage fluctuations. By measuring the time between light intensity maxima, the particle velocity component normal to the plane of the fringe pattern can be determined from:

$$u_i = \frac{d_f}{\Delta t}$$
Eq. 1

where u_i is the particle velocity, d_f is the fringe spacing, and Δt is the time between maxima. The fringe spacing is fixed by the wavelength of the laser light and the beam crossing angle:

$$d_f = \frac{\lambda}{2 \sin \phi}$$
Eq. 2

where λ is the wavelength of the laser light and ϕ is half the beam crossing angle.

Combining the previous equations yields:

$$u_i = \frac{\lambda}{2 \Delta t \sin \phi} = \frac{\lambda \nu_D}{2 \sin \phi}$$
Eq. 3

where $v_D = \Delta t^{-1}$ is called the Doppler frequency of the fluctuating scattered light signal.

If the focusing lens is optically thin, half the beam angle can be found from:

$$\phi = \tan^{-1}\left(\frac{d}{2f}\right)$$ Eq. 4

where d = spacing of the split beams and f = focal length of the lens [14, 15].

Thus, the particle velocity can be measured by knowing the wavelength of the light and the geometric parameters of the optical system and by measuring the Doppler frequency of the scattered light signal.

LDV is prone to several types of biasing which affect the validity of the measurements. Directional bias in which the flow direction is ambiguous can result since the equations say nothing about the direction the particle is moving. Density bias can result when density changes or mixing of two flows changes the particle concentration within the fluid volume to be measured. Combustion introduces additional light and can overwhelm the scattered light signals. Fortunately, most biases are eliminated by tailoring the optics, shifting the beam frequencies, or electronic processing of the signals [16]. An exception is velocity bias which results from a correlation between the particle velocity and sampling rate. Velocity bias is not easily eliminated. Attempts have frequently centered upon post-processing the data to correct for the bias (Chapter 3).

Signal processing of the light scattered from the seed particles in the flow can be very involved. The reader is referred to Durst, Melling and Whitelaw [14] along with Faeth [15] for a detailed discussion of the intricacies of signal processing and the impact on LDV measurements.

Chapter 2

EXPERIMENTAL APPARATUS AND APPROACH

Test Facility

Hot-firings were conducted at the PSU Cryogenic Combustion Laboratory. The Cryogenic Laboratory's development and capabilities have been thoroughly documented elsewhere [8, 9, 10,11]. Thus, a brief description will suffice.

The Cryogenic Combustion Laboratory consists of a control room, an instrumentation room, a test cell, and a propellant storage area. Hot-firings are remotely controlled from the control room which contains the test control panel, equipment racks, and data acquisition computers. The instrumentation room houses the lasers and other equipment which do not require immediate proximity to the test chamber. Access to the optically-accessible rocket chamber in the test cell is via two ports containing optical windows. The test cell is a three-sided reinforced concrete room with a large overhead door that is opened during test firings. The rocket chamber is oriented to direct the exhaust out of the test cell through the open door toward a protective earthen embankment.

Propellants are fed into the test cell from banks of high pressure gas bottles in the propellant storage area. The maximum mass flow rates of the facility are 0.045 kg/sec (0.1 lb/sec) for GO_2, 0.45 kg/sec (1.0 lb/sec) for liquid oxygen (LOX), and 0.11 kg/sec (0.25 lb/sec) for the fuel, typically GH_2 [11].

Optically-Accessible Rocket Chamber

The optically-accessible chamber has also been thoroughly documented by others [8, 9, 10, 11]. The rocket chamber is modular and can be easily configured to provide optical access along the chamber length (Fig. 1). The chamber consists of an injector assembly, igniter, window and blank sections and a nozzle assembly. The window section permits optical access into the chamber for laser-based diagnostics. Two diametrically-opposed quartz windows of 50.8 mm (2 in) diameter and 25.4 mm (1 in) thickness provide optical access into the chamber. The windows are protected from the hot combustion gases by a gaseous nitrogen (GN_2) purge which flows across the interior surfaces. The slot windows can be replaced by special blanks with fittings to insert a temperature rake across the 50.8 mm x 50.8 mm (2 in. x 2 in.) square chamber. The optical and slot window blank section can be repositioned downstream of the injector exit plane to allow measurements at different axial stations.

The injector assembly can be replaced with various configurations (Fig. 2). The velocity measurements and gas/gas temperature measurements utilized a uni-element shear coaxial injector. The LOX/GH_2 temperature measurements were made with two swirl coaxial injectors of different LOX mass flow capacities. Table 1 lists the injector dimensions.
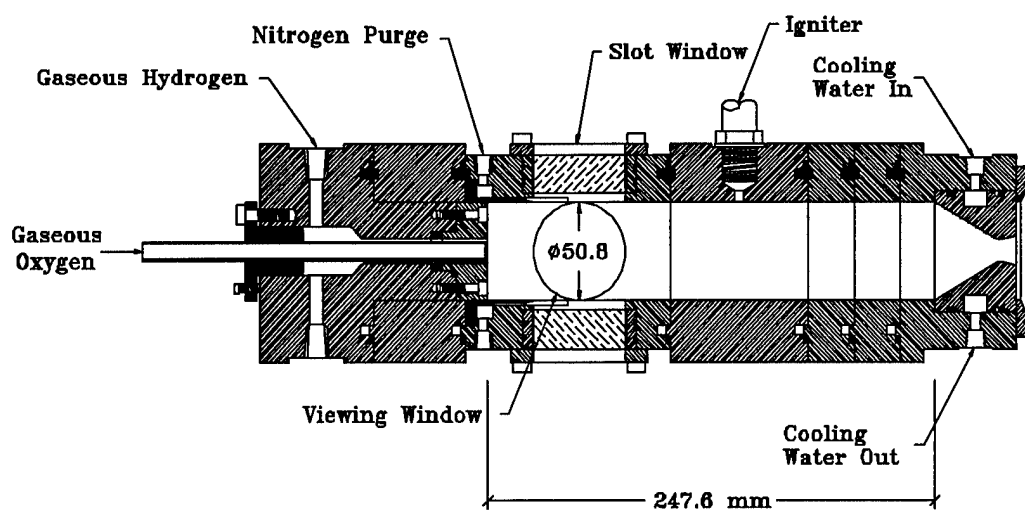
Fig. 1: Cross-Sectional View of the Optically-Accessible Rocket Chamber

Hydrogen

Oxygen

Hydrogen

Shear Coaxial Injector

LOX
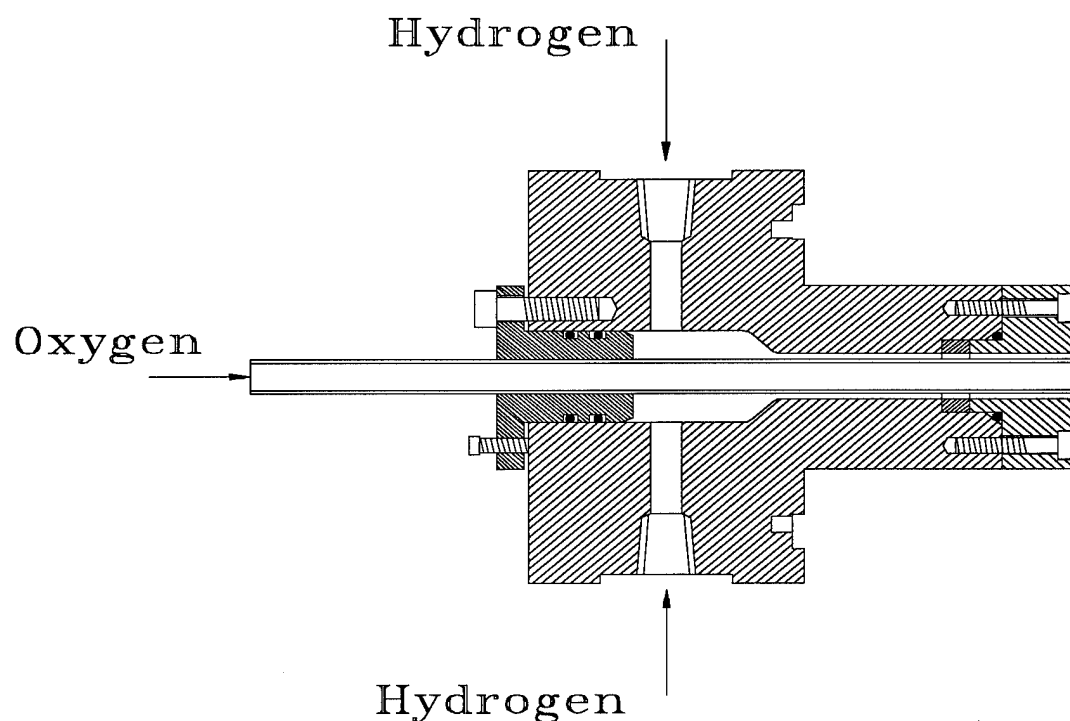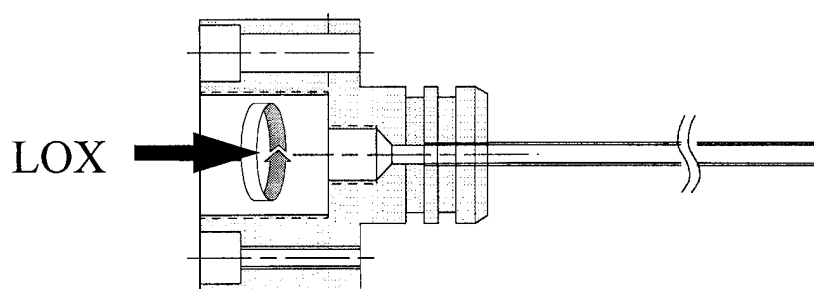
Swirl Coaxial Oxidizer Post
(replaces center post above)

Fig. 2: Cross-Sectional Views of the Shear and Swirl Coaxial Injectors

Table 1: Injector Dimensions

	shear coaxial	swirl coaxial (low $\dot{m}$)	swirl coaxial (high $\dot{m}$)
oxidizer post ID	7.75 mm (0.305 in.)	3.43 mm (0.135 in.)	7.04 mm (0.277 in.)
fuel annulus ID	9.53 mm (0.375 in.)	4.19 mm (0.165 in.)	9.53 mm (0.375 in.)
fuel annulus OD	12.7 mm (0.5 in)	7.11 mm (0.280 in.)	10.74 mm (0.423 in.)
oxidizer post recess	0.0 mm	0.0 mm	0.0 mm

Test Conditions

The rocket firing control sequence was identical to that of Merenich, Moser, et al. [8, 9, 10, 11]. The rocket was fired for 4 seconds, a time selected as a compromise between quartz window survivability and the time required to reach steady-state conditions. Velocity measurements were taken for 2.5 seconds after the chamber reached steady-state pressure whereas temperature rake measurements were taken throughout the entire firing to record ignition and shutdown temperatures. Nominal flow conditions for the various hot-firings are listed in Table 2.

Velocity Measurements

A major thrust of this research was to obtain radial distributions of axial velocity within the chamber flowfield through LDV.

Table 2: Nominal Conditions for Various Rocket Hot-Firings

	GO_2/GH_2	air/GH_2	LOX/GH_2 (low $\dot{m}$)	LOX/GH_2 (high $\dot{m}$)
GH_2 mass flow kg/s (lb/s)	0.0103 (0.0226)	0.0036 (0.0079)	0.0007 (.0015)	0.0045 (0.0100)
Oxidizer mass flow kg/s (lb/s)	0.0387 (0.0852)	0.0591 (0.1303)	0.1133(0.2500)	0.4536 (1.000)
O/F	3.8	16.6	166.0	100.0
GN_2 mass flow (purge) kg/s (lb/s)	0.0134 (0.0295)	0.0146 (0.0322)	N/A	0.0218 (0.0481)
GH_2 injection velocity m/s (ft/s)	184.6 (605.6)	54.8 (179.9)	16.9 (55.4)	101.0 (331.4)
Oxidizer injection vel m/s (ft/s)	52.8 (173.1)	72.4 (237.6)	12.3 (40.4)	10.2 (33.5)
Chamber pressure MPa (psia)	1.27 (186)	1.43 (207)	2.08 (302)	2.86 (415)

Phase Doppler Particle Analyzer

Velocities were measured using the Aerometrics Phase Doppler Particle Analyzer (PDPA) LDV system [17]. The PDPA can measure two components of velocity and the size of spherical particles traversing the probe volume. In this effort, the instrument measured the flowfield axial velocity only.

Figure 3 illustrates the experimental setup. The probe volume was formed in the chamber by splitting an argon ion laser beam of wavelength 514.5 nm into two beams. The intersection of the beams produced the probe volume. One beam was frequency shifted by 40 MHz with a Bragg cell to eliminate directional ambiguity. The transmitting
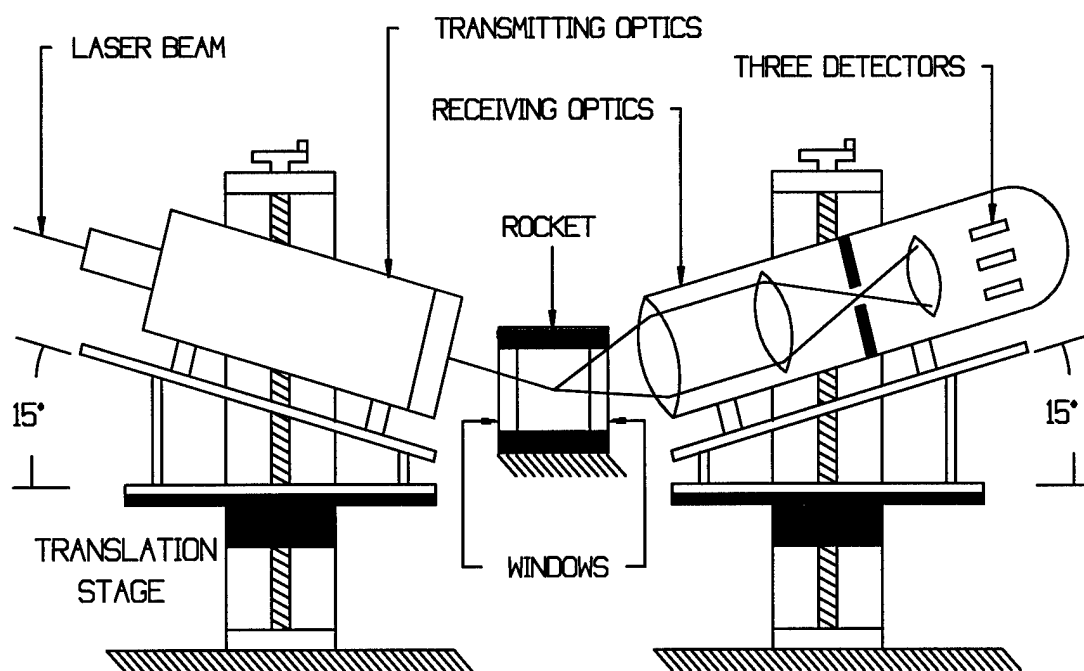
Fig. 3: Phase Doppler Particle Analyzer Configuration

and receiving optics were canted 15 degrees from horizontal to minimize reflections from the quartz viewing windows. The optics were mounted on translation stages to move the probe volume radially within the chamber. However, the cant limited the distance the probe volume could traverse in the upward as compared to the downward direction.

Flow Seeding

The LDV technique requires particles to pass through the probe volume to measure the flow velocity. Separate fluidized bed seeders in the oxidizer and fuel lines introduced the particles into the chamber. A portion of the main propellant flow was diverted into the seeder, flowed through a porous plate upon which the seeding material rested, and entrained seed particles in the gas flow. The particle-laden gas exited the seeder, recombined with the primary propellant flow and entered the combustion chamber (Fig. 4) [8]. An additional remotely-operated valve was added to the seeding system subsequent to Merenich's work to better control the amount of seed entering the chamber. Merenich's firings were characterized by great clouds of seed spewing from the rocket due to the large pressure changes at startup and shutdown. The remote valve was opened only during the steady-state portion of the firing which reduced the seed to lower levels.

The oxidizer and fuel flows were not seeded simultaneously during the same firing to avoid density bias. Density bias occurs when two flows of unequal seeding concentrations mix, resulting in a measuring bias toward the flow with the higher seed density [14,18].
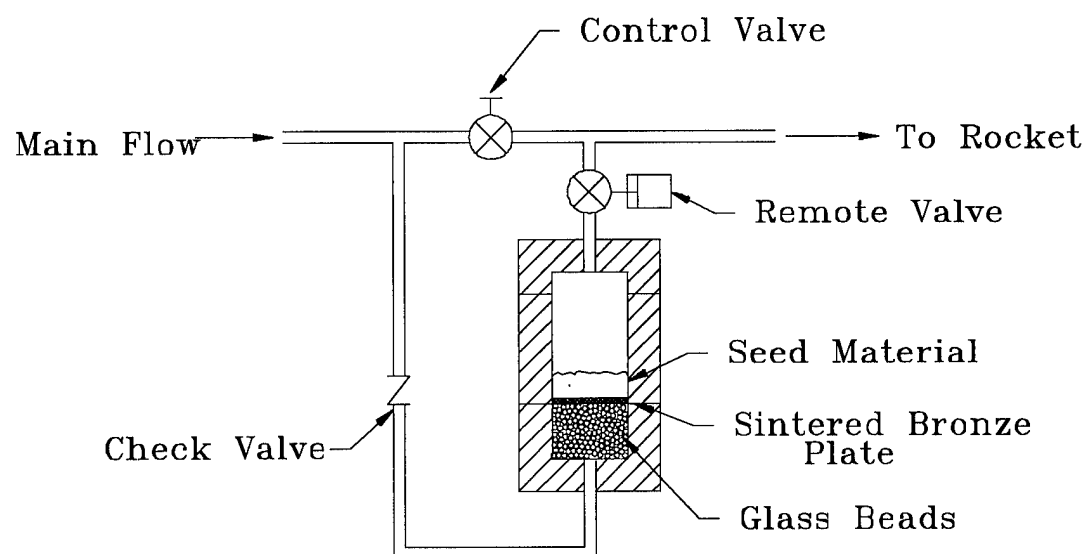
Fig. 4: Fluidized Bed Seeder

The flow was seeded with a commercial-grade aluminum oxide (Al_2O_3) abrasive of nominal diameter 0.3 μm [19]. Numerous factors are involved in selecting a seed material for combusting environments [20, 21, 22,23]. Aluminum oxide was chosen due to its refractory properties, low toxicity, wide-spread availability, and low cost. Particle sizes of 0.1 - 1.0 μm are considered small enough to follow the local gas velocity [24].

When discrepancies arose between the data and the work of Merenich, other sizes of Al_2O_3 were examined in cold-flow tests in an attempt to explain and eliminate apparent discrepancies as discussed in Chapter 3.

Measurement Locations

Velocity profiles were obtained at five axial locations downstream of the injector face. Measurements were taken at the 25.4 mm (1 in.) and 50.8 mm (2 in.) axial locations for comparison with the data from Merenich [9]. In addition, profiles of mean and RMS velocities were obtained 1.6 mm (0.063 in.), 6.4 mm (0.25 in.) and 12.7 mm (0.50 in.) downstream of the injector. Extension of the velocity measurements to the near-injector region was a significant accomplishment of this effort since previous work measured velocities no closer than one inch to the injector plane.

Measurements were performed by individually and non-simultaneously seeding the hydrogen and oxygen flows and traversing the probe volume vertically across the rocket chamber between firings. Typically, measurements were taken at radial increments of 0.508 mm (0.020 in.) or 0.635 mm (.025 in.) but smaller steps were taken in regions where greater resolution was desired. The probe volume was traversed radially

toward the chamber walls until velocities could no longer be measured due to geometrical constraints of the windows or insufficient seed particle concentration near the wall.

Temperature Measurements

Another objective was to obtain temperature boundary conditions within the injector flowfield and preliminary temperature distributions within the combustion chamber. The approach was not designed to be nonintrusive. Rather, standard thermocouples measured temperatures for comparison with nonintrusive measurements by other researchers.

Thermocouple-Instrumented Coaxial Injector

A coaxial injector of the type used in the GH_2/GO_2 hot-firings in this and multiple other works was wired with seven Type K, nickel-chromium thermocouples of 0.508 mm (0.020 in.) diameter. Three of the seven thermocouples were grounded and four were bare. Type K thermocouples have a measurement range of 73 to 1523 K [25]. Six thermocouples were situated around the inner and outer periphery of the oxidizer injector tube and one was located within the center (Fig. 5)

The thermocouple leads were plugged into a jack panel connected to an amplifier and LeCroy data acquisition system. An ice bath reference was used to calibrate the thermocouples and voltages were recorded at a frequency of 200 Hz. The thermocouple voltages were converted to temperatures with a FORTRAN routine based on curvefit coefficients for Type K thermocouples [25].
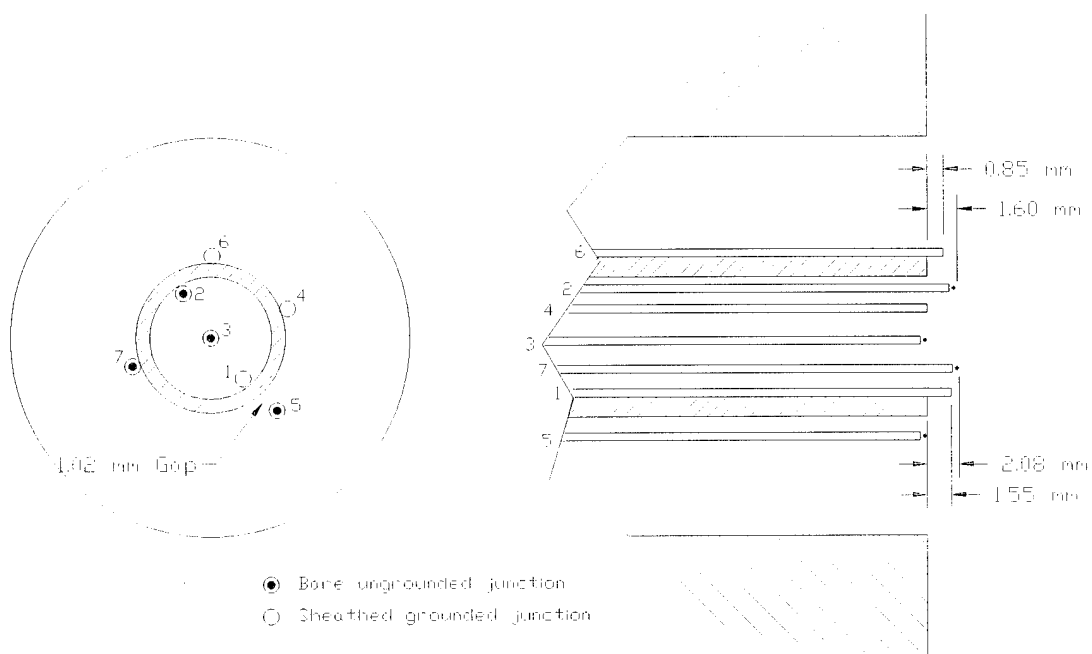
Fig. 5: Location of Type K, 0.508 mm Diameter Thermocouples on Shear Coaxial Injector

Hot-firings were performed with the instrumented injector to further define the exit plane boundary conditions within the injector flowfield.

Temperature Rake

It was desired to examine the feasibility of taking temperature measurements with a simple thermocouple-instrumented probe to enhance understanding of the degree of mixing and combustion at various points within the chamber.

A proof-of-concept prototype rake was constructed. The probe consisted of a 50.8 mm (2 in.) section of 4.76 mm (0.19 in.) outer diameter brass tubing with 6.35 mm (0.25 in.) outer diameter brass tube fittings silver soldered to both ends. Two Type K grounded thermocouples of 0.508 mm (0.020 in.) diameter were routed inside the tube and passed through holes in the wall. The thermocouples protruded beyond the tube wall to lengths of 1.65 mm (0.065 in.) and 2.54 mm (0.10 in.) respectively. Inlet and outlet hoses were attached to the end fittings through which water flowed to cool the probe.

The prototype temperature rake measured radial temperature distributions in a laboratory methane/air flame. Profiles were obtained at positions 10, 40 and 100 mm (0.39, 1.57 and 3.94 in.) above the flame burner.

The temperature rake profiles were compared to profiles from quick-insertion bare-wire thermocouple measurements [26]. The rake closely reproduced the shape of the reference flame profiles including the distance between the bimodal temperature peaks at the 10 and 40 mm (0.39 and 1.57 in.) vertical locations. The peak temperatures recorded were approximately one-fifth to one-third of the reference flame peaks.

A simple heat transfer model was developed to predict the temperatures the thermocouples should have reported within the methane/air reference flame. The model was written using MathCad Version 5.0 [27] and used a simple energy balance in which:

$$E_{conducted} + E_{radiated} + E_{convected} = 0 \qquad \text{Eq. 5}$$

where $E_{conducted}$ = energy conducted *away from* the thermocouple, $E_{radiated}$ = energy radiated *away from* and $E_{convected}$ = energy convected *to* the thermocouple [28]. Using basic conduction, radiation and convection models, Eq. 8 becomes:

$$kA_1 \frac{T_{tc} - T_w}{\Delta x} + \sigma \varepsilon A_2 \left(T_{tc}^4 - T_\infty^4\right) + hA_2\left(T_{tc} - T_\infty\right) = 0 \qquad \text{Eq. 6}$$

where k = thermal conductivity of the thermocouple sheath, A_1 = cross sectional area of the thermocouple sheath, T_{tc} = temperature of the thermocouple, T_w = temperature of the tube wall, Δx = length of the thermocouple, σ = Stefan-Boltzmann constant, ε = emissivity of the sheath material, T_∞ = temperature of the fluid media, h = convection heat-transfer coefficient and A_2 = area of the radiating surface. Thermocouple material properties were taken from Holman [28].

Several assumptions were made in implementing the above equation. The energy conducted by the insulation within the thermocouple was neglected. Radiation was assumed to occur only from the hemispheric thermocouple bead; radiation from the cylindrical shaft was ignored. The wall temperature was assumed to be the temperature of the water coolant. The convection heat-transfer coefficient was based on the model for a sphere in a cross flow for $17 < \text{Re}_d < 70{,}000$ in which:

$$h = 0.37 \frac{k_f}{d} \frac{u_\infty d^{0.6}}{\nu_f}$$ Eq. 7

where d = diameter of the sphere, k_f = thermal conductivity of the fluid medium,

u_∞ = cross flow velocity of the fluid past the sphere, and ν_f = kinematic viscosity of the

fluid [28]. The fluid medium properties were calculated from the CET89 code [29].

The predicted temperatures were compared to the measured peak values. The

measured temperatures were 46 to 66 percent of the values predicted from the simplified

heat transfer model. Agreement was better for the 2.54 mm (0.10 in.) than for the

1.66 mm (0.065 in.) length thermocouple. Given the assumptions and the model's

simplicity, agreement between the predicted and measured temperatures was sufficient to

determine the approximate thermocouple length for balancing resolution with

survivability. It was concluded the rake would be suitable as a measurement device.

An operational temperature rake was constructed based on the prototype. The

operational rake was identical to the prototype with seven rather than two Type K

grounded 0.508 mm (0.020 in.) diameter thermocouples. The thermocouples were spaced

6.35 mm (0.25 in.) apart so that the end thermocouples would be 6.35 mm (0.25 in.) away

from the chamber wall when inserted into the rocket combustion chamber. The

thermocouples protruded 1.5 mm (0.59 in.) beyond the tube wall.

A heat transfer analysis was performed using the FLUENT CFD code to

determine if water flow through the rake could sufficiently cool the probe in the rocket

chamber [2]. The convection heat-transfer coefficient for the cylindrical temperature rake

in a cross flow was calculated from:

$$h = 0.683 \frac{k_f}{d} \left(\frac{u_\infty d}{v_f} \right)^{0.466} Pr^{\frac{1}{3}}$$
Eq. 8

where Pr = Prandtl number and other variables are as before [28].

A probe was fabricated for use in the rocket chamber. Analysis indicated water would sufficiently cool the probe to ensure survival at the anticipated hot-fire conditions. The probe was inserted vertically into the chamber through fittings in the slot window plugs and oriented with the protrusions parallel to the chamber axis. Thermocouples were placed in the water coolant inlet and outlet lines to measure the temperature rise and estimate the heat transfer to the coolant. The thermocouples were connected to an amplifier and LeCroy data acquisition system. Voltages were recorded at 200 Hz and converted to temperatures with a FORTRAN routine.

The rake collected temperature profiles at various axial locations for both gas/gas and gas/liquid propellant combinations.

Chapter 3

RESULTS AND DISCUSSION

Velocity Measurements

25.4 mm (1 in.) Axial Location Hot Firings

The reproducibility of Merenich's data was examined before extending the

chamber velocity measurements upstream of the positions studied by Merenich. The

laser probe volume was positioned 25.4 mm (1 in.) downstream of the injector and

measurements were taken for the flow conditions from the earlier study. Fig. 6 displays

the mean velocities along with those reported by Merenich [9]. The velocities were

calculated by the PDPA software using a straight-forward ensemble average algorithm.

The radial positions were nondimensionalized by the oxidizer post radius

(3.87 mm/0.153 in.).

Measurements were taken from a nondimensional radius of approximately 1.6

(upward) to -1.6 (downward) with the oxygen flow seeded. The peak velocity in the

oxygen-seeded core was 57.2 m/sec (187.7 ft/sec) at a nondimensional radius of -0.08.

Since the central core velocity could be expected to peak at the centerline, the offset may

indicate the error inherent in visually centering the probe volume. The mean velocity

dropped off with increasing radial distance until $r/r_0 = 1.6$ whereupon the velocity

increased, thus revealing the influence of the higher velocity hydrogen outer flow.
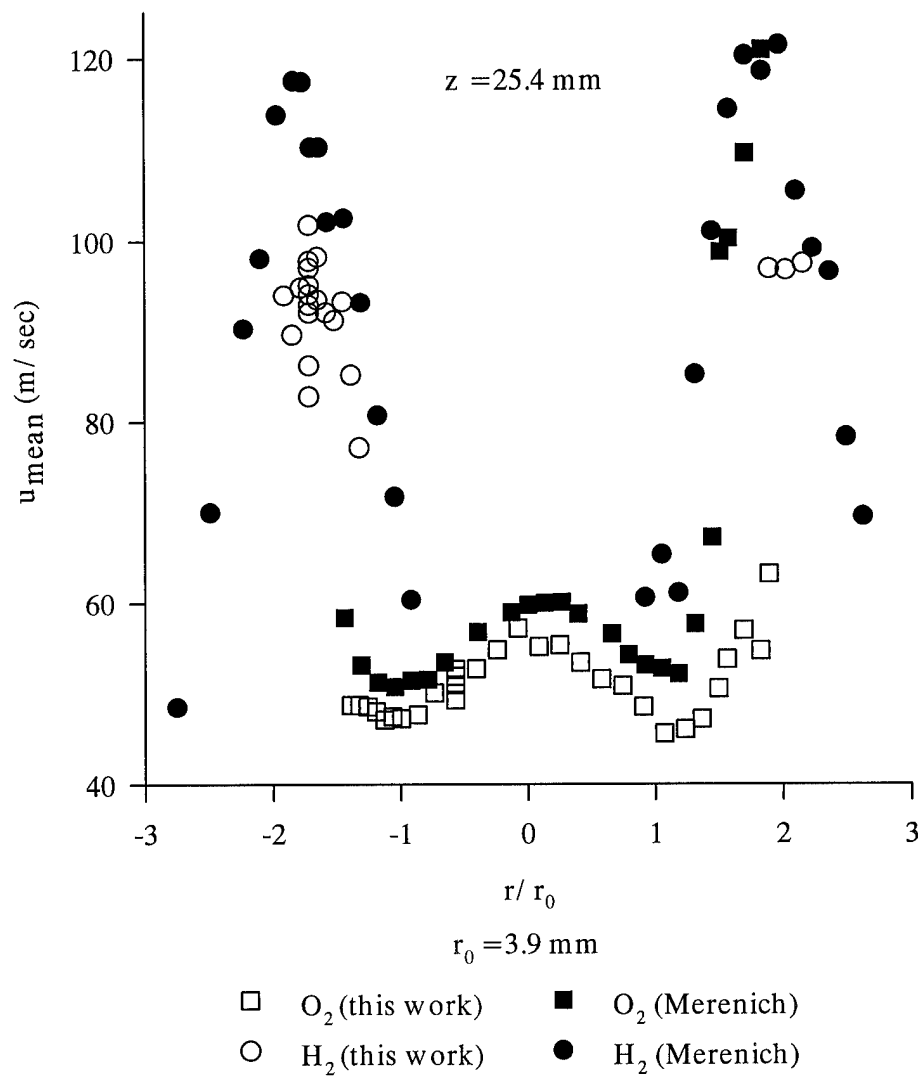
Fig. 6: Hot-Fire Measurements of Mean Velocity at 25.4 mm (1 in.) Axial Location

Hydrogen-seeded measurements were taken at radial positions of approximately 1.6 to 2.0 in both the upward and downward directions. Testing was temporarily discontinued outside this region when it was observed that the measured velocities were notably lower than those reported by Merenich.

The chamber was traversed in different spatial increments in this work as compared to Merenich's, so exact comparison of velocities was only possible at certain points. In general, however, the mean velocities were roughly 5 to 25 percent lower than Merenich's velocities. The differences were lesser in the core flow and greater in the hydrogen flow shear region. Likewise, the RMS velocities from this effort were generally higher than Merenich's and consequently, higher turbulence levels were noted in this effort.

Initial speculation as to the cause of the discrepancies between these data and Merenich's centered upon possible seed agglomeration. High speed flows require seed particles on the order of 1 μm or smaller to minimize particle lagging and accurately track the flow field [20, 22]. It was theorized that the seed particles in the recent firings may have agglomerated to larger than 1 μm and not properly tracked the flow.

The recent tests used the same batch of Al_2O_3 particles used by Merenich, Micro Abrasives Corporation's GB-2000 MicroGrit of nominal diameter 0.3 μm. However, the batch was approximately one year old and even though the particles were baked in an electric oven at 422 K (300 °F) for two weeks to remove moisture, it was conceivable that the seed might have "clumped" together during the year.

Therefore, a new batch of GB-2000 of nominal diameter 0.3 μm was obtained and the hydrogen-seeded firings repeated. The mean velocities in the nondimensional region 1.6 to 2.0 were slightly higher with the new seed than for the old batch, but were still 10 to 20 percent lower than Merenich's data.

The new batch of GB-2000 seed was then sifted through a 53 μm screen in an attempt to break up large clumps. Even though 53 μm was much larger than the nominal seed diameter, it was felt that forcing the seed through the sifter would decrease gross agglomerations. Firings with the sifted seed particles produced slightly higher velocities than the old seed batch but were still 10 to 20 percent lower than Merenich's velocities.

After discussing the problem with representatives from Micro Abrasives Corp., a seed sample specially formulated to enhance dispersion was obtained [30]. The sample consisted of flame phased alumina of nominal diameter 0.02 μm containing 99.6 percent Al_2O_3, 0.1 percent SiO_2, 0.2 percent Fe_2O_3, and 0.1 percent TiO_2. The additives were expected to act as flow agents and decrease agglomeration.

Firings with the specially formulated seed did not produce velocities significantly different from the original or sifted 0.3 μm Al_2O_3 The velocities were still notably less than reported by Merenich. In addition, the special seed sample had the undesirable characteristic of coating the viewing windows with a film which had to be frequently cleaned. Therefore, testing with this sample was terminated.

Finally, firings were made with the hydrogen flow seeded by unbaked particles from the new batch of GB-2000 (0.3 μm) Al_2O_3 All previous firings used oven-dried

seed and using unbaked seed was an attempt to isolate the influence of the baking process on the velocity measurements.

The unbaked seed produced the lowest velocities of all samples tested. Thus, adsorption of water from the atmosphere could affect seed distribution and measured velocities. Baking the seed to remove moisture was indeed warranted.

Figures 7, 8 and 9 summarize the results of the hydrogen-seeded firings with the various seed samples at the 25.4 mm (1 in.) axial location. As can be seen, none of the firings reproduced the mean velocity magnitudes observed by Merenich at this location. Furthermore, the RMS velocities and turbulence levels measured in these firings significantly exceeded the values reported by Merenich.

In a further attempt to explain the discrepancies from Merenich's data, hot-fire testing was suspended and cold-flow simulations begun.

Cold-Flow Simulations

The purpose of the cold-flow simulations was to examine the effect of different particle size distributions on the measured flow velocities to determine if agglomeration was responsible for the discrepancies from Merenich's data in the hot-firings.

Seed agglomeration may have raised the 0.3 μm nominal diameter beyond the 1 μm limit for accurately tracking the flow field. Agglomeration is an inherent problem when seeding flows with aerosol generators [31,32]. Potentially, agglomeration could be most severe for smaller original particle sizes. Thus, agglomeration could be reduced by
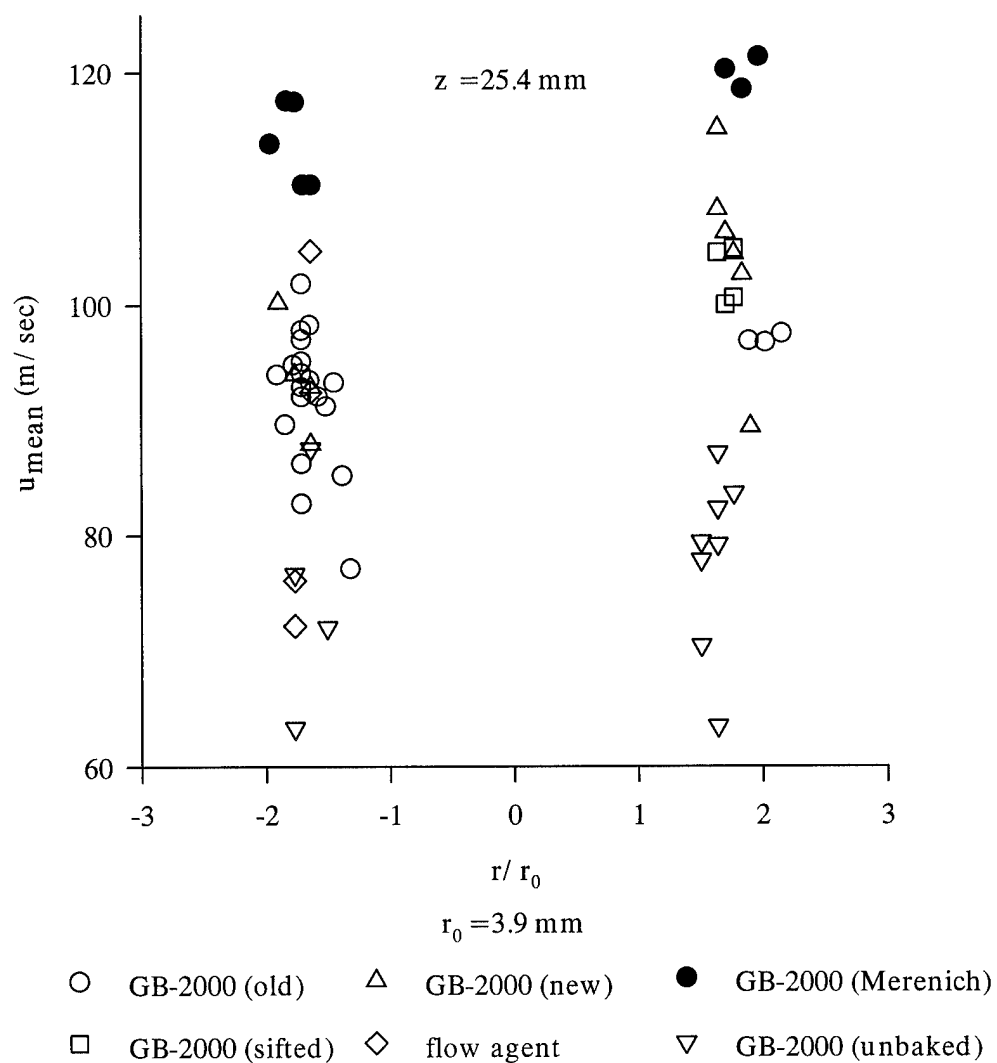
Fig. 7: Hot-Fire Measurements of Mean Velocity at the 25.4 mm (1 in.) Axial Location for Various Seed Samples
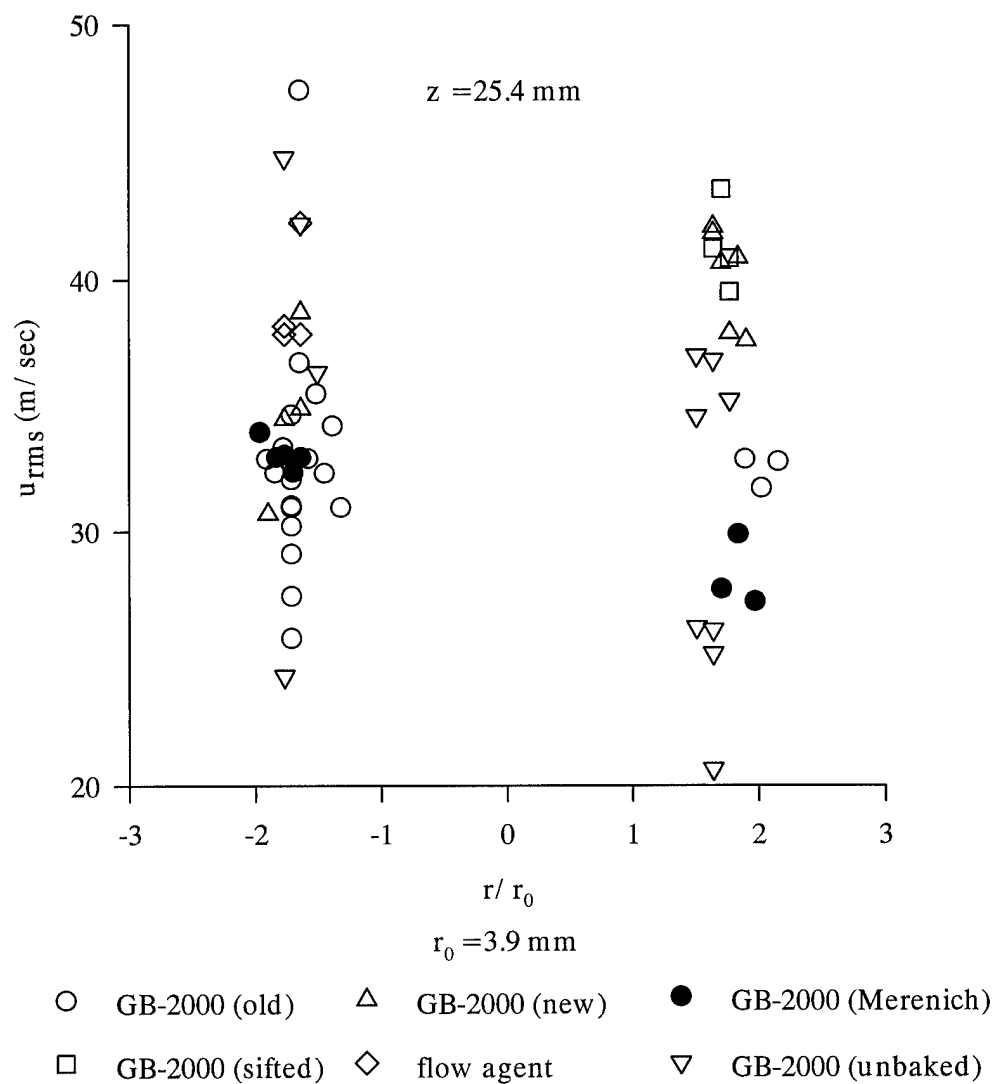
Fig. 8: Hot-Fire Measurements of RMS Velocity at 25.4 mm (1 in.) Axial Location for Various Seed Samples
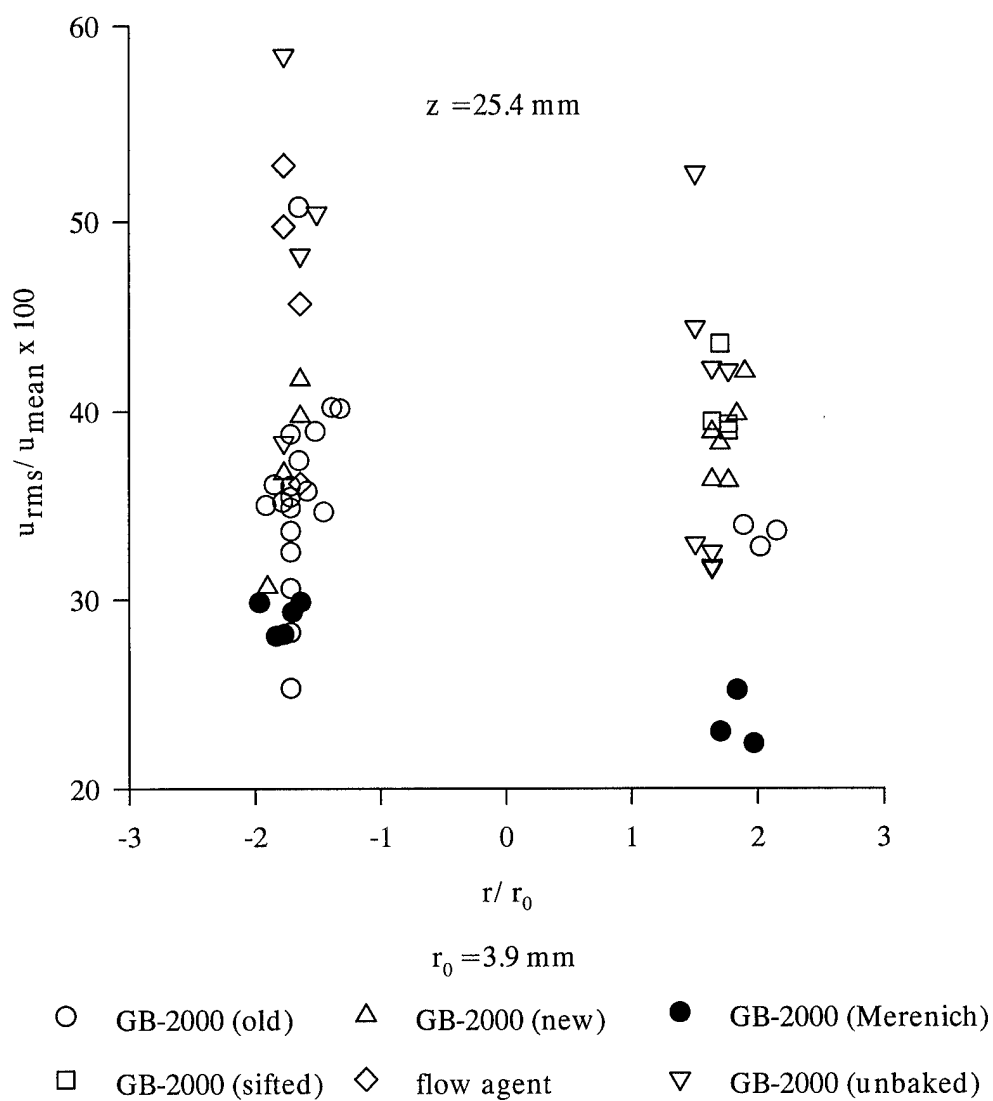
Fig. 9: Turbulence Level at 25.4 mm (1 in.) Axial Location for Various Seed Samples

using a slightly larger original nominal size [31]. For example, if 0.3 μm particles agglomerated to 1.2 μm and 0.4 μm particles only agglomerated to 0.8 μm, the flow would be more accurately tracked by the 0.8 μm particles despite the larger original diameter. Cold-flow simulations tested this hypothesis.

The cold-flow apparatus was almost identical to the actual hot-fire seeding system. Compressed air flowed through the fluidized bed seeder to entrain Al_2O_3 particles. Atmospheric pressure air simulated the hot-fire GH_2 flow since the density approximated the hydrogen injection density for the hot-firings. The seeder was the same unit which seeded the hydrogen flow in the rocket combustion tests. The flow through the seeder was controlled with a bypass valve which permitted a crude degree of control of the flow seeding. A critical orifice ensured constant mass flow. The seeded air jetted into the atmosphere through a 25.4 mm (1 in.) long exit tube. The injection velocity of the air was 140 m/sec, comparable to the hydrogen injection velocity in the hot-firings. Two different tubes were used: 1.4 mm (.056 in.) outer diameter and 3.8 mm (0.15 in.) inner diameter. The smaller tube approximated the width of the rocket injector fuel annulus whereas the larger tube approximated the exit area. The LDV probe volume was traversed across the tube exit and velocity measurements were taken at axial positions of 25.4 mm (1 in.) and 1.6 mm (0.063 in.) for the 1.4 mm and 3.8 mm tubes respectively.

The flow was seeded individually with six different sizes of aluminum oxide particles. The original GB-2000 seed (0.3 μm) was used as were two new samples of aluminum oxide from Sumitomo Chemical America, Inc.: AKP-3000 (nominal diameter

0.4 μm to 0.7 μm) and AKP-15 (nominal diameter 0.6 μm to 0.8 μm) [33]. In addition,

three samples were obtained from the Pennsylvania State University Materials Research

Center: A-16SG, A-1520, and T-61 [34]. These samples were produced by ALCOA.

A-16SG and A-1520 had nominal diameters of 0.48 μm and 1.6 μm respectively.

ALCOA was unable to provide size data on sample T-61 since it was a long-discontinued

product [35]. However, the particles in this sample appeared granular rather than

powdery and obviously were much larger than the other samples. The sample was not

expected to track the flow well but was included for comparison purposes.

Scanning electron microscope photographs of the various seed samples revealed

the particles did clump. In most cases, the clumps were significantly larger in size than

the reported nominal diameter of the sample. Furthermore, the particles were more

oblong than spherical which may have contributed to agglomeration. Thus, differences

were expected in the cold flow simulations.

Figures 10, 11 and 12 display the LDV results for the 25.4 mm (1 in.) axial

location downstream of the 1.4 mm (0.056 in.) diameter tube. The radial positions were

nondimensionalized by the outer tube radius (0.7 mm/0.028 in.).

Differences are apparent in the measured velocities for the various seed samples.

The differences are greatest along the flow centerline where the mean velocity is highest.

This is consistent with the idea that particle lagging of the flow will be greatest in the

region of highest velocity [20].

z =25.4 mm

u_{mean} (m/ sec)

r/ r_0

r_0 =0.7 mm

O	GB-2000 (0.3 μm)	□	MRC 0.48 μm	▽	AKP-3000 (0.5 -0.7 μm)
◇	AKP-15 (0.6 -0.8 μm)	O	MRC 1.6 μm	△	MRC T-61
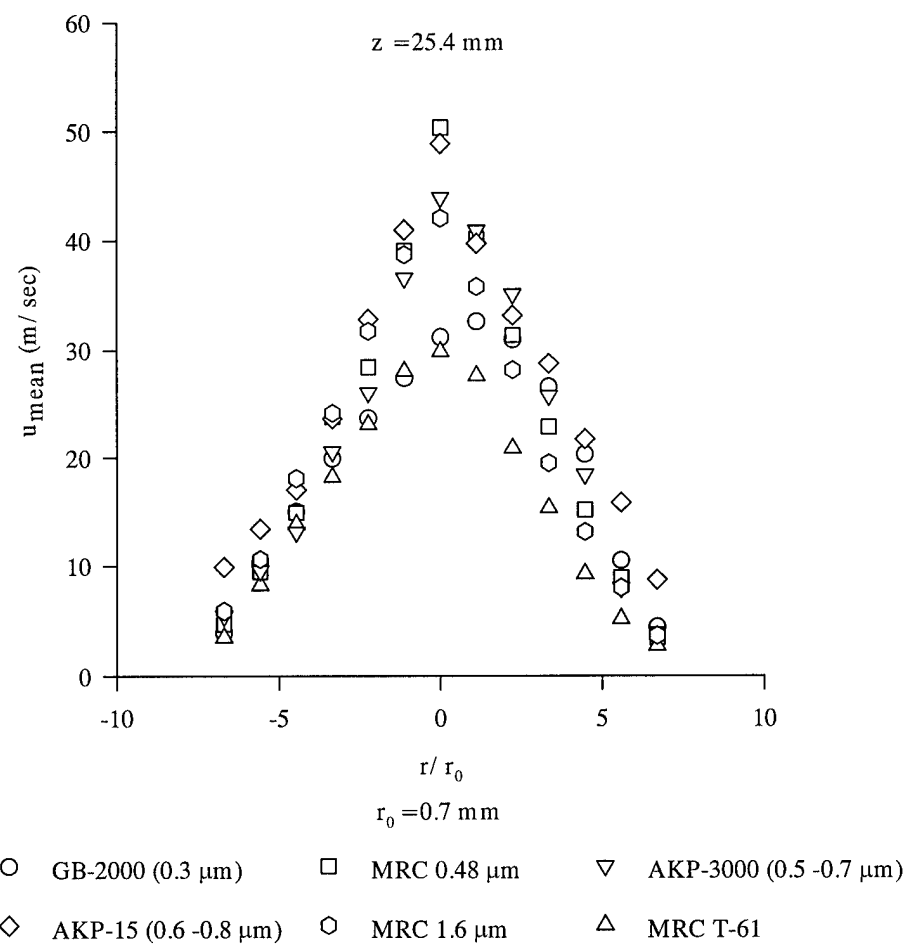
Fig. 10: Cold Flow Measurements of Mean Velocity for 1.4 mm (0.055 in.) Tube at 25.4 mm (1 in.) Axial Location
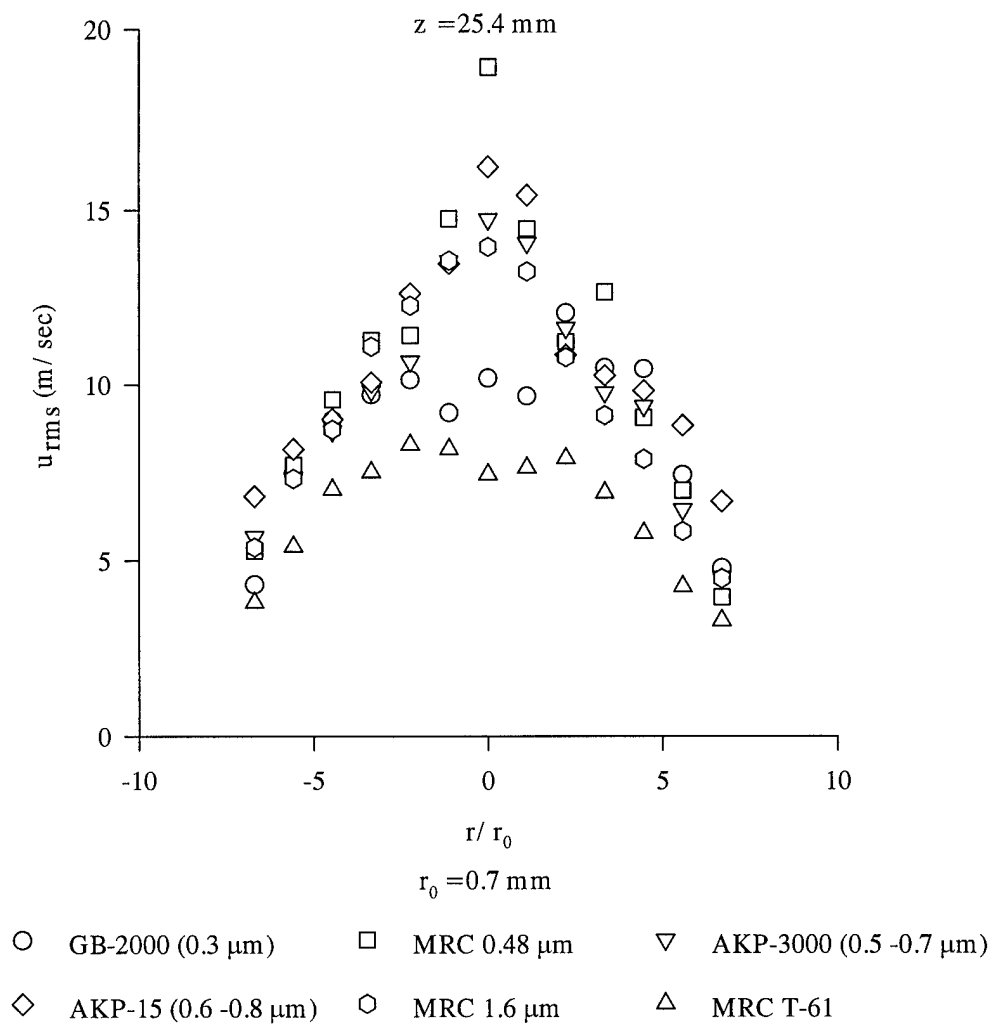
Fig. 11: Cold Flow Measurements of RMS Velocity for 1.4 mm (0.055 in.) Tube at 25.4 mm (1 in.) Axial Location
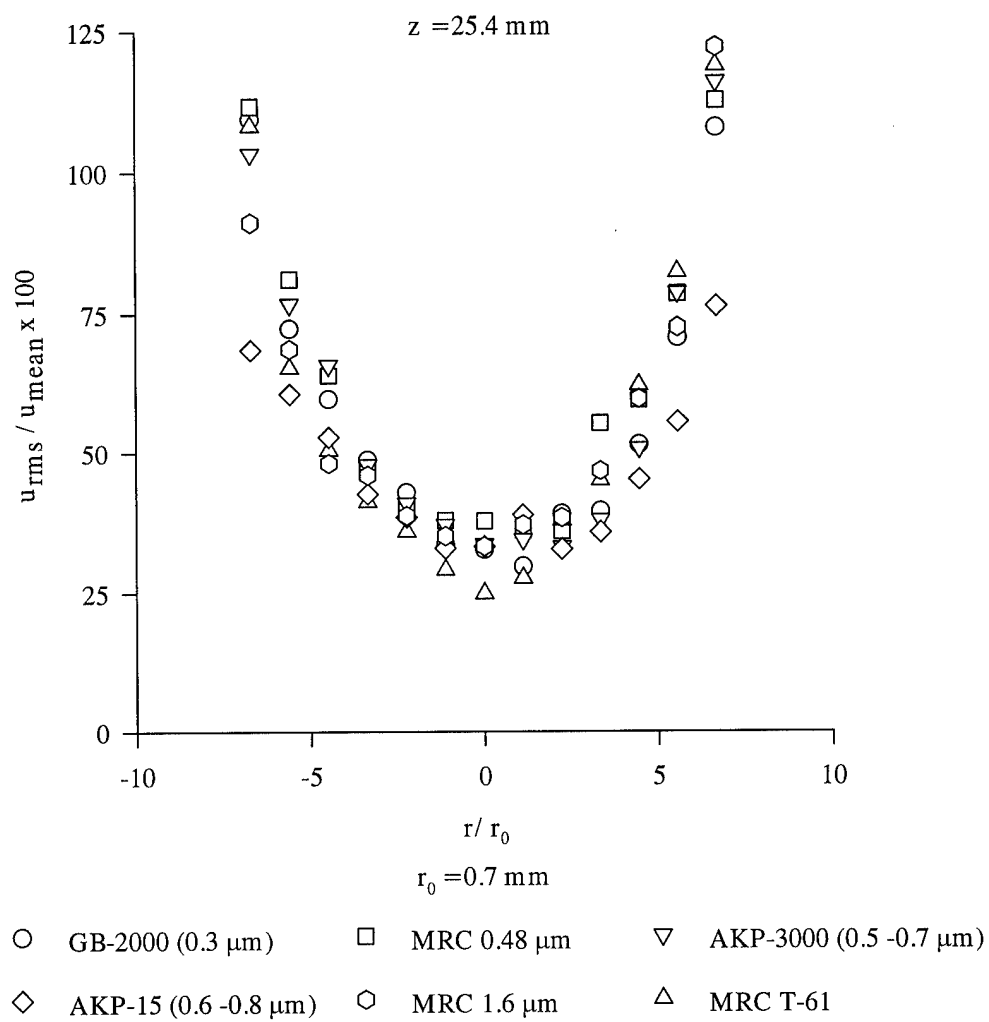
Fig. 12: Cold Flow Turbulence Level for 1.4 mm (0.055 in.) Tube at 25.4 mm (1 in.) Axial Location

The differences in the measured velocities were consistent with the hypothesis that particle agglomeration affected the velocity measurements. The A-16SG (0.48 μm), the AKP-15 (0.6 - 0.8 μm), and the AKP-3000 (0.4 -0.7 μm) samples produced the highest mean velocities. Apparently, agglomeration of these samples was less than the agglomeration of the nominally smaller GB-2000. The GB-2000 (0.3 μm) sample led to lower measured velocities suggesting that the particles were indeed agglomerating since an actual size of 0.3 μm should have accurately tracked the flow. The A-1520 (1.6 μm) sample revealed a higher mean velocity than the 0.3 μm sample, suggesting that the 0.3 μm particles were agglomerating to larger than 1.6 μm. The T-61 sample of unknown but large size clearly resulted in the lowest velocity as expected due to the greater particle lag induced by its larger size.

The LDV results for the 3.8 mm (0.15 in.) inner diameter tube are displayed in Figs. 13, 14 and 15 . Mean velocity differences between the seed samples were evident for this case also. The velocity profile is flatter as expected but the lowest velocity was recorded with the A-1520 (1.6 μm) sample rather than the T-61 sample as before. The highest mean velocities were registered by the AKP-15 (0.6 -0.8 μm) and the A-16SG (0.48 μm) as for the smaller exit tube case. The lowest RMS velocities and turbulence levels were recorded by the GB-2000 (0.03 μm) though the values were close to those registered by the AKP-15 (0.6 -0.8 μm) and A-16SG (0.48 μm).

z = 1.6 mm

u_{mean} (m/ sec)

r/ r_0

r_0 = 1.9 mm

○   GB-2000 (0.3 μm)   □   MRC 0.48 μm   ▽   AKP-3000 (0.5 -0.7 μm)

◇   AKP-15 (0.6 -0.8 μm)   ⬡   MRC 1.6 μm   △   MRC T-61
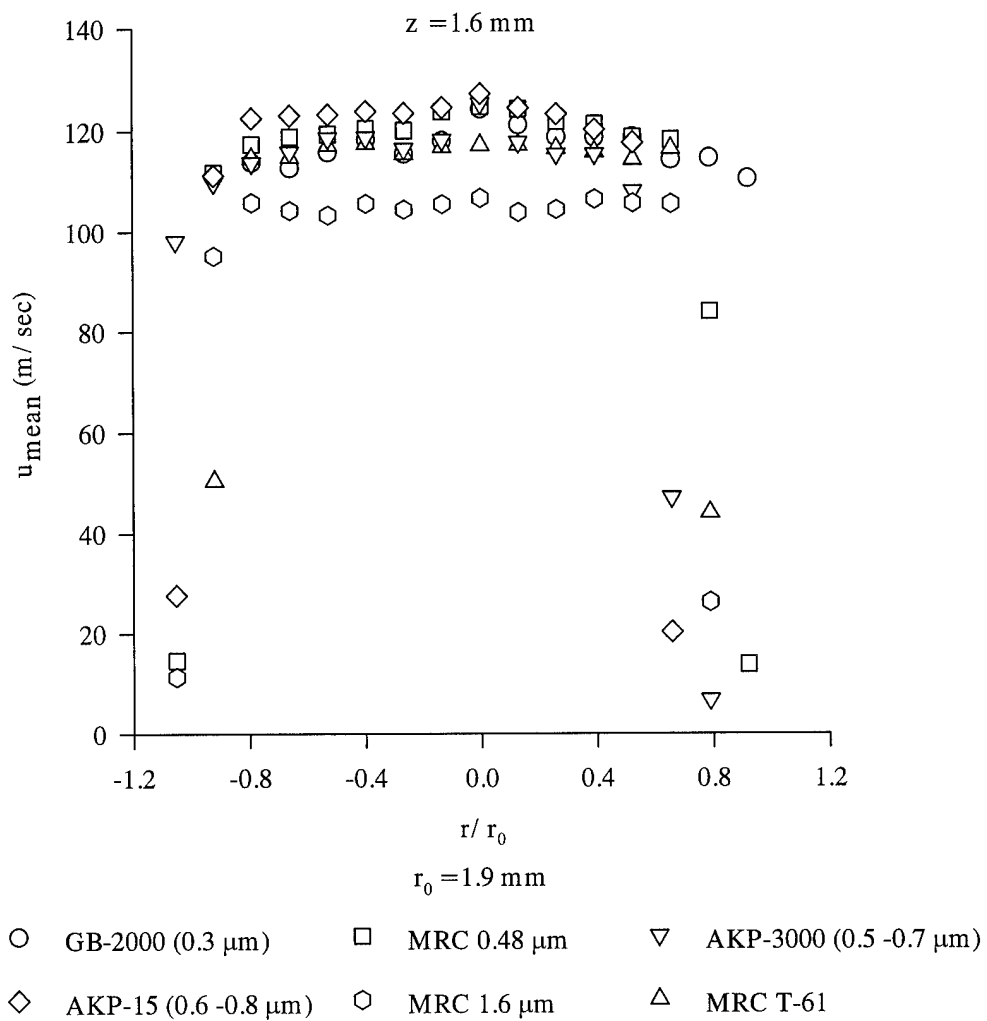
**Fig. 13:** Cold Flow Measurements of Mean Velocity for 6.4 mm Tube at 1.6 mm Axial Location
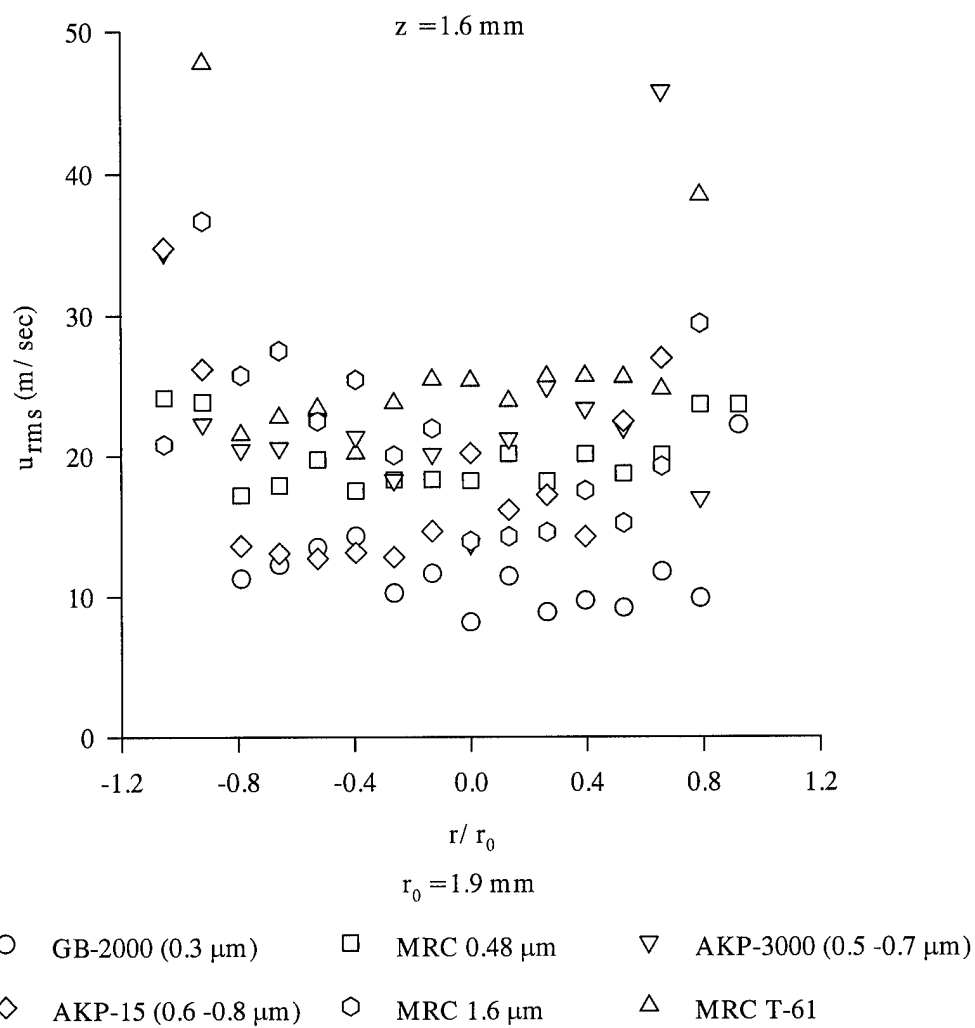
Fig. 14: Cold Flow Measurements of RMS Velocity for 6.4 mm Tube at 1.6 mm Axial Location
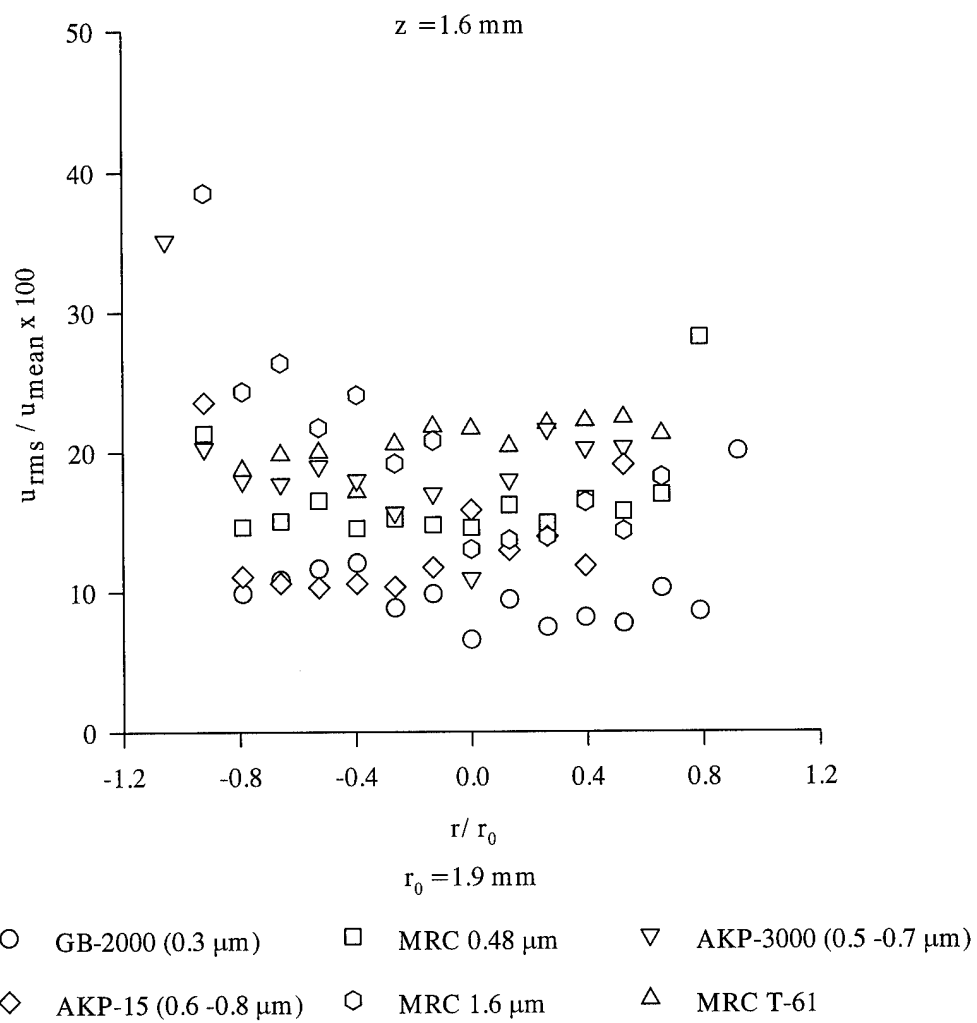
Fig. 15: Cold Flow Turbulence Level for 6.4 mm Tube at 1.6 mm Axial Location

More 25.4 mm (1 in.) Axial Location Hot Firings

Based on the cold flow simulations, the decision was made to repeat a limited set of hot firings at the 25.4 mm (1 in.) axial location. The AKP-15 (0.6 -0.8 μm) and the AKP-3000 (0.5 - 0.7 μm) were used to seed the hydrogen flow since they promised to produce the highest velocities. The firings were conducted with the seeder outlet valve closed. Seed for the LDV was provided by residual particles in the flow plumbing. This change resulted in slightly higher validation rates than the previous firings in this series.

Figure 16 displays the mean velocity results from these firings. No improvement was noted over the firings with the GB-2000 (0.3 μm). The mean velocities were still approximately 10 to 20 percent lower than Merenich's at that axial location. RMS velocities were generally 10 - 15 percent greater than Merenich's. The corresponding turbulence levels exceeded the Merenich data by approximately 20 percent (Figs. 17 and 18).

While the velocities discussed so far were up to 20 percent lower than reported by Merenich, they were self-consistent. In other words, roughly the same velocities were measured regardless of the sample that seeded the flow. The measurements appeared highly repeatable whereas Merenich's data could not be reproduced in these tests.

Since the seed-related differences in velocity which were evident in the cold flow simulations did not appear in the hot firings, it was decided to conduct all subsequent tests with the GB-2000 (0.3 μm) to be consistent with Merenich's tests.
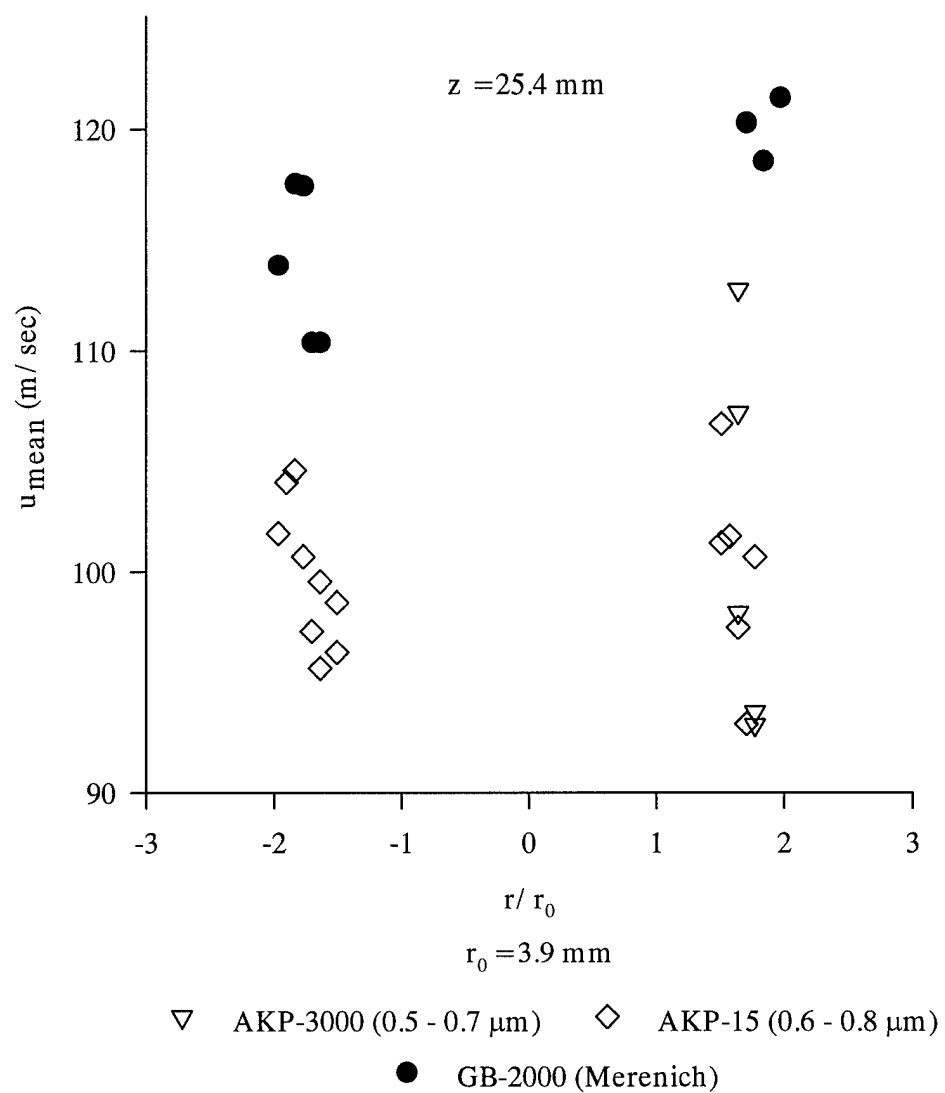
Fig. 16: Hot-Fire Measurements of Mean Velocity at 25.4 mm (1 in.) Axial Location
Using AKP-15 (0.6 - 0.8 μm) and AKP-3000 (0.5 - 0.7 μm)
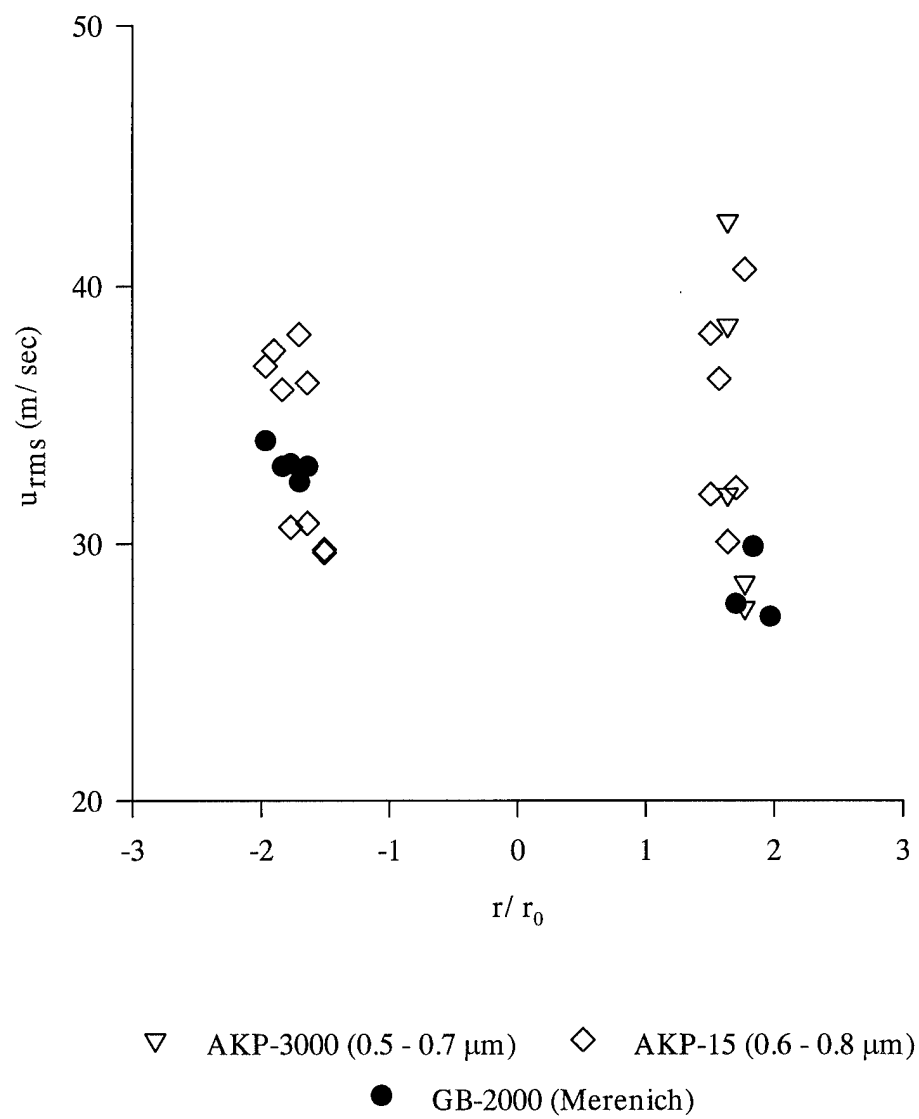
Fig. 17: Hot-Fire Measurements of RMS Velocity at 25.4 mm (1 in.) Axial Location Using AKP-15 (0.6 - 0.8 μm) and AKP-3000 (0.5 - 0.7 μm)
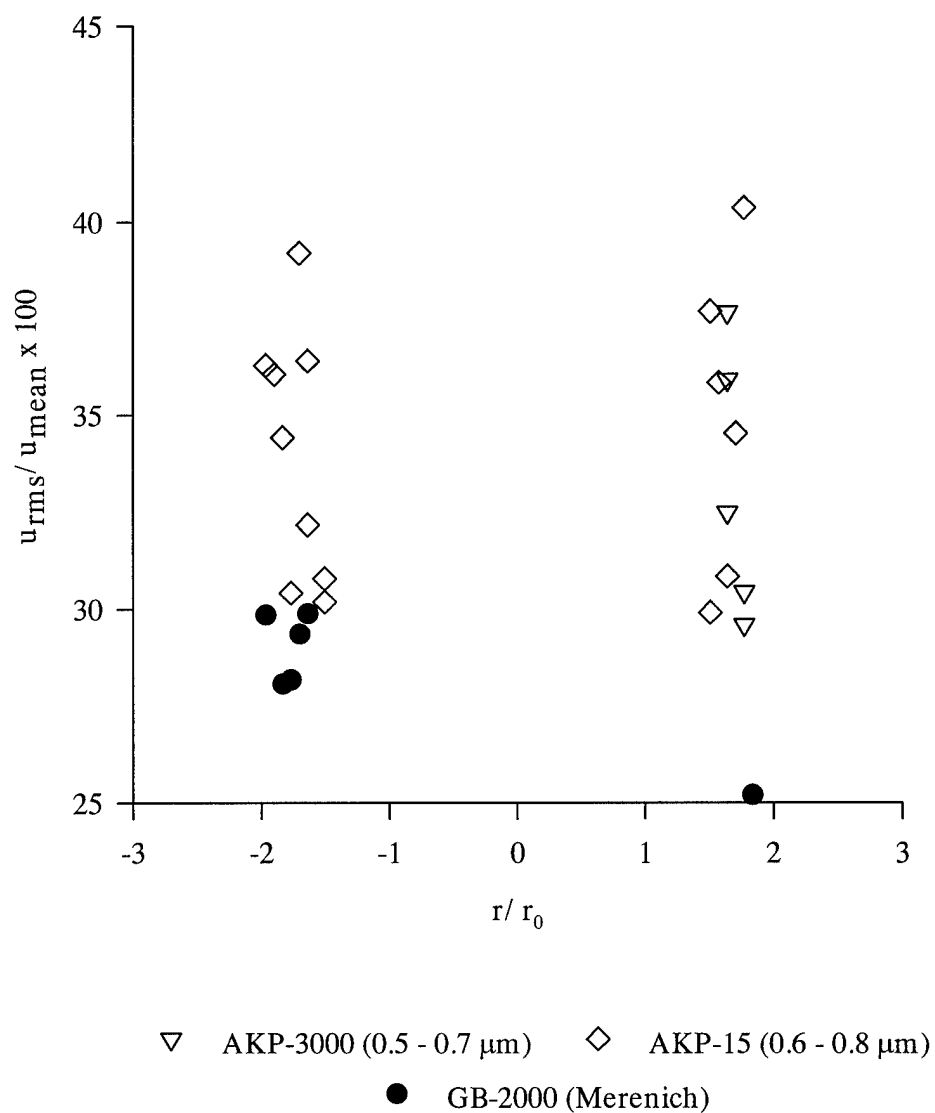
Fig. 18: Turbulence Level at 25.4 mm (1 in.) Axial Location Using AKP-15 (0.6 - 0.8 μm) and AKP-3000 (0.5 - 0.7 μm)

50.8 mm (2 in.) Axial Location Hot Firings

Measurements were made at the 50.8 mm (2 in.) axial location for additional comparison to Merenich's work. The mean velocities and those reported by Merenich are displayed in Fig. 19. As before, the radial position was nondimensionalized by the inner radius of the injector oxidizer post (3.87 mm/0.153 in.). The mean velocity at the flow centerline was 59.0 m/sec (193.6 ft/sec) and the flow was relatively uniform and symmetric in the central portion.

Seeding the oxygen flow permitted velocity measurements out to a non-dimensional radial distance of 2.46 in the downward (negative) direction and 2.30 in the upward (positive) direction.

Hydrogen flow seeding allowed measurements to be taken from the centerline to $r/r_0 = 2.75$ in the upward direction and to 5.57 in the downward direction. The measurements were limited in the upward direction by the PDPA setup geometry. Due to the transmitter angle, when the probe volume was raised beyond $r/r_0 = 2.75$, the laser beams laid above the upper edge of the viewing window and could not enter the chamber. However, the PDPA angle did allow measurements in the downward direction to a non-dimensional radius of 6.25, contingent upon the presence of sufficient seed particles.

Asymmetries appeared for the hydrogen seeded flow. The peak velocity was 73.2 m/sec (240.2 ft/sec) at a nondimensional position of 2.36 upward. However, the maximum velocity below the centerline was only 62.5 m/sec (205.1 ft/sec) at -1.97.
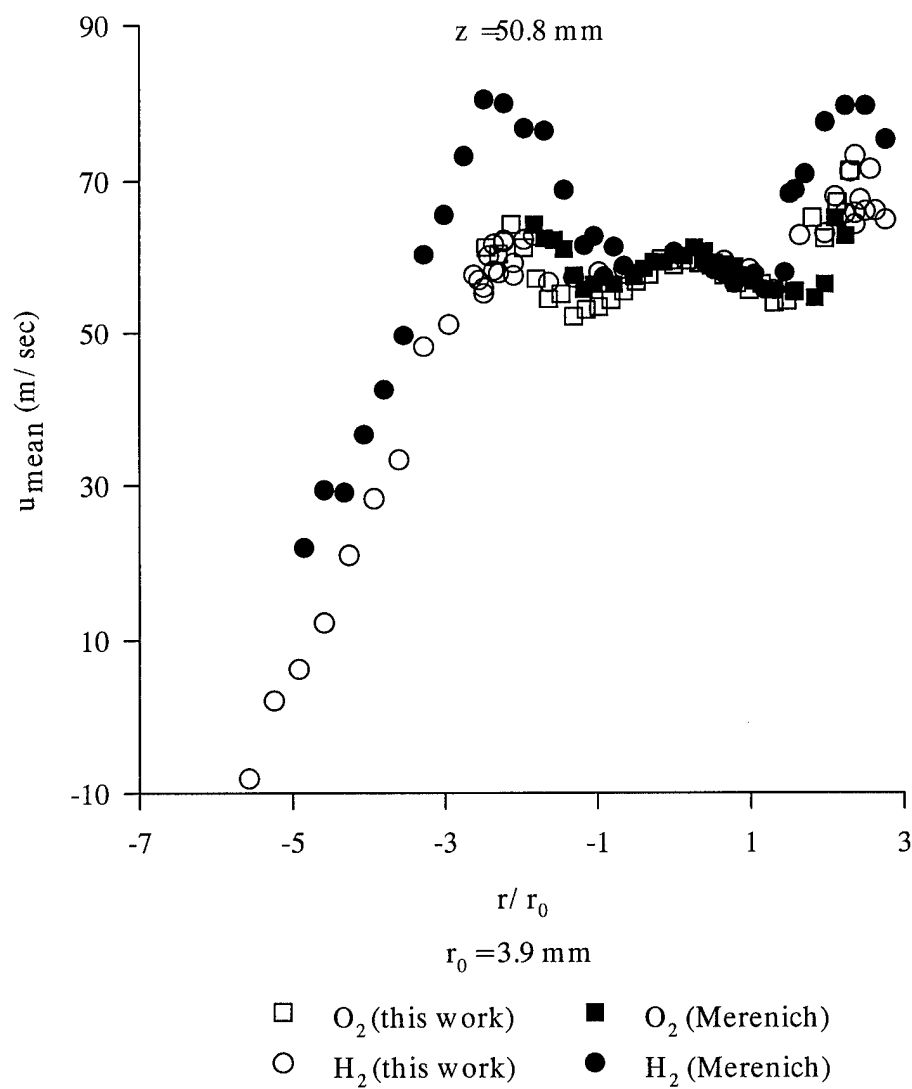
Fig. 19: Hot-Fire Measurements of Mean Velocity at 50.8 mm (2 in.) Axial Location

Differences were measured between the hydrogen-seeded and the oxygen-seeded velocities. In the central part of the flow, the hydrogen-seeded tests revealed velocities slightly higher than the corresponding oxygen-seeded tests. A flatter profile resulted since the velocities did not drop off as quickly for increasing radial distance. In general, the hydrogen-seeded measurements revealed higher velocities than the oxygen-seeded measurements at the same radial locations. The difference was greatest in the nondimensional region 1.31 to 1.97 from the centerline in both directions. The velocities from the hydrogen-seeded and oxygen-seeded flows converged in the nondimensional region 1.97 to 2.30 from the centerline. At the 2.30 nondimensional radial location and beyond, the oxygen-seeded flows revealed slightly higher velocities, e.g. 60.5 m/sec (198.5 ft/sec) for the oxygen-seeded versus 58.0 m/sec (190.3 ft/sec) for the hydrogen-seeded flow at the 2.30 downward location. Thus, the measured mean velocity at a particular radial location depended upon which flow was seeded which is probably a reflection of the unsteady movement or "flapping" of the flame front. Charge coupled device images taken by Merenich suggested that the central oxygen-rich region ejected large scale turbulent structures analogously to bursts in the near wall region of a turbulent boundary layer [9]. The data from this effort support that interpretation.

At a nondimensional distance of 5.57 downward, the measured mean velocity became negative indicating a recirculation zone near the chamber wall. The seed at this radial location was very sparse and no measurements were possible closer to the wall.

Figure 20 illustrates the measured RMS velocities at the 50.8 mm (2 in.) axial location. The RMS velocities in the central flow, as measured by oxygen seeding , were relatively uniform at approximately 6 m/sec (20 ft/sec). Seeding the hydrogen flow yielded higher RMS velocities in the central flow, approximately 6 to 17 m/sec (20 to 56 ft/sec). The RMS values for both seeded flows jumped dramatically beyond a non-dimensional distance of approximately 1.31 from the flow centerline. The oxygen-seeded flow produced a maximum RMS value of 24.3 m/sec (79.7 ft/sec) at 1.48 downward radial location while the hydrogen-seeded flow peaked at 25.7 m/sec (84.3 ft/sec) at 2.30 downward. The peak RMS locations resided in the region where mixing between the hydrogen and oxygen was expected to be greatest. As before, the magnitude of the velocity depended upon which flow was seeded. In general, the hydrogen-seeded flows yielded higher RMS values than the oxygen-seeded flows at the same locations.

Figure 21 plots the turbulence intensity for the 50.8 mm (2 in.) axial location. The turbulence level remained relatively constant throughout the flow core at approximately 10 percent for the oxygen-seeded flow. The hydrogen-seeded flow displayed a higher turbulence level in the central core, approximately 20 percent. The turbulence intensity for fully developed pipe flow is typically 5 percent [36]. Consequently, the core flow possessed a higher energy content in relation to pipe flow [9].
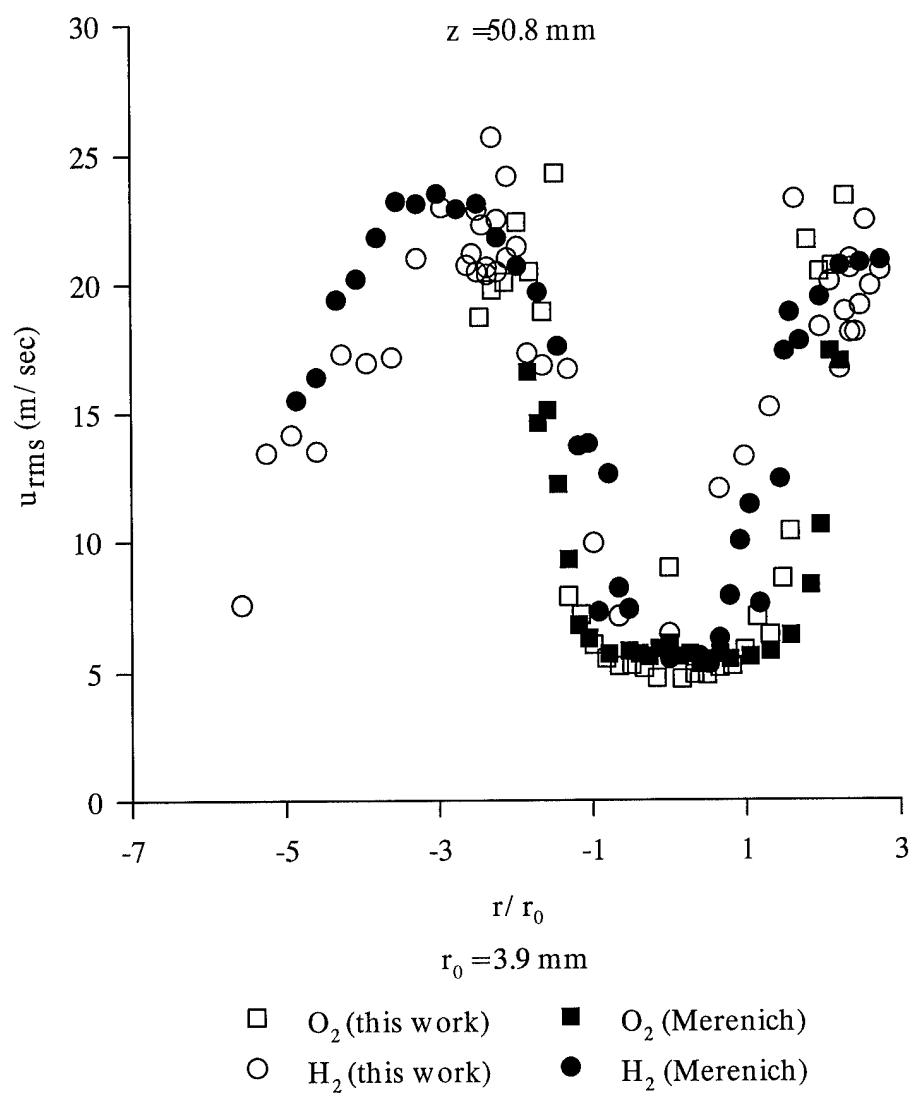
Fig. 20: Hot-Fire Measurements of RMS Velocity at 50.8 mm (2 in.) Axial Location
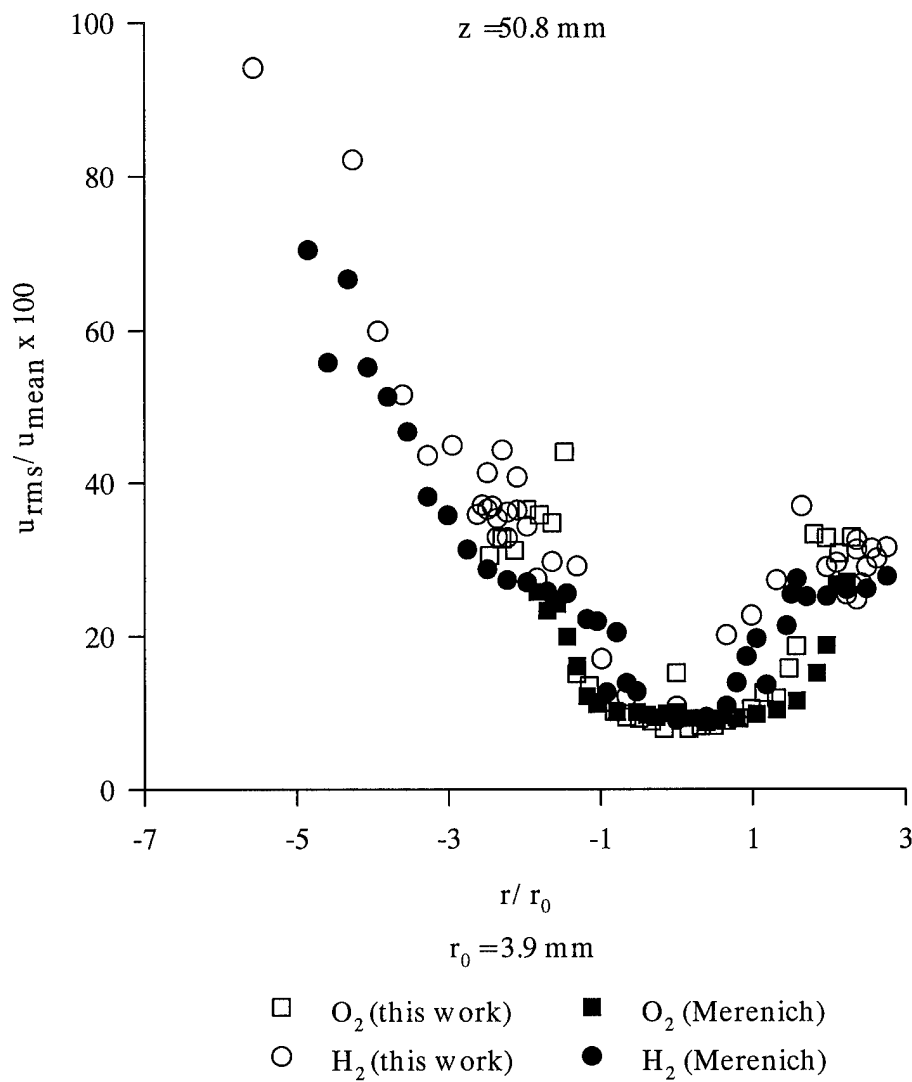
Fig. 21: Turbulence Level at 50.8 mm (2 in) Axial Location

Beyond a nondimensional distance of 1.3, both the oxygen-seeded and hydrogen-seeded flows revealed a jump in turbulence intensity to greater than 30 percent. Apparently, flow mixing was high in this region. Moving further from the centerline, the hydrogen-seeded flow turbulence intensity increased until it reached very high levels near the wall. The high calculated turbulence levels were probably a consequence of the relatively low mean velocities in the near-wall zone as compared to the RMS values and not an indication of the level of mixing.

When compared to the data from Merenich, the more recent profiles reveal the same general shape and behavior except that Merenich measured mean velocities roughly 15 to 20 percent higher than obtained in this work. The RMS velocities and turbulence levels measured by Merenich also display values which are from 2 to 20 percent higher than the current work.

The lower mean velocities and higher RMS velocity and turbulence levels seen at the 50.8 mm (2 in.) axial location as compared to Merenich's data are consistent with the results at the 25.4 mm (1 in.) location.

This effort repeatedly measured mean velocities which were lower than reported by Merenich. Since different-sized seed particles did not reduce the velocity differences, particle agglomeration does not appear to be the source of the discrepancies. Further discussion of possible causes for the discrepancies will be deferred until a later section.

12.7 mm (0.5 in.) Axial Location Hot Firings

The LDV probe volume was moved upstream and measurements performed at the 12.7 mm (0.5 in.) axial location. This location was further upstream than any location measured in the work of Merenich. The mean velocities as a function of radial location (nondimensionalized by the oxidizer post radius) are displayed in Fig. 22.

The peak mean velocity in the core flow, 59.6 m/s (195.6 ft/sec), was at the centerline. The value is slightly higher than the peak core velocity registered by the oxygen-seeded flow at the 25.4 mm (1 in.) axial location (57.2 m/sec /187.7 m/sec) and approximately equal to the peak core velocity at the 25.4 mm (1 in.) location reported by Merenich (59.9 m/sec /196.5 ft/sec).

The core velocity decreased to $\approx$ 45 m/sec (148 ft/sec) at nondimensional radii of 1.0 in both directions, i.e. at the edge of the oxidizer post. Beyond these distances, the velocity increased sharply due to the influence of the higher-velocity hydrogen flow.

The flow was asymmetric. The peak velocity in the hydrogen-seeded flow was 156.3 m/sec (512.8 ft/sec) at a nondimensional radius of 1.4 in the downward direction. At the corresponding radius in the upward direction the peak velocity was only 136.9 m/sec (539.0 ft/sec). The asymmetry could have been due to imprecise alignment of the probe volume to the chamber centerline. However, the asymmetry was also seen in the profiles at the 25.4 mm (1 in.) and the 50.8 mm (2 in.) locations in this effort and Merenich's data. Thus, it is likely to be a flow characteristic or a resolution by-product of step-size and sharp velocity peaks rather than an artifact of the alignment process.
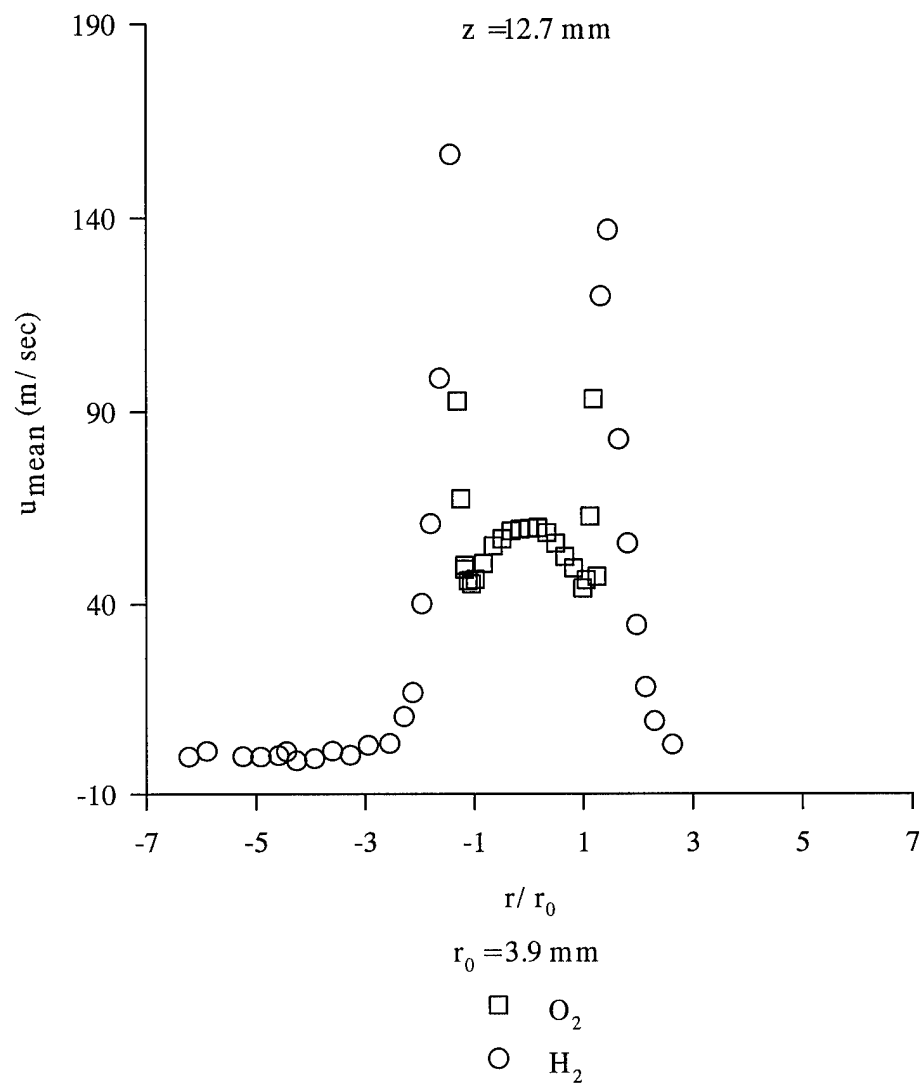
Fig. 22: Hot-Fire Measurements of Mean Velocity at 12.7 mm (0.5 in.) Axial Location

Velocity measurements were taken radially outward almost to the chamber wall in the downward direction. Sufficient seed was present to record velocities to a radial location of -6.2 which was closer to the wall than any previous measurement at any axial location in either this work or that of Merenich. Near the wall, the mean velocities were very small and were negative in the region -3.9 to -4.2, indicating a recirculation zone. Measurements in the upward direction were limited to a nondimensional radius of 2.6 due to the PDPA geometry.

With the hydrogen flow seeded, measurements were not obtained within the non-dimensional region -1.4 to 1.3. Since the seed particles can be considered to be passive scalars [37], the positions where the seeded GH_2 flow permitted measurements indicated the presence of hydrogen either as elemental H_2 or the combustion product H_2O. Therefore, at the 12.7 mm (0.5 in.) axial location, hydrogen did not penetrate into the GO_2 core flow. Contrast this case with the 50.8 mm (2 in.) axial location in which hydrogen-seeding permitted measurements all the way to the centerline. Obviously, the flows were more thoroughly mixed and/or the combustion process was more complete further downstream. This conclusion is supported by the fact there was no measurement overlap at the 12.7 mm (0.5 in.) location, i.e. there were no radii where measurements were possible with both the hydrogen flow and oxygen flow seeded.

The peak velocities in the hydrogen-seeded flow occurred radially outward from the shadow of the injector annulus and were lower than the calculated mean hydrogen injection velocity of 185 m/sec. Apparently, the GH_2 flow diffused, mixed with the GO_2

and/or combustion products, and slowed down, a conclusion supported by the peaking of the RMS values in the same region, suggesting that mixing occurred (Fig. 23).

The turbulence level in the central core was approximately 13 percent and was therefore greater than the turbulence level at the corresponding radii for the 50.8 mm (2 in.) axial location. The turbulence level in this region was roughly the same as for the 25.4 mm (1 in.) axial location, suggesting that between 25.4 mm (1 in.) and 50.8 mm (2 in.) turbulence diminished, perhaps by flow spreading and combustion.

Figure 24 illustrates the turbulence level. The scale has been limited to preserve detail. Beyond a nondimensional radius of 1.2 the turbulence level jumped dramatically to greater than 40 percent. In the hydrogen-seeded flow the turbulence had values on the order of hundreds or thousands of percent. The very high turbulence near the wall was due to the low mean velocities in the recirculation region.

6.4 mm (0.25 in.) Axial Location Hot Firings

Measurements were taken at the 6.4 mm (0.25 in.) axial location. Mean velocities are plotted in Fig. 25. The peak centerline mean velocity for the GO_2-seeded flow was 66.8 m/sec (219.2 ft/sec). The velocity quickly dropped to ≈ 40 m/sec (131 ft/sec) at the radius corresponding to the edge of the oxidizer post ($r/r_0 \approx 1$). Oxygen-seeded measurements were only obtained in the nondimensional region -1.2 to 1.2. This region was slightly narrower than at the 12.7 mm (0.5 in.) downstream location. Hence, the trend toward less mixed, more distinct flows upstream continued. The influence of
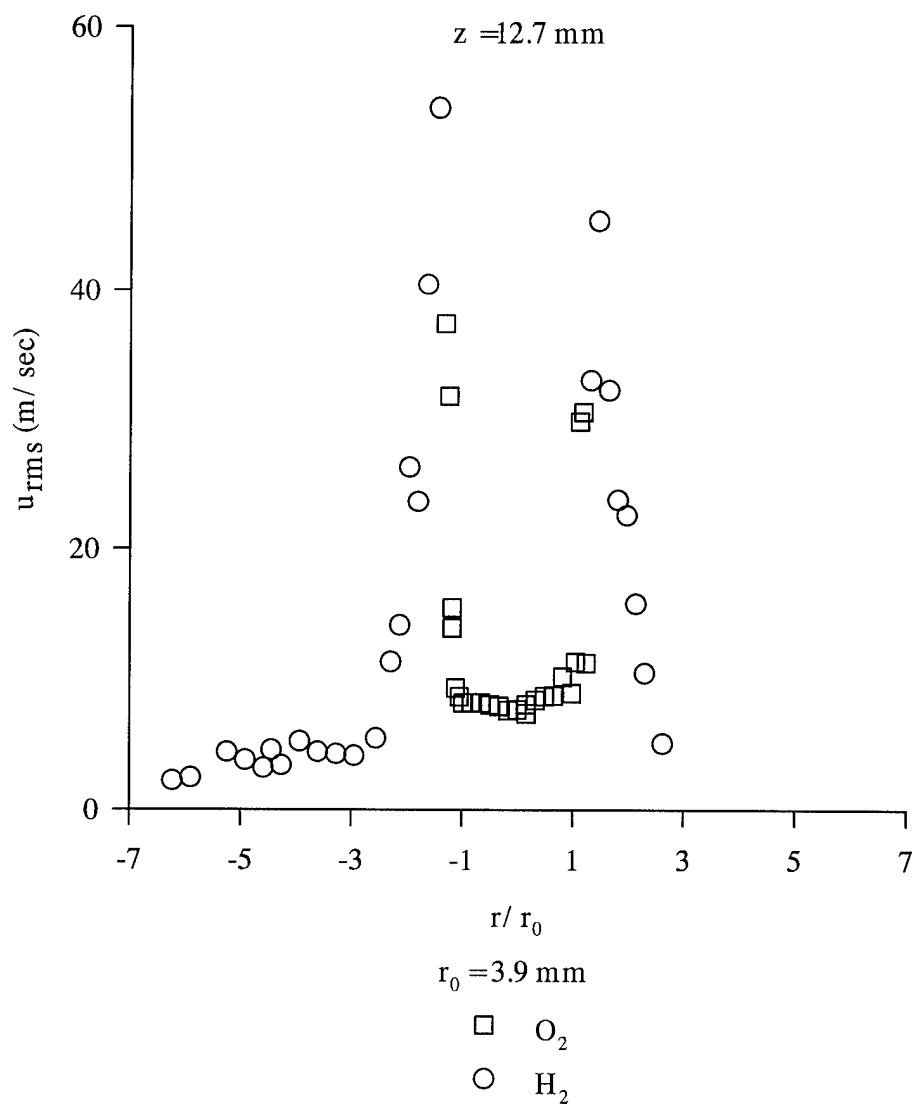
Fig. 23: Hot-Fire Measurements of RMS Velocity at 12.7 mm (0.5 in.) Axial Location
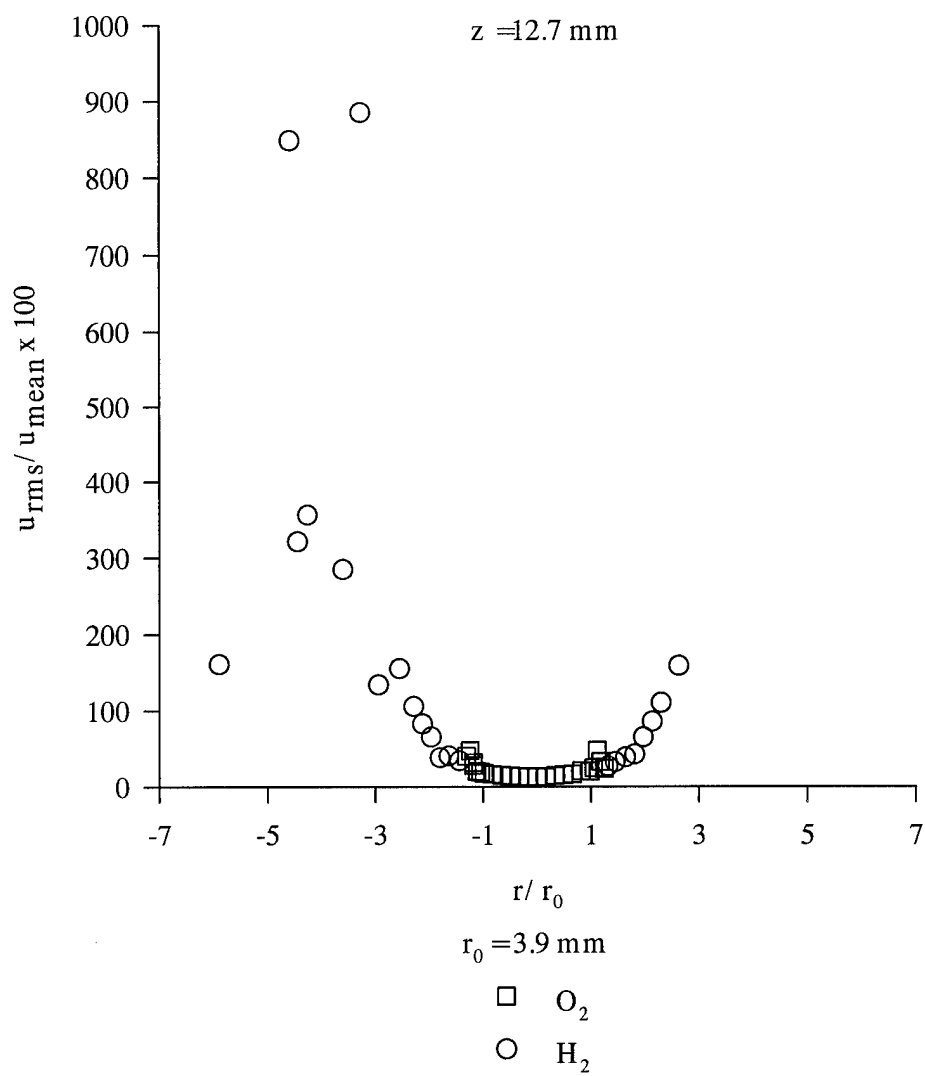
Fig. 24: Turbulence Level at 12.7 mm (0.5 in.) Axial Location
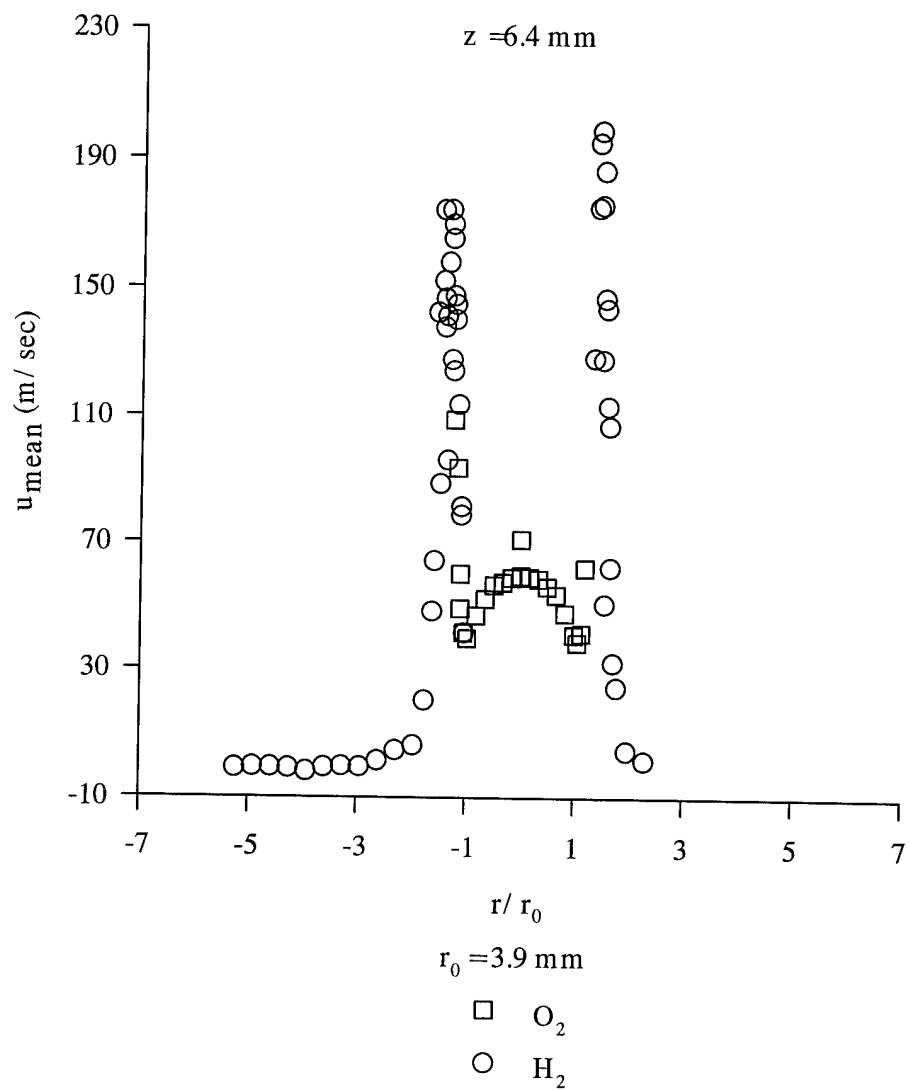
Fig. 25: Hot-Fire Measurements of Mean Velocity at the 6.4 mm (0.25 in.) Axial Location

the higher velocity hydrogen flow was evident beyond radii of 1.1 since the velocity quickly rose with increasing radial distance.

Measurements with seeded GH_2 revealed additional information. Measurements were obtained at nondimensional radii of 1.3 to 1.6 in the upward direction and 1.0 to 5.2 in the downward direction. An overlap region in which hydrogen-seeded and oxygen-seeded measurements were possible existed at radii -1.0 to -1.2. Consequently, oxygen, hydrogen, and their combustion products were likely to be present there. In general, seeding the GH_2 flow resulted in higher velocities than seeding the GO_2 flow in this overlap area. The seeding-dependency of the measured mean velocity which was seen at the 25.4 mm (1 in.) and 50.8 mm (2 in.) axial locations and was curiously absent at the 12.7 mm (0.5 in.) location was evident here.

The peak GH_2-seeded velocities were measured at radii corresponding to the shadow of the injector fuel annulus. However, within this region the particle percent validation rate decreased abruptly, perhaps because of excessive seed particle concentration in the narrow area.

The flow was asymmetric as in the downstream cases discussed previously. The peak GH_2-seeded flow velocities were located above the centerline as opposed to the previous profiles in which the peak GH_2-seeded velocities occurred below the centerline. The GO_2-seeded flow peak velocities were seen below the chamber centerline.

Measurements extended to a nondimensional radius of 5.2 downward. No data were collected outward of this point due to insufficient seed particles. The seed "ran out"

closer to the centerline than for the previous axial profiles. The mean velocity was

negative beyond the -2.9 radius, making the recirculation zone at this axial location larger

than for any of the downstream positions.

As seen in Fig. 26, the RMS velocity profile was relatively uniform within the

shadow of the oxidizer post, $\approx$15 m/sec (49 ft/sec). The associated turbulence level was

around 25 percent, making the central core at this axial location the most turbulent of the

profiles examined thus far (Fig. 27).

The RMS values peaked and the turbulence increased dramatically within the

shadow of the fuel annulus. Clearly, this was an area of high shear flow. In the peak

velocity region, the turbulence intensity was $\approx$ 28 percent, similar to that reported for

turbulent hydrogen/air diffusion flames [38, 39]. Outside the fuel annulus radius, the

RMS values decreased but not as swiftly as the mean velocity. Therefore, the turbulence

level continued to rise, especially within the recirculation zone. This behavior was

consistent with that seen at the downstream stations.

1.6 mm (0.063 in.) Axial Location Hot Firings

The final station studied was 1.6 mm (0.063 in.) downstream of the injector exit

plane. The mean velocities are plotted in Fig. 28. The oxygen-seeded profile was flat in

the central portion of the flow between nondimensional radii -0.25 and 0.25 at

approximately 62 m/sec (203 ft/sec). Outside this region the mean velocity rapidly

decreased to roughly 30 m/sec (98 ft/sec) at the edge of the oxidizer post ($r/r_0 \approx 1$).
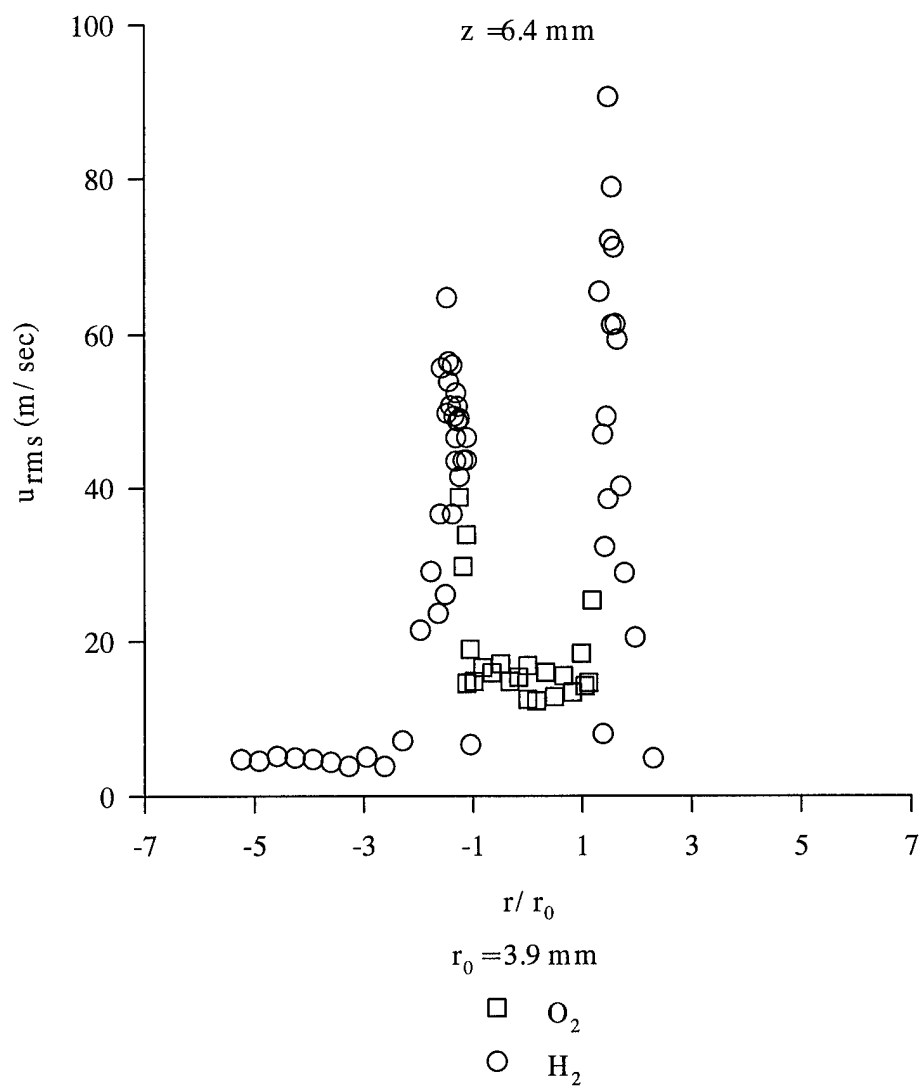
Fig. 26: Hot-Fire Measurements of RMS Velocity at 6.4 mm (0.25 in.) Axial Location
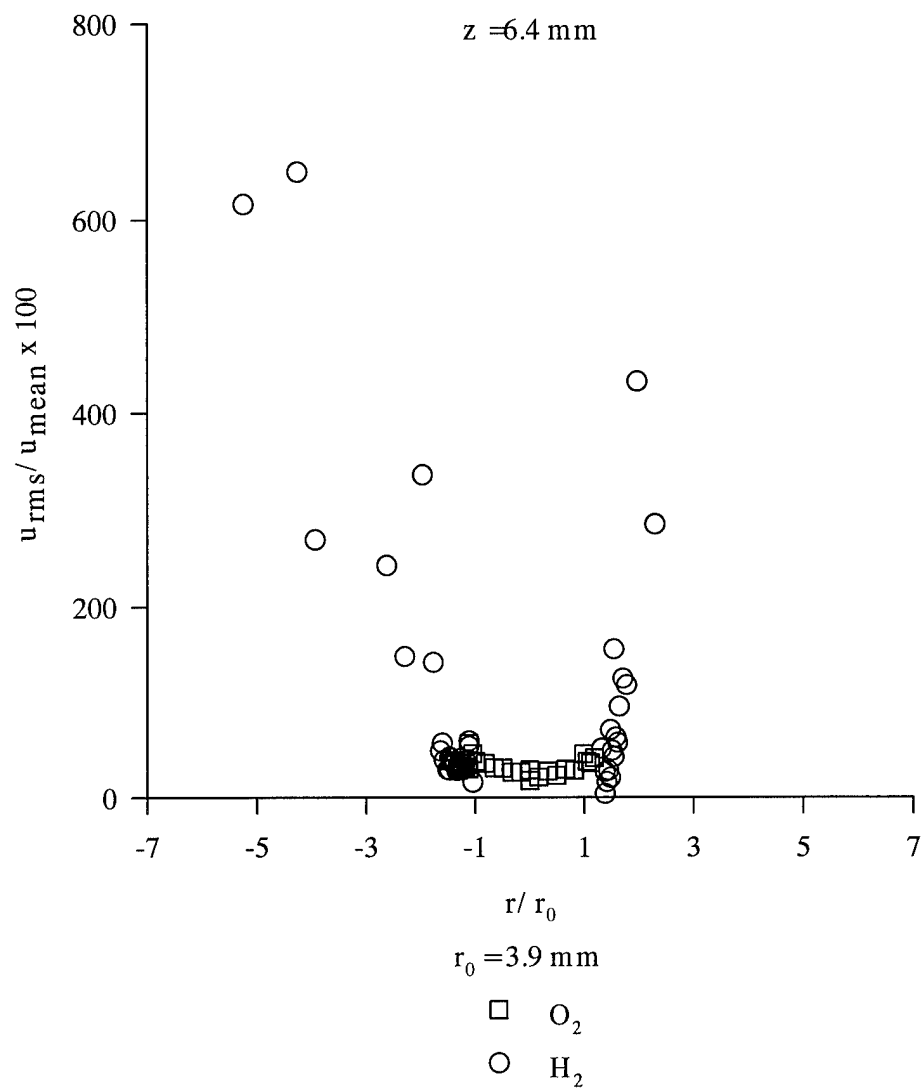
Fig. 27: Turbulence Level at 6.4 mm (0.25 in.) Axial Location
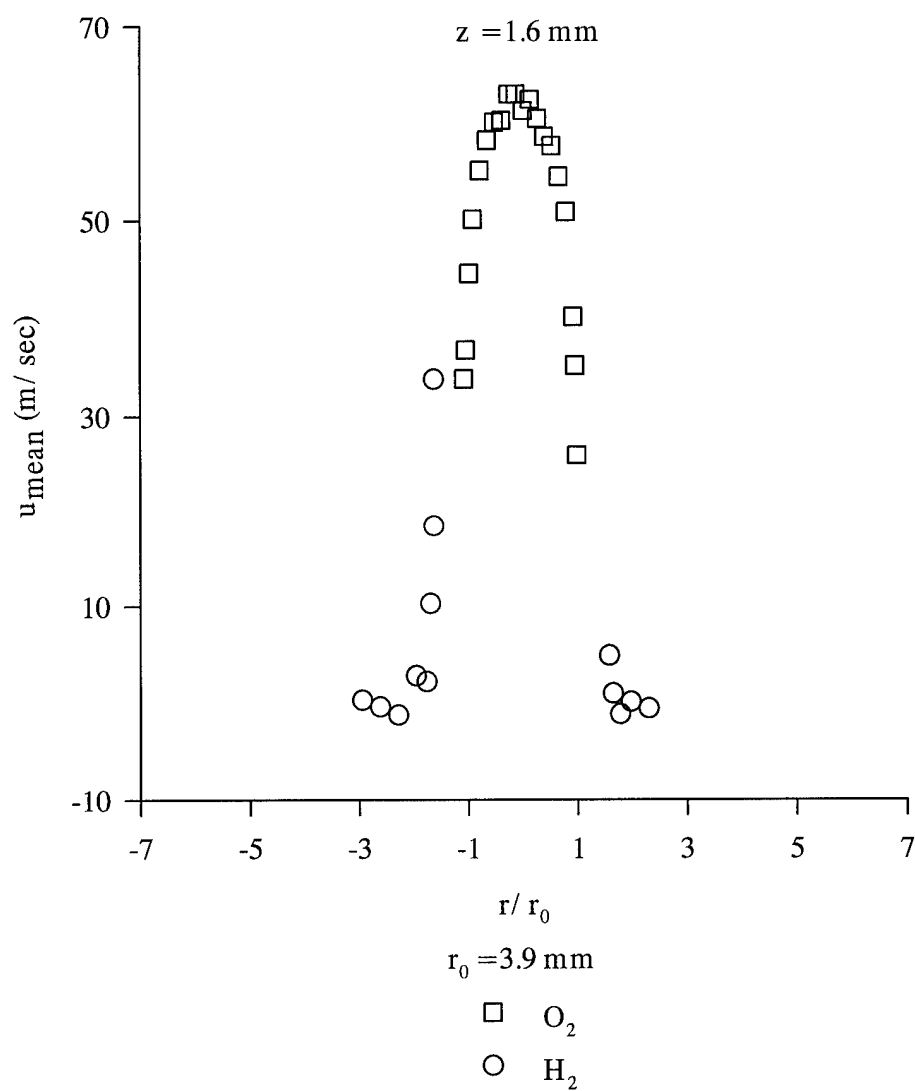
Fig. 28: Hot-Fire Measurements of Mean Velocity at 1.6 mm (0.063 in.) Axial Location

With the GH_2 flow seeded, measurements were only possible outside of the non-dimensional radii 1.6 both above and below the centerline, i.e. beyond the shadow of the injector posts. Outside of these radii, measurements were obtained but the amount of seed was sparse, resulting in sample sizes on the order of only 10^1 to 10^2. The "peak" GH_2-seeded velocities were much lower than for the downstream locations. Obviously, the true peaks were somewhere in the shadow of the fuel annulus but were unable to be measured. It is conceivable that the seed density in the constrained area of the shadow region was too great to permit LDV measurements.

Measurements were taken out to a maximum of $r/r_0 \approx 3$. A recirculation zone was noted beyond a non-dimensional radius of approximately 2 both above and below the centerline. The recirculation zone was much closer to the centerline than for any of the downstream stations. Clearly, the flow expanded little at this position.

The RMS and turbulence values in the flow core were relatively constant at 8 m/sec (26 ft/sec) and 12 percent respectively (Figs. 29 and 30). The core turbulence was roughly half the value at the 6.4 mm (0.25 in.) location and about the same as at the 12.7 mm (0.5 in.) position. Beyond a nondimensional radius of 1 the turbulence increased drastically to the order of 10^2. Apparently, significant shear was present beyond the oxidizer post shadow. However, as mentioned, no measurements were obtained in the shadow of the fuel annulus where the shear was expected to be greatest.

Since the 1.6 mm (0.063 in.) axial location was close to the injector plane, the central core flow was expected to resemble the fully developed turbulent pipe flow
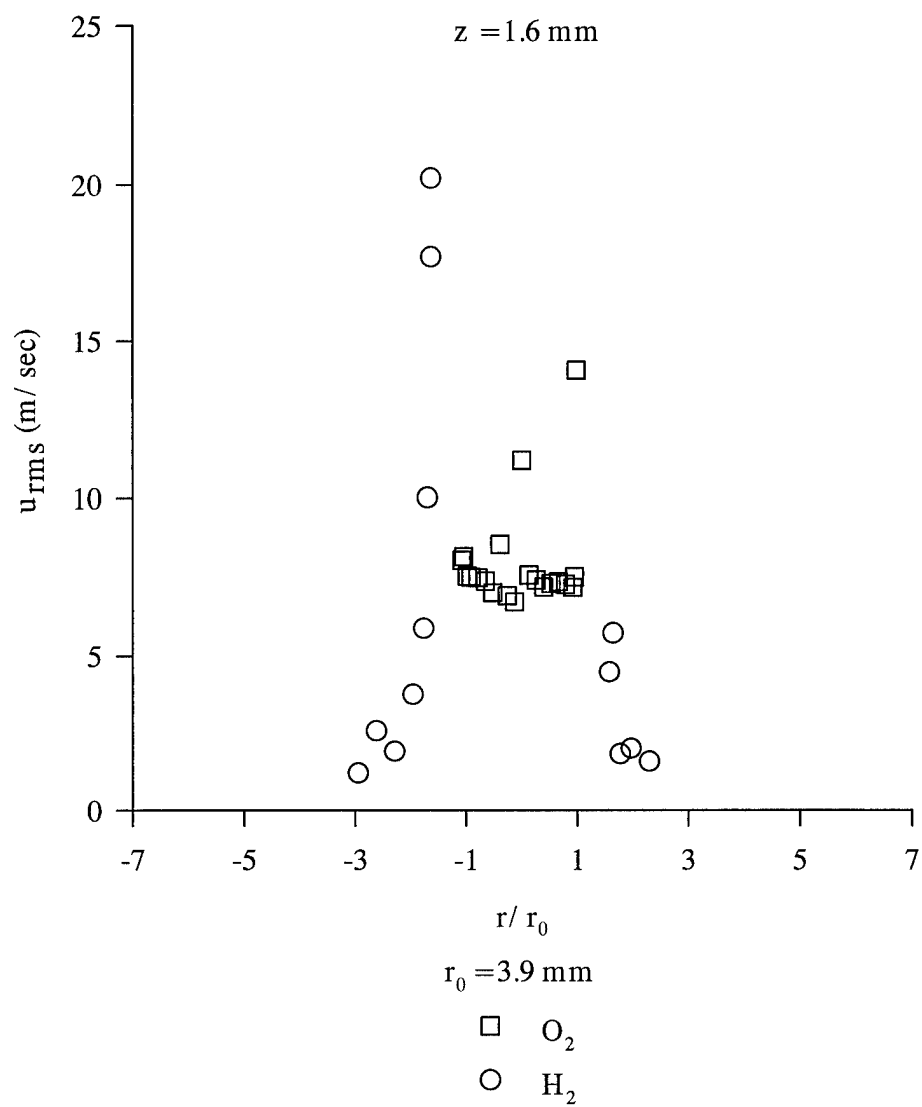
Fig. 29: Hot-Fire Measurements of RMS Velocity at 1.6 mm (0.063 in.) Axial Location
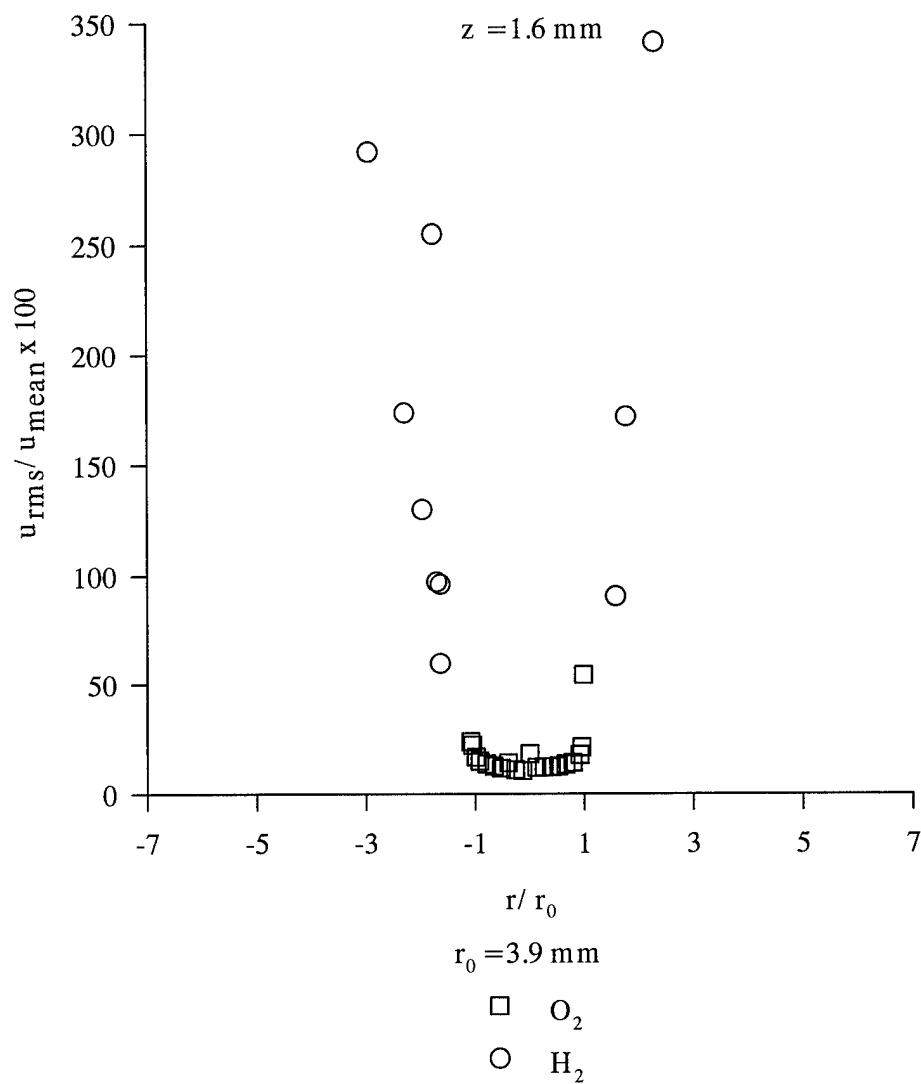
**Fig. 30:** Turbulence Level at 1.6 mm (0.063 in.) Axial Location

within the oxidizer post. The Reynolds number of the GO_2 flow, based on average inlet

temperature and chamber pressure, exceeded 3.3×10^5. Pipe flow becomes turbulent at

Re > 2000 [40]. Thus the core flow velocity profile at the injector exit plane should

closely resemble a fully developed turbulent pipe flow profile.

For fully developed turbulent pipe flow, the ratio of the velocity at any radius to

the maximum velocity (centerline) can be represented by the empirical equation:

$$\frac{u}{U_{CL}} = \left(1 - \frac{r}{r_0}\right)^{\frac{1}{n}} \qquad \text{Eq. 9}$$

where u is the velocity at radius r, U_{CL} is the centerline velocity, and r_0 is the pipe

radius [36]. The ratio of the mean, $\bar{u}$, to the maximum (centerline) velocity is:

$$\frac{\bar{u}}{U_{CL}} = \frac{2n^2}{(n+1)(2n+1)} \qquad \text{Eq. 10}$$

where the exponent $n = 7$ at Re $= 1 \times 10^5$ [36].

Combining the equations yields an expression for the fully developed turbulent

velocity profile in a pipe:

$$u = \bar{u}\frac{(n+1)(2n+1)}{2n^2}\left(1 - \frac{r}{r_0}\right)^{\frac{1}{n}} \qquad \text{Eq. 11}$$

For the 1.6 mm (0.063 in.) hot firings, the mean oxidizer injection velocity, $\bar{u}$, was

59.1 m/sec.

Eq. 10 is plotted along with the measured mean velocity profile in Fig. 31. The

shape of the measured velocity profile conformed fairly well with the predicted turbulent
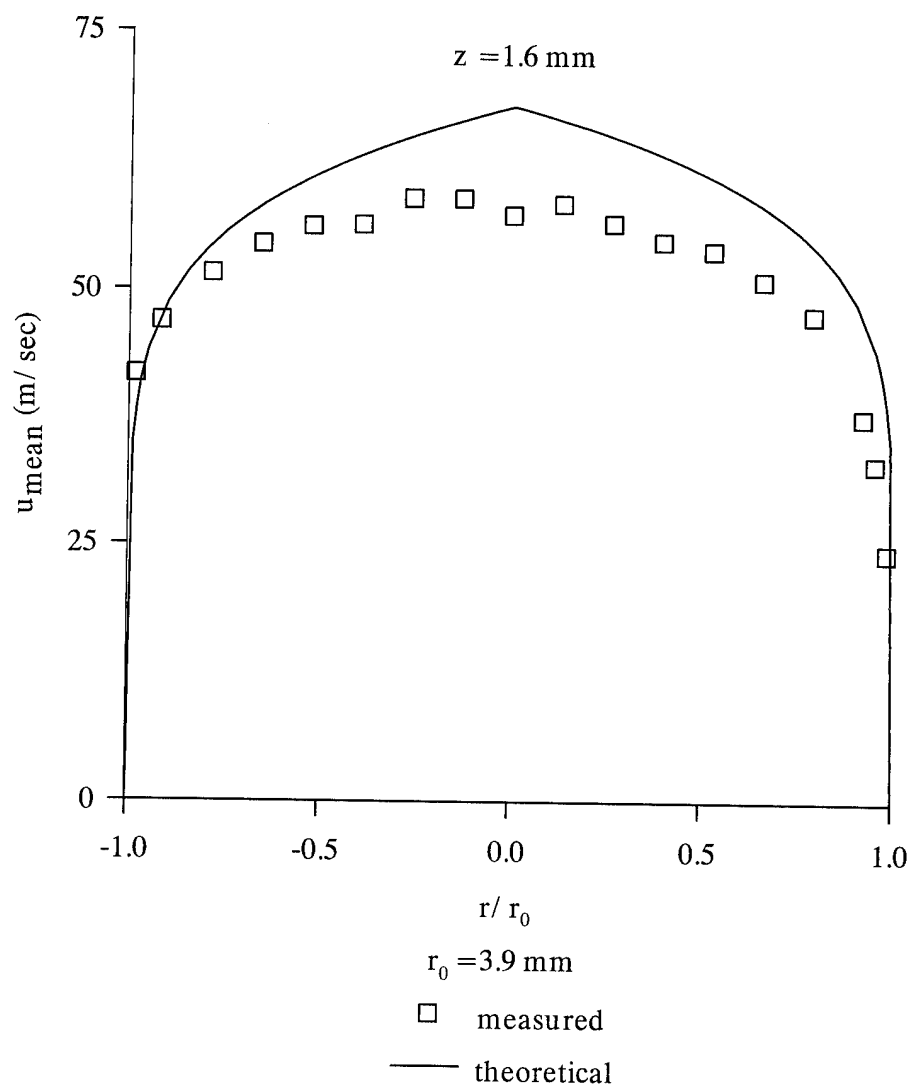
Fig. 31: Hot-Fire Measurements of Mean Velocity of Core Flow at 1.6 mm (0.063 in.) Axial Location Compared to Theoretical Fully Developed Turbulent Pipe Flow

plot. However, the measured centerline velocity was approximately 15 percent less than the predicted turbulent magnitude. In general, the measured velocities were lower than the corresponding predicted turbulent velocities although the differences decreased away from the flow centerline. Misalignment of the probe volume to the chamber centerline could account for some of the difference since shifting the data slightly to the right improves the agreement with the predicted turbulent profile.

In sum, the measured core flow velocity profile did resemble fully developed turbulent pipe flow as expected although the measured velocities were less than predicted for fully developed turbulent pipe flow.

Velocity Bias

None of the preceding data was corrected for velocity or sampling bias effects. The velocities were all calculated from simple ensemble average schemes in which

$$u_{mean} = \frac{1}{N} \sum_{i=1}^{N} u_i \qquad \text{Eq. 12}$$

$$u_{rms} = \left[\frac{1}{N} \sum_{i=1}^{N} u_i^2 - u_{mean}^2 \right]^{\frac{1}{2}} \qquad \text{Eq. 13}$$

where N = the number of samples and u_i = velocity of the ith particle [16].

However, ensemble average schemes can produce velocities significantly different from the true values. Ensemble averages can yield mean velocities which are greater than and turbulence levels which are lower than the unbiased values [16]. McLaughlin and Tiedermann first recognized the potentially significant effect of velocity bias [41]. Durst,

Melling and Whitelaw claim the error in the mean velocity is likely to be less than

10 percent [14]. However, McLaughlin and Tiedermann claimed a bias existed equal to

the square of the turbulence intensity for essentially one-dimensional flows [41, 42].

Since the turbulence intensity in the shear layer between the GO_2 and GH_2 appears high,

velocity bias could be significant for the LDV measurements.

Considerable controversy centers around whether or not to correct for velocity

bias. Johnson, Modarress and Owen cite the lack of conclusive experimental evidence to

support or disprove the existence of bias [43] while Adams and Eaton claim experiments

have substantiated the significance of velocity bias in the turbulent region of free shear

layer flows [44]. Consequently, some researchers have corrected their data for velocity

bias effects and some have not. Driver, Seegmiller and others have foregone velocity

bias corrections due to the "elusive nature" of the problem [43]. Likewise, Merenich

presented his data without velocity bias correction, arguing the effect was minimal due to

the "sporadic" nature in which the data was received and the absence of "evident patterns

indicating velocity biasing" in the data acquisition. Furthermore, Merenich cited the

small change in values associated with the application of a time weighted average

correction scheme to his data as justification for not correcting the ensemble averaged

quantities [9].

Nevertheless, because of the potentially significant impact of velocity bias, it was

decided to investigate the issue. It was also hoped that velocity bias could account for the

discrepancies between the data reported here and by Merenich. Such would be the case if Merenich's data contained a higher amount of bias than the later work.

Velocity bias of LDV measurements results when the particle measurement rate is correlated to the magnitude of the instantaneous velocity vector at a point in the flowfield [44]. The particle arrival rate, and hence the sampling rate, depends on the local instantaneous speed of the fluid at the sensing volume [43]. In other words, higher velocity particles will enter the probe volume more frequently than lower velocity particles for a given period of time and will be recorded more often by a period timing counter than the lower velocity samples [14]. Since more particles per unit time pass through the probe volume during intervals when the fluid velocity is high, the mean calculated by ensemble averaging will be higher than the true mean [45]. The velocity fluctuations responsible for the bias can be either temporal or spatial as seen by the detector [46] and explain why velocity bias may be significant in highly turbulent flows.

Since the collection of velocity information in LDV is statistical with the sampling depending on the occurrences of particles crossing the sensing volume, no bias will result if the particle interarrival times are truly random [43, 47]. Thus, an examination of the particle interarrival times should reveal whether or not velocity bias can be expected in a particular set of data.

The 50.8 mm (2 in.) axial location was examined. Fig. 32 is a plot of the time between data (TBD) samples versus particle velocity for the nondimensional radius $r/r_0 = 1.97$ with the GH_2 flow seeded. The data at this particular location is
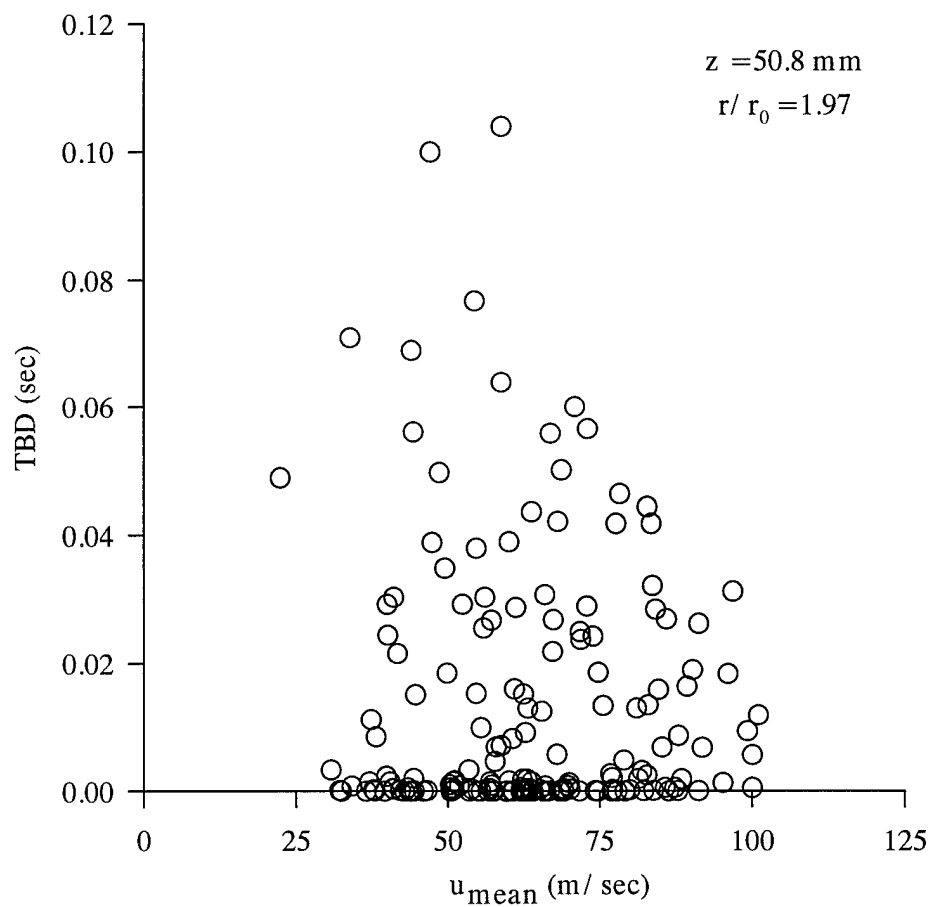
Fig. 32: Time Between Data Samples, GH$_2$ Seeded, 50.8 mm (2 in.) Axial Location, r/r$_0$ = 1.97

representative of the data at other radii and is displayed for illustrative purposes. The plot is not conclusive but appears to reveal a weak dependence of particle interarrival time with velocity, i.e. the faster the particle, the shorter the interarrival particle time. Thus velocity bias could be expected in these data. Merenich's data displayed the same trend. A plot of processor gate time, i.e. the time a particle spends in the sensing volume, versus velocity exhibited the same behavior, suggesting that gate time might also be a factor in the bias.

There are two basic velocity bias correction methods: time dependent (time-weighted average) and time independent (constant time interval) [14, 16, 42, 43, 44]. Considerable controversy exists as to which method is superior. Some claim either one or both can adequately remove the velocity bias [14, 42, 43, 44] while others believe neither method is satisfactory [45]. Attempts to eliminate bias in this work primarily revolved around time weighted averages although a preliminary investigation of the constant time interval approach was also conducted.

The time-weighted average method uses the fact that faster particles arrive more frequently at and spend less time within the probe volume than slower moving particles. The interarrival time or probe volume residence time of each sample is used as a weighting factor for each individual data point [14, 42, 48]. Consequently, the influence of the faster particles will be reduced since their interarrival times or residence times are shorter than for slower particles. The mean and RMS velocities are calculated from:

$$u_{mean} = \frac{\displaystyle\sum_{i=1}^{N} u_i t_i}{\displaystyle\sum_{i=1}^{N} t_i} \qquad\text{Eq. 14}$$

and

$$u_{rms} = \left[\frac{\displaystyle\sum_{i=1}^{N} u_i^2 t_i - \left(\displaystyle\sum_{i=1}^{N} u_i t_i\right)^2}{\displaystyle\sum_{i=1}^{N} t_i} \right]^{\frac{1}{2}} \qquad\text{Eq. 15}$$

where u_i = particle velocity, t_i = the appropriate time interval and N = number of samples [14, 42].

The appropriate time interval for weighting the individual data points is an important consideration in applying the equations.. If t_i is constant, the values reduce to the ensemble averages. In general, however, t_i is not constant and the time-weighted average mean velocity will be less than the ensemble average mean. If t_i is defined as the time to the next available sample, the scheme is termed "sample-hold" and the assumption is the flow velocity does not change significantly between samples. The "hold-sample" approach weights each velocity with the time from the preceding velocity realization. The assumption is the time period before a velocity realization is inversely proportional to the probability of that realization occurring and thus can be used for bias correction [16].

The probe volume residence time can also be the weighting factor in Eqs. 13 and 14. The correct time-averaged statistical quantities of the flow can be obtained since each realization enters the time integral only during the time the particle is present in the measuring volume [48]. Determination of the residence time is complicated by the difficulties associated with defining and measuring the signal durations for Doppler bursts of varying shapes [14]. In this work, the gate time of the processor was taken as the residence time.

Adams and Eaton reported cold flow experiments which they claimed prove time-weighted averaging effectively removed velocity bias. They claimed the time-averaged LDV data agreed with the most accurate conventional measurement techniques to within 5 percent [44].

The time-weighted average method was applied to the 50.8 mm (2 in.) axial location data both for the present work and for Merenich's data. Four different time intervals were used for weighting the data: the time between the sample and the next realization (sample-hold), the time between the sample and the previous realization (hold-sample), the gate time (residence time), and the time between the tenth and eleventh sample after the current sample (referred to as TBD_{10}). The TBD_{10} interval was selected as an arbitrary weighting factor to determine if the correlation was random. The corrections were applied to the specific radii where measurements were made both in the present work and by Merenich to determine if the discrepancies between the two data sets decreased by applying the correction factors.

Figure 33 displays the percent difference of the four weighting factor schemes from the ensemble average mean velocity for the data from the present work. Note that at some radii the bias correction is positive, that is, the velocity is biased toward a lower value than the true velocity. This contradicts the whole concept of velocity bias since the biased measurement should be greater than the unbiased value. The hold-sample correction performed the poorest in this respect while the arbitrary TBD_{10} correction seemed to provide results no worse than the "proper" schemes. The bias corrections ranged from ± 25 percent.

The percent differences between the "unbiased" schemes and the ensemble averages were lowest in the regions where the turbulence was smallest and highest in the outer flow region where turbulence was high. This was consistent with the concept of bias being a function of turbulence intensity. In general, however, the predicted bias was less than the square of the turbulence intensity as postulated by McLaughlin and Tiedermann. Qualitatively, with the exception of the positive biasing, the results agreed with velocity bias theory. Quantitatively, the "unbiased" results cannot be accepted as true due to the presence of positive differences, the wide scatter of results from different weighting factors and the similarity of the arbitrary TBD_{10} results to the others.

Figure 34 reveals similar results for the correction schemes applied to the RMS velocities. Again, some of the bias corrections were positive and some were negative. Removing bias should increase the RMS values. The arbitrary TBD_{10} weighting produced results similar to the other weighting factors. As before, the differences
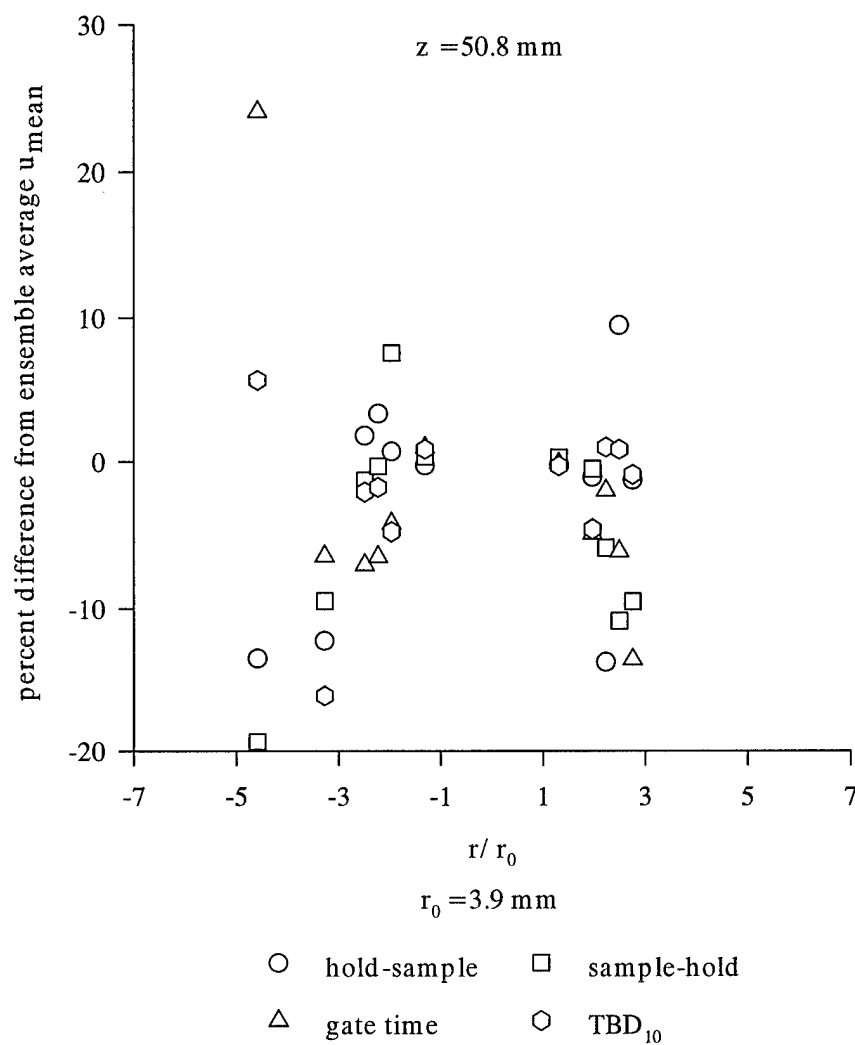
Fig. 33: Mean Velocity Percent Difference of Various Weighting Schemes From Ensemble Average at 50.8 mm (2 in.) Axial Location
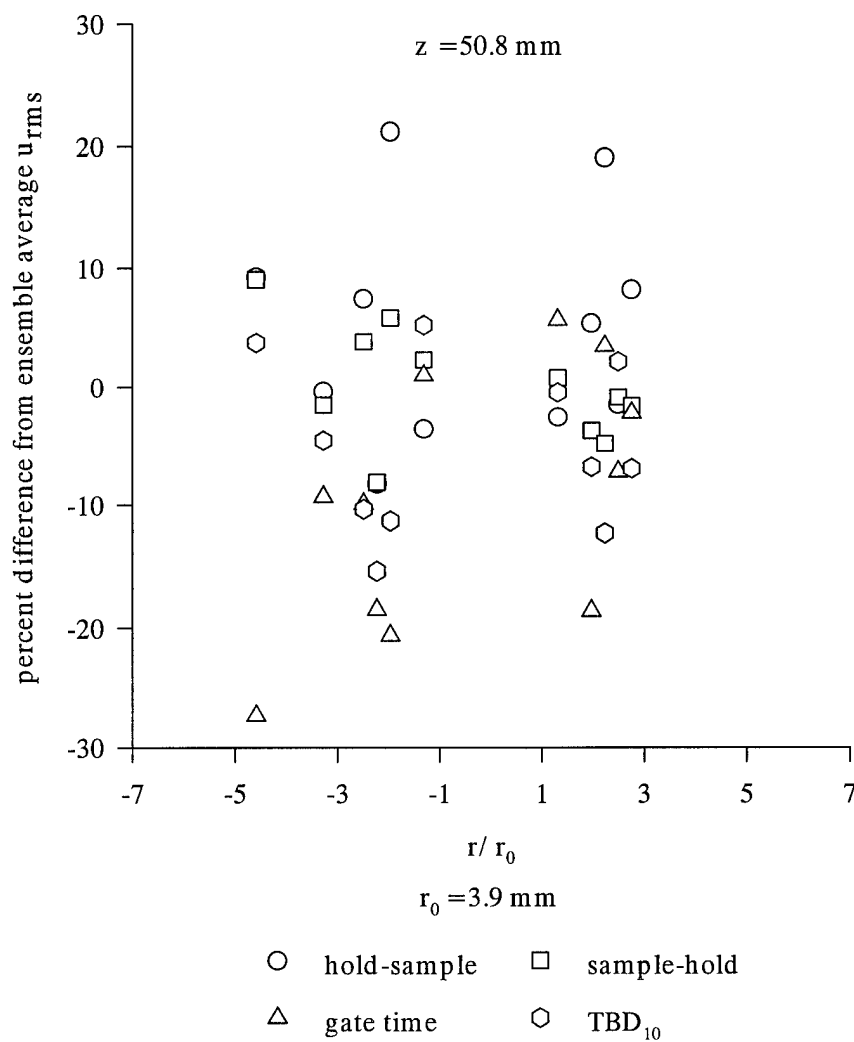
Fig. 34: RMS Velocity Percent Difference of Various Weighting Schemes From Ensemble Average at 50.8 mm (2 in.) Axial Location

between the biased ensemble RMS velocity and the "unbiased" values were smallest in the low turbulence regions and greater in the high turbulence regimes.

The results of applying the time-weighted average correction schemes to Merenich's 50.8 mm (2 in.) data are contained in Figs. 35 and 36. The "unbiased" values were better behaved than in the previously discussed case in that fewer instances of positive correction were noted. Most of these were in the region where turbulence is relatively low and bias should have been small. The arbitrary weighting factor differed more from the "proper" weighting factors than in the previous case. The gate time scheme appeared the best behaved in that the bias correction increased with turbulence intensity more consistently than the others. As for the data described before, the bias corrections were a function of turbulence but the magnitude was less than predicted by the square of turbulence intensity rule-of-thumb.

Applying the time-weighted average schemes to Merenich's RMS velocities was more ambiguous than for the mean velocities. Positive and negative bias corrections were noted within ±12 percent. The trend toward increasing bias with increasing turbulence was present but not as distinct.

Applying the time-weighted average correction schemes to both the data from the present work and from Merenich did not account for the discrepancies between the sets. Each decreased on the order of 10 percent. As explained, it did not appear quantitatively appropriate to apply the corrections to the data from this work. However, Merenich's
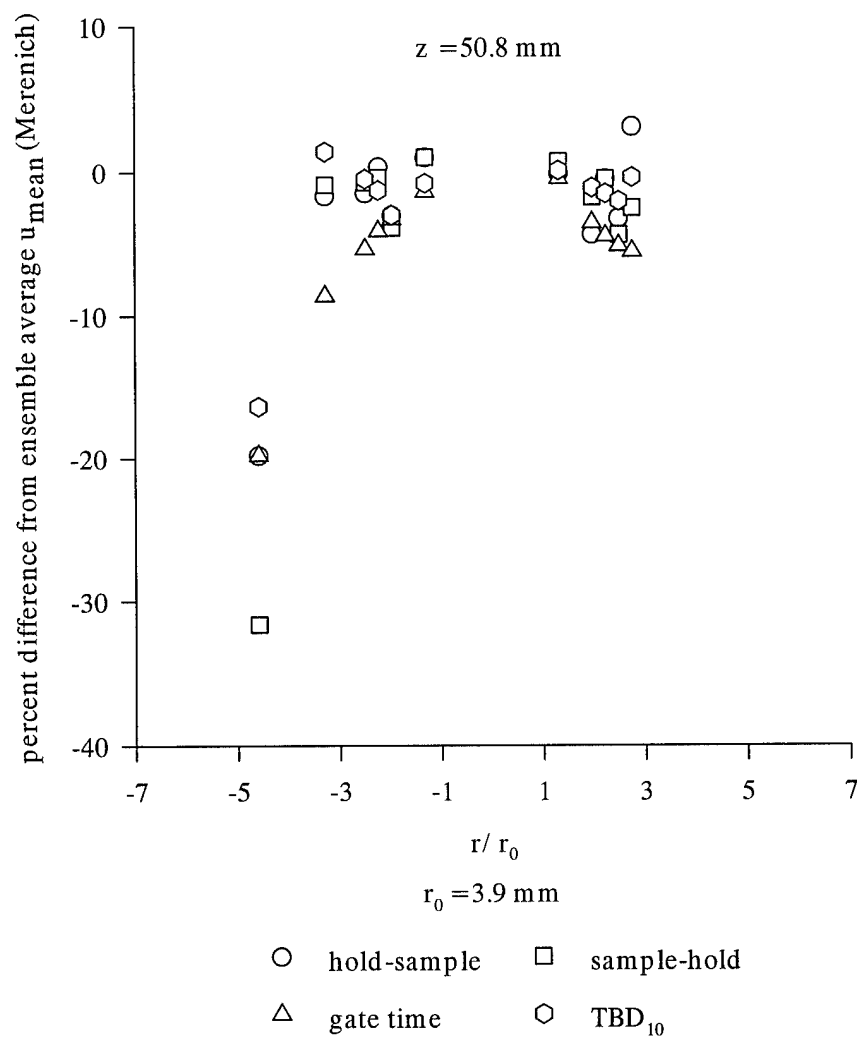
Fig. 35: Merenich Mean Velocity Percent Difference of Various Weighting Schemes From Ensemble Average at 50.8 mm (2 in.) Axial Location
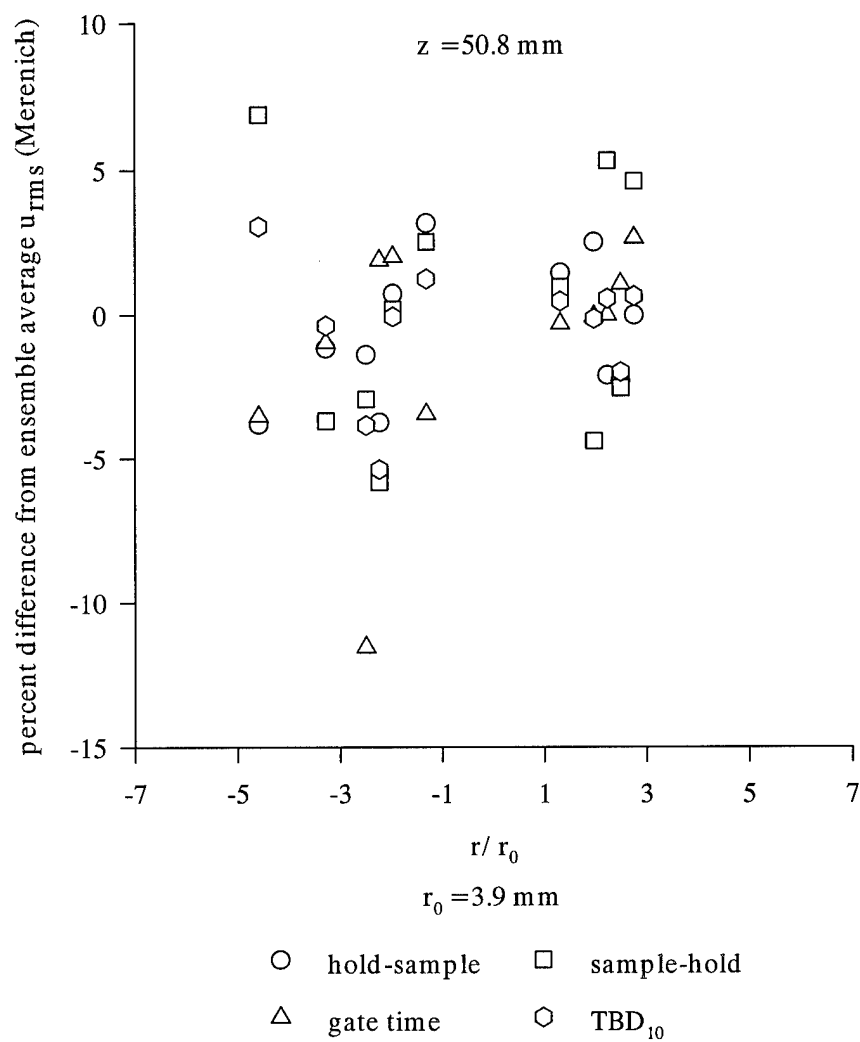
Fig. 36: Merenich RMS Velocity Percent Difference of Various Weighting Schemes From Ensemble Average at 50.8 mm (2 in.) Axial Location

data appeared to respond more "correctly" to the bias corrections. If the corrections are applied to Merenich's but not the later data, the discrepancies between the data sets becomes less than 10 percent. The question then becomes whether or not it is proper to apply the bias corrections to Merenich's work but not the current effort.

The signal-to-noise ratio (SNR) criterion differed in the collection of the two sets of data. Merenich used a minimum SNR acceptance criterion of 0.3 whereas the present work specified 0.6 to produce more distinct Doppler bursts. Therein could lie the reason for the discrepancy. Raising the SNR could selectively eliminate high velocity samples since slower particles produce higher SNRs than faster ones [43, 49]. In fact, most of the data samples rejected during the hot firings failed to meet the SNR criterion. Considering all available signals maximizes the possible bias. Durão and Whitelaw claim bias will be reduced when the collection percentage is low [50]. Thus, the bias would be reduced or eliminated by selectively eliminating faster particles.

Examination of the data revealed that Merenich obtained particle percent validation rates as much as four times greater than in this work. In general, the validation rates for the two data sets were similar in the GO_2 flow and significantly different in the GH_2 outer flow. Figure 37 shows that the percent difference in the mean ensemble velocity between Merenich's and this work decreased as the ratio of particle valid percentage approached one. The differences in the mean velocities were largest for the greatest differences in the percent validation rates. Consequently, the argument can be made that the lower SNR used in Merenich's data collection produced higher
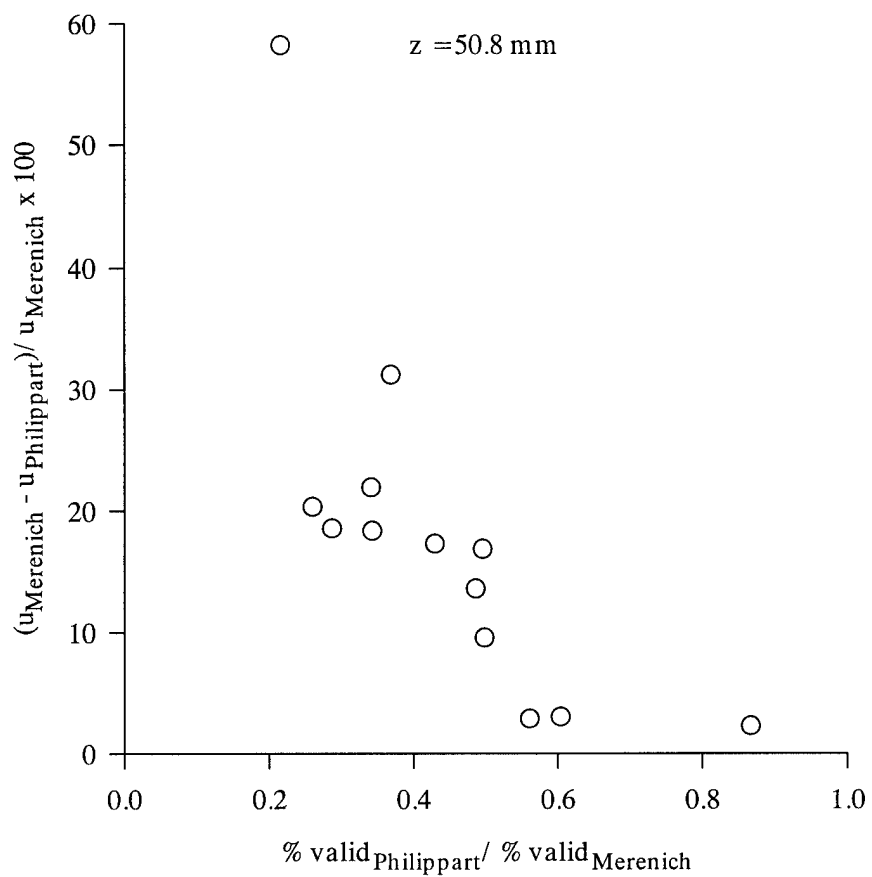
Fig. 37: Difference in Mean Velocity at 50.8 mm (2 in.) Axial Location vs. Ratio of Percent Valid Samples

validation rates and therefore, mean velocities which are more velocity biased than the data collected in this work. Qualitatively speaking, the velocities from the present work may lie closer to the true values [22]. Quantitatively, the magnitude of the bias in the later data was not satisfactorily determined from time-weighted methods.

Since time-weighted methods did not appear suitable for removing velocity bias in these data sets, a constant time interval method was briefly studied. As the name implies, a constant time interval approach eliminates the dependency of particle arrival rate on velocity by selecting only a subset of data at periodic intervals. Simpson and Chew suggested that constant time interval data sampling will eliminate velocity bias and the density bias which results from unequal seeding densities in 2 mixing flows [51, 52]. Therefore, basic ensemble average equations can be used without bias [14, 44].

Three basic types of constant time interval method are used: delayed search, forward search and center search [16].

In the delayed search routine, samples are extracted from the sample set at a specified fixed time interval. If no velocity realization is present at the specified time, the algorithm marches forward in time until a sample is recorded. The time error is noted and a new reference time for future marching is established. The process is repeated until the entire randomly-arrived, primary velocity sample set is filtered. The disadvantage of this approach is that each accepted velocity realization defines a new reference time and thus is not the best approach to constant time interval sampling [16].

The remaining two approaches select velocity realizations at a specified time but use an acceptance window criterion if no realization is present at the exact sampling interval. The forward search technique selects the earliest velocity realization within the acceptance window *after* the sampling time is reached. Conversely, the center search method selects the velocity realization within the acceptance window *closest in time* to the specified sampling interval, whether it be before or after the time. No sample is recorded if no velocity realizations lie within the acceptance window and the original time reference is maintained throughout [16].

The forward and center search techniques are highly sensitive to the width of the acceptance window. Nejad and Davis detail in depth the relationship between acceptance window width, sampling rate and seeding rate [16].

The Aerometrics PDPA software contains a constant time interval algorithm for eliminating velocity bias. The algorithm selects a subset of the raw data based on the input parameters of specified interval time and width. Mean ensemble average velocities are calculated from the subset of the raw data [17].

The 50.8 mm (2 in.) axial location data was examined at several radial positions with the Aerometrics software using various interval times and widths. The "corrected" velocity values were highly sensitive to the input parameters. Time intervals in the range 0.01-1 msec and interval widths of 1-20 µsec were tried. Some combinations of time and width produced "unbiased" values greater than the ensemble averages similar to the case for the time-weighted schemes. Other combinations of input time and width resulted in

"unbiased" values that were virtually identical to or at most 5 percent less than the ensemble values.

The presence of the unrealistic positive bias corrections and the inconsistent nature of the "unbiased" results suggested that applying the algorithm to the data was inappropriate. This was likely due to the small sample size of the data sets. Many of the raw data files only contained a few hundred valid samples. Selecting a subset reduced the sample size even further, probably to the point of statistical insignificance.

Nonuniform Seeding

Most velocity bias correction schemes assume uniform particle seeding. An examination of the data revealed the actual nonuniformity during the firings. Velocity realizations occurred in bursts, perhaps as clumps of seed were introduced into the flow. The behavior is apparent in Fig. 38, a typical plot of gate time versus run time for Merenich's data. Each gate time symbol represents a velocity realization. Clearly, the velocity realizations and hence, the flow seeding were not temporally uniform. The current work displayed the same trend with the exception that the realization bursts were not concentrated in the first half of the run time. This difference may have been due to the valve in the flow seeding system which was present in this work but not for Merenich's tests.

To investigate the influence of this seed burst behavior, the sample sets were divided into two parts containing an equal number of realizations. The time-weighted average schemes from before were reapplied to each half. Overall, each half produced
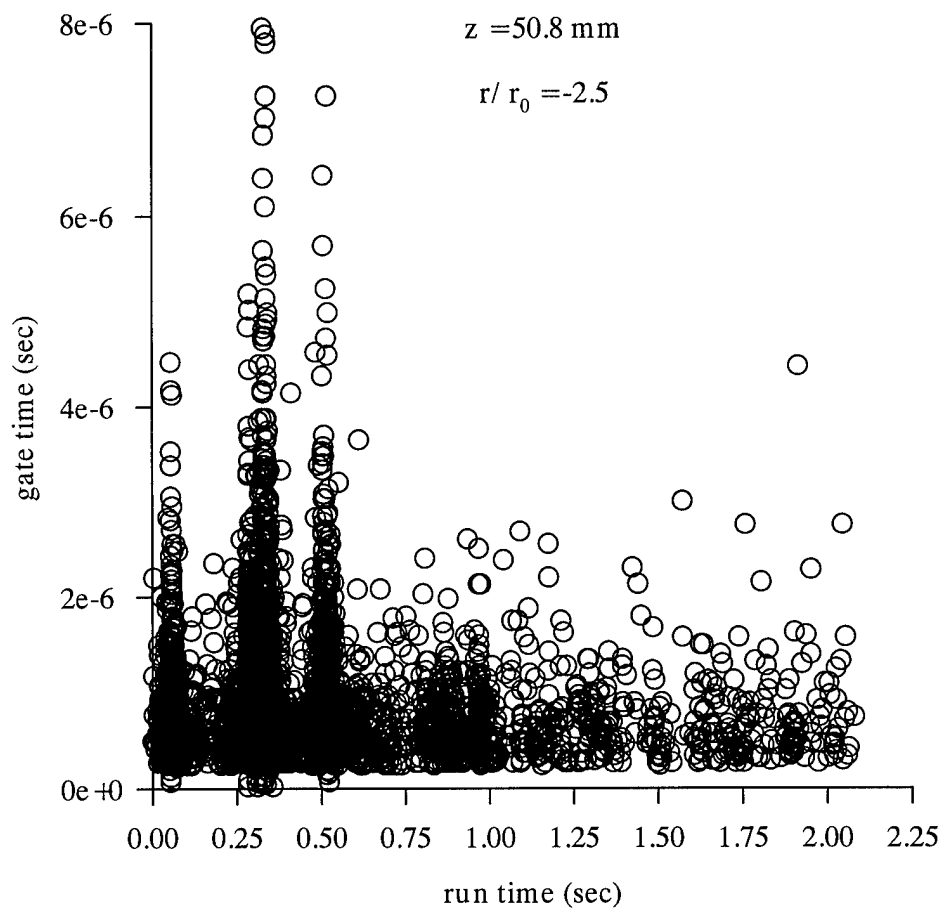
Fig. 38: Merenich Velocity Realization Bursts at 50.8 mm (2 in.) Axial Location, H_2 Seeded, $r/r_0 = -2.5$

"unbiased" velocities which were within a few percent of each other and the previous full sample set values. Therefore, while the temporal nonuniformity of the seeding violated an assumption of the bias correction schemes, it does not fully explain the inconsistent results obtained with these methods.

To recap, no method of eliminating bias examined in this effort appeared appropriate for the data. However, the reduced SNR suggested that the data from this work was less biased than Merenich's data. Nevertheless, no additional attempt was made to eliminate velocity biasing and the ensemble averages were retained.

Figures 39 and 40 display all the mean and RMS velocity profiles side-by-side for completeness. The 25.4 mm (1 in.), 50.8 mm (2 in.) and 127 mm (5 in.) profiles are from Merenich while the others are from the work described herein.

Temperature Measurements

Temperature measurements were made within the uni-element coaxial injector flowfield and within the combustion chamber itself.

Injector Temperatures for GH_2/GO_2

Four GH_2/GO_2 hot firings were conducted with the thermocouple-instrumented shear coaxial injector. The average thermocouples temperatures for the firings are superimposed on the injector schematic in Fig. 41.
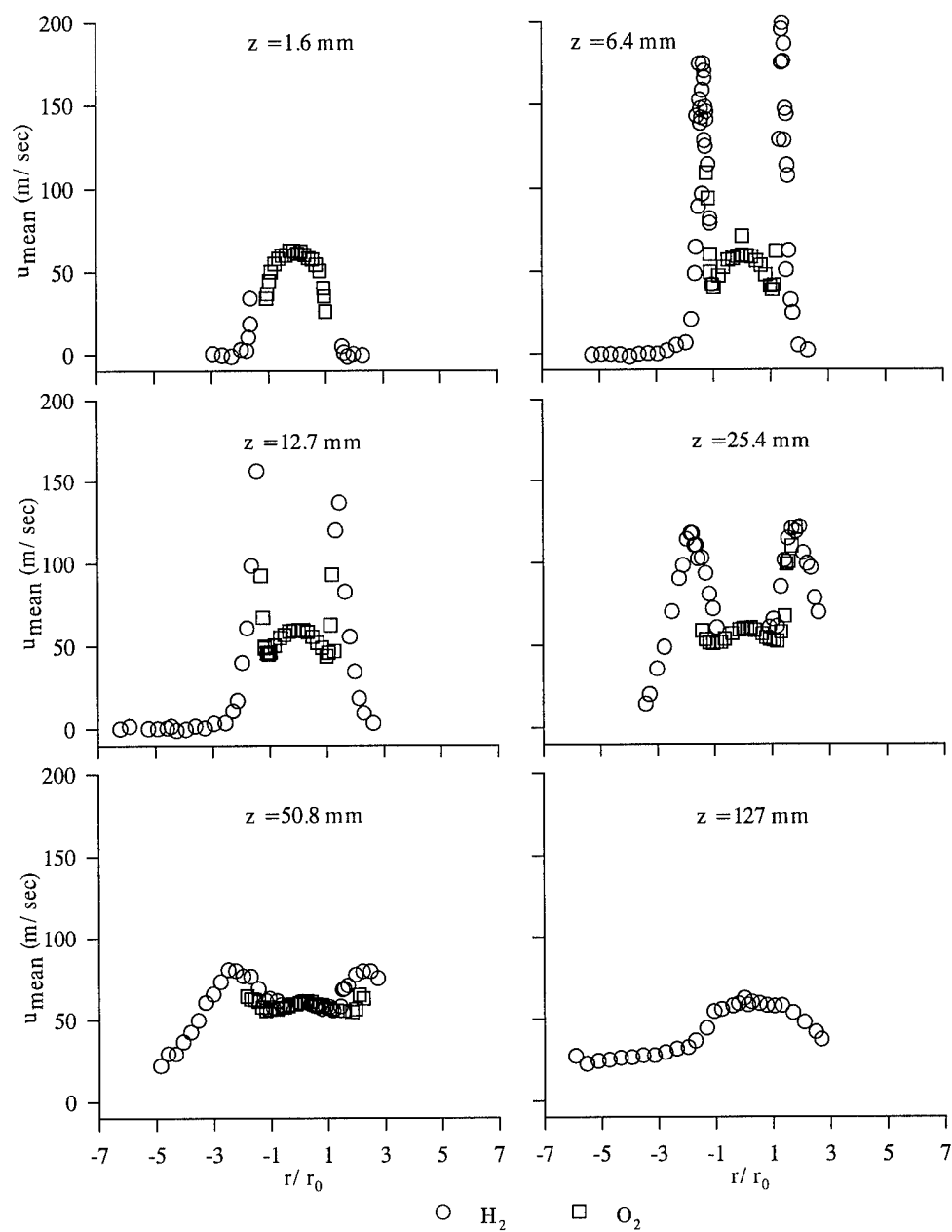
Fig. 39: Hot-Fire Measurements of Mean Velocity at Various Axial Locations
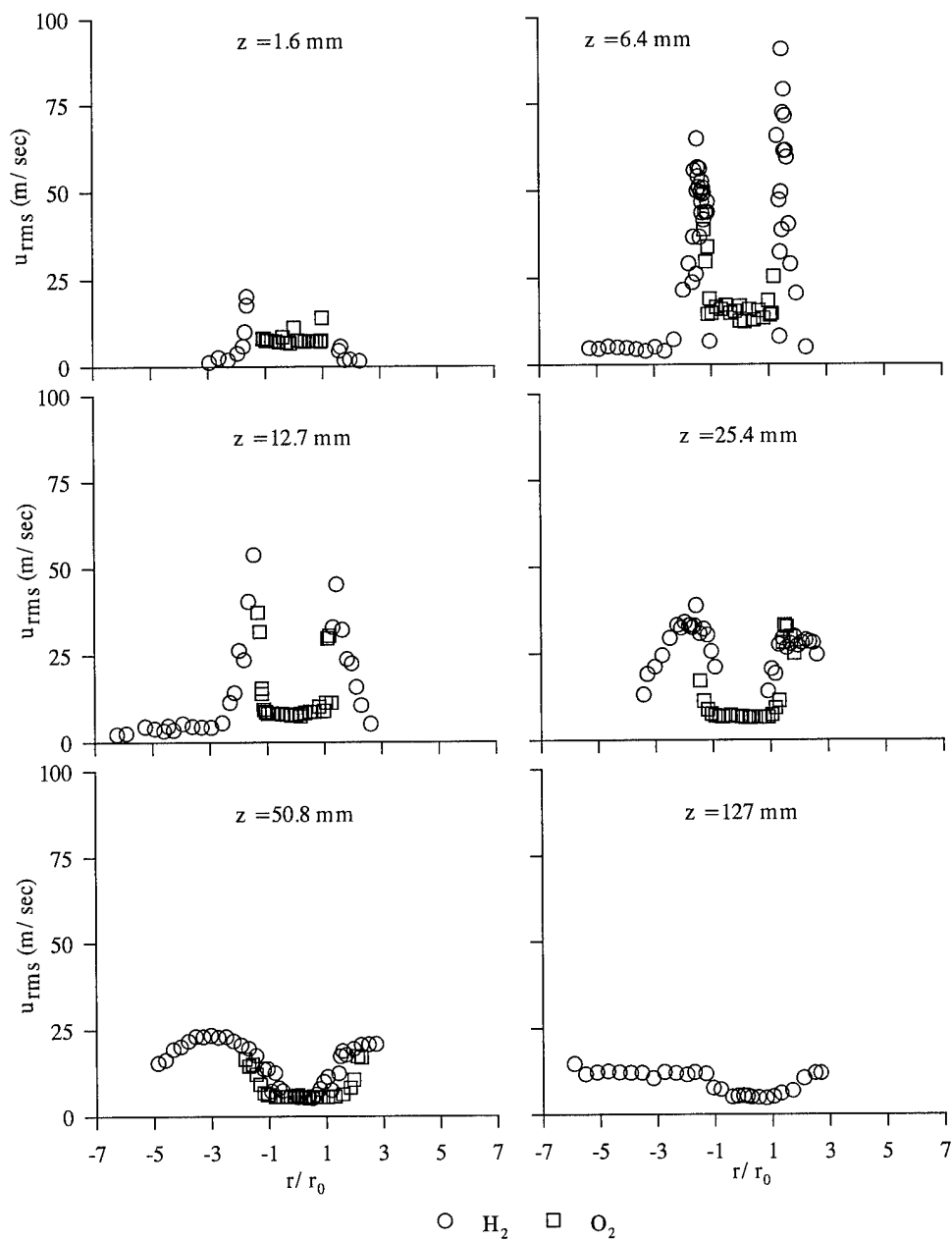
Fig. 40: Hot-Fire Measurements of RMS Velocity at Various Axial Locations
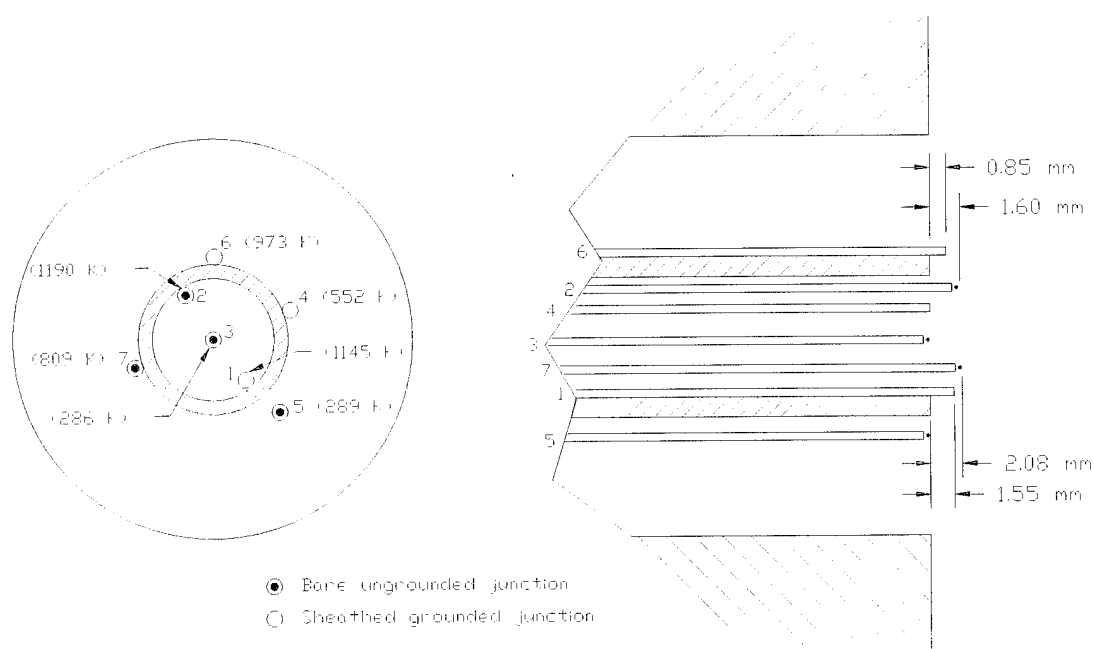
Fig. 41: Average Shear Coaxial Injector Thermocouple Temperatures for GH_2/GO_2 Hot-Firings

The thermocouple configuration was satisfactory for measuring the injector temperatures. Visible light photographs revealed the thermocouples glowed during the firings but none were saturated or destroyed by the flame.

The temperature measurements illuminated details of the flowfield. The bare thermocouples near the center of the oxidizer post and fuel annulus recorded the injection temperatures of the respective gaseous propellants and established the exit plane boundary conditions. The temperatures on the outer periphery of the oxidizer post (thermocouples 6 and 7) were approximately the same after taking into account the different thermocouple lengths and sheaths. The highest temperatures were recorded on the inner periphery of the oxidizer post (numbers 1 and 2). The temperatures recorded on the outer and inner peripheries of the oxidizer post were high but beneath the 3470 K stoichiometric flame temperature of GH_2/GO_2 [29] indicating that the thermocouples were not immersed in the flame. The visible flame appears bracketed by the peripheral thermocouples. Thus, the flame could have been anchored on the lip of the oxidizer post.

The injector hot-firings established the exit plane boundary conditions for the flow and proved the feasibility of measuring temperatures near the flame with sheathed and bare wire thermocouples.

Temperature Rake Hot-Fire Measurements

Air/GH₂ firings

The temperature rake was first tested in hot-firings with air and gaseous hydrogen propellants. It was ultimately desired to use the rake in LOX/GH_2 firings but was

considered prudent to test the probe in the more benign air/GH$_2$ environment first. The injector for this series was the same as in the LDV and injector thermocouple tests.

Measurements were made with the probe inserted at three axial locations downstream of the injector: 76.2 mm (3 in.), 127 mm (5 in.) and 152.4 mm (6 in.). A total of 31 firings were made with the air/GH$_2$ propellant combination. The thermocouple measurements were averaged during the steady-state portion of the firing to eliminate the temperature spikes associated with ignition and shutdown.

Figure 42 displays the averaged results from all tests. The radius has been nondimensionalized by the radius of the oxidizer post (3.88 mm/0.153 in.). The temperatures are as reported by the thermocouples and have not been corrected for the effects of thermocouple length etc. Note that only five or six points were measured at each location since two thermocouples ceased functioning during the firings.

The profiles revealed an asymmetric temperature distribution analogous to the asymmetric velocity profiles from the LDV tests. In general, higher temperatures were observed below the centerline ($r/r_0 < 0$) than above. The minimum temperature was noted near the centerline for the two profiles at which data was available.

The temperatures increased with increasing downstream axial distance as expected since the combustion and mixing of the hot gases would be more complete downstream.

The asymmetry and centerline minimum temperature behavior for the 127 mm (5 in.) location was consistent with Raman-derived temperatures at the same
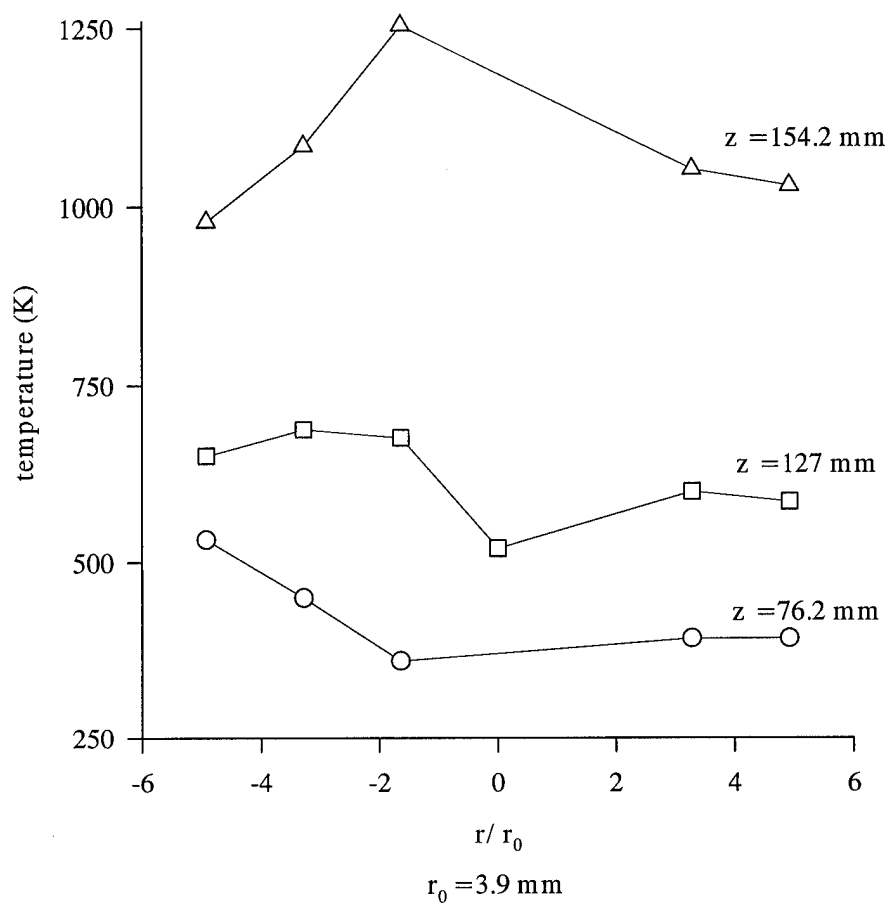
Fig. 42: Temperature Profiles for Air/GH$_2$ Firings at Three Axial Locations

conditions [53]. Thus, the temperature rake was useful as an independent measurement tool and validation device for non-intrusive methods.

The prefire heat transfer analysis proved adequate. The water outlet temperature rose approximately 17 K during the firings. Calculations with FLUENT predicted a bulk temperature rise of between 5 and 10 K [2]. Thus, confidence was high that the temperature rake could function and survive in the harsher LOX/GH_2 environment as predicted by the heat transfer analysis.

Two of the seven thermocouples quit working during the previous test series so a new probe was built. Larger diameter (0.813 mm/0.032 in.) thermocouples were substituted to make the rake more robust and prevent future failures [54].

LOX/GH₂ firings

Measurements were taken for LOX/GH_2 firings at an axial location of 76.2 mm (3 in.) and O/F = 166. The firings utilized a swirl coaxial injector as described by Rahman, et. al [55]. A problem was encountered during the prefire period. In preparation for firing the rocket, LOX flowed through the propellant line into the chamber to cool the line and purge any remaining GO_2. However, the rake coolant outlet thermocouple indicated that the water froze during this prefire period. As a result, the rake only approached steady-state temperatures during a one second period near the end of the firing sequence. The outlet water temperature remained constant, suggesting that the water line did not completely thaw during the firing. Only one firing successfully produced temperature data in this test series.

The results are plotted in Fig. 43. Note that all of the thermocouples functioned, vindicating the decision to switch from 0.508 mm (0.020 in.) to 0.813 mm (0.032 in.) diameter thermocouples. The radii were nondimensionalized by the radius of the LOX post. The temperature asymmetry seen in previous firings was again apparent and even more distinct. Buoyancy effects could be involved in this asymmetry since upon injection the cold LOX would tend to sink, mix and combust more thoroughly with the GH_2 below the centerline.

The minimum temperature was recorded above ($r/r_0 = 3.3$) rather than at the centerline as in the air/GH_2 test series. The peak LOX firing temperature was slightly less than but comparable to the peak for the air/GH_2 firings at the same axial location.

Because of the unanticipated freezing of the coolant during the prefire cool down phase, it was decided to replace the water with gaseous nitrogen (GN_2). FLUENT calculations revealed that sufficient GN_2 mass flow could be provided to cool the probe [2]. Therefore, the next test series utilized GN_2 cooling.

Firings were made with the coaxial swirl injector operated at the maximum oxidizer flow rate of 0.45 kg/sec (1.0 lb./sec) producing O/F = 100. Since this was a lower O/F than before, the probe was placed further downstream than previously (127 mm/5 in. versus 76.2 mm/3 in.) to try to prevent direct LOX impingement.

Unfortunately, the probe was destroyed during the first hot-firing. The end fittings were all that remained of the probe and were burned almost flush with the chamber walls. No other traces of the probe were found either in the combustion
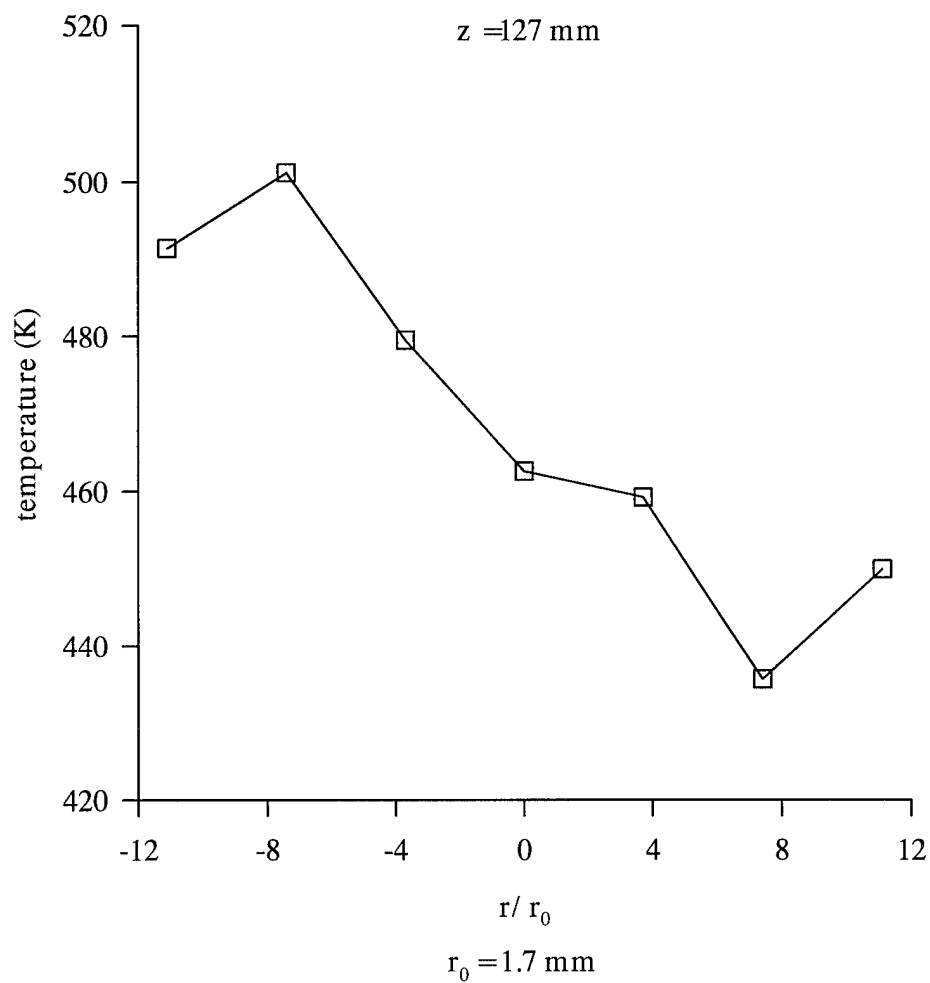
Fig. 43: Temperature Profile for LOX/GH$_2$ Firing (O/F=166) at 76.2 mm (3 in.) Axial
Location

chamber or the test cell area. All thermocouples reported temperatures of ≈1500 K,

(i.e. the saturation temperature of Type K thermocouples) prior to their destruction.

Examination of the test videotape was revealing. An orange flash in the chamber at the rake location was seen approximately one second into the combustion sequence. The plume had an orange tint as the probe was consumed for the next two seconds. A slight dip in chamber pressure corresponded to the cessation of the orange flashes. An increase in the GN_2 outlet temperature coincided with the onset of the flashes. The nitrogen supply pressure gage jumped to roughly chamber pressure, apparently as the probe tube was breached and backpressure from the chamber entered the coolant line.

Examination of the coolant outlet temperature indicated the GN_2 reached a steady-state temperature of 386 K. The temperature stabilized for almost the first full second of the firing after which it rose dramatically to 600 K and then decreased as the GN_2 stopped flowing. FLUENT calculations indicated the GN_2 steady-state temperature should have been around 417 K [2]. The probe did not appear to have overheated globally since the coolant temperature had ceased climbing and was within 7 percent of the predicted steady-state temperature. The bulk coolant outlet temperature was below the melting points of brass and silver solder [56].

The exposed thermocouple tips may have ignited and destroyed the rake [57]. The thin, stainless steel-sheathed tips may have acted as wicks and ignited in the corrosive oxygen-rich environment. The rake tube may have been breached when the thermocouples burned back causing rapid destruction of the probe.

A temperature rake was exposed to an acetylene cutting torch to test this hypothesis. The protruding thermocouple tips were heated until glowing and then oxygen was applied from the cutting jet. The thermocouples combusted violently when exposed to the oxygen. The surrounding brass tube became extremely hot but did not ignite. Therefore, it appeared reasonable that the thermocouple tips burned back and breached the probe tube wall. When the hot combustion chamber gases entered the probe, coolant flow ceased and the probe's mechanical integrity was quickly compromised. The available evidence was consistent with this hypothesis.

The destruction of the temperature rake terminated the test series for this effort.

Chapter 4

SUMMARY AND RECOMMENDATIONS

Summary

The major objectives of this research were accomplished. The LDV velocity

measurements were extended to axial locations closer to the injector than the preceding

work of Merenich. A thermocouple-based temperature rake was constructed and the

feasibility of its use in the rocket chamber was established.

Profiles of mean velocity, RMS velocity and turbulence intensity were produced

for rocket firings using GH_2/GO_2 propellants at axial locations of 1.6 mm (0.063 in.),

6.4 mm (0.25 in.), 12.7 mm (0.5 in.), 25.4 mm (1 in.) and 50.8 mm (2 in.). The latter two

profiles were collected to examine the reproducibility of Merenich's data.

A significant amount of effort went into attempting to reproduce the data obtained

by Merenich. Numerous firings confirmed the qualitative behavior and shapes of the

profiles reported by Merenich at the 25.4 mm (1 in.) and 50.8 mm (2 in.) axial locations

but were unable to obtain the same peak velocity magnitudes. In general, the maximum

velocities reported here were 10 to 20 percent lower than the peak values reported by

Merenich for the same positions.

Several different sizes and batches of aluminum oxide particles were used to seed

the flow in the hope of accounting for the discrepancies from Merenich's data. Cold-flow

simulations were promising since differences were seen in the velocity measurements

depending on the particular particles seeding the flow. It was hoped that using particles of slightly larger nominal size would decrease agglomeration and allow better flow tracking. However, the hot-fire results for the various seed particles were virtually identical and were still lower than reported by Merenich. The hot-firings in this study were self-consistent and thus call into question the validity of Merenich's data.

Additional attempts to explain the discrepancies from Merenich's data involved an in-depth examination of velocity bias. Application of both time-weighted average and constant time interval methods produced inconclusive results. The data sets did not appear suited for these bias correction schemes. Quantitatively, the amount of velocity bias could not be determined. Qualitatively, however, an argument was made that the data from this effort was less biased than that obtained by Merenich due to the higher SNR criterion specified in the later data collection.

The near-injector measurements revealed additional characteristics of the rocket flowfield. Asymmetries were noted at all profiles with higher velocities generally occurring below the chamber centerline. The shear layer between the hydrogen flow and the oxygen core flow was characterized by high levels of turbulence. The central flow in the proximity of the injector closely resembled turbulent pipe flow. Recirculation zones existed near the chamber walls and became smaller as the flow evolved downstream. The combusting flow region expanded with increasing axial distance.

A thermocouple-instrumented coaxial injector was fired with GO_2/GH_2 propellants and temperature measurements taken. The measurements supported the concept that the flame was anchored to the lip of the oxidizer post.

The feasibility of a thermocouple temperature rake was established. Comparison with reference flame measurements was satisfactory. Tests were made with the water-cooled probe inserted at three axial positions for air/GH_2 firings. The tests revealed asymmetric temperature profiles with higher temperatures generally lying below the chamber centerline analogous to the velocity asymmetries. The measured temperatures increased with increasing axial distance as expected due to more complete mixing and combustion downstream. The temperature profile at the 127 mm (5 in.) axial location agreed qualitatively with Raman-derived temperatures at the same hot-fire conditions.

The water-cooled probe experienced difficulty in a LOX/GH_2 environment. The water coolant froze during the prefire cool-down phase and the rake only reached steady-state temperatures for a small portion of the firing. The 76.2 mm (3 in.) axial results were comparable to the air/GH_2 tests and once again, revealed a temperature asymmetry.

The rake was reconfigured for GN_2 cooling and placed in a high mass flow LOX environment. The probe was destroyed during the first hot-firing and no temperature profile was taken. Analysis of the data suggested the probe did not overheat globally but was consumed when the thermocouple tips ignited and burned through the tube wall possibly due to the extremely oxygen-rich environment.

Recommendations for Future Work

The influence of SNR on the mean velocities should be examined to determine if the discrepancies between the data from this work and Merenich can be explained. One approach is to repeat the velocity measurements at the same axial locations and flow conditions while saving the raw data buffers during the data acquisition. The data can then be post-processed to examine the effects of SNR and other data acquisition parameters [17]. This was not done previously due to the large storage space required.

Clearly, seeding the flow is difficult. The data revealed inadequacies in the seeding system since particles entered in bursts rather than smoothly throughout the firing. Controlling the amount of seed with precision and repeatability was virtually impossible. Undoubtedly, the nonuniformities affected the measurements [42].

The problem of adequately dispersing seed particles in gaseous flows has not been satisfactorily addressed by anyone [31]. Fluidized bed seeders are prone to large fluctuations in particle concentration [24]. Nevertheless, improvements might be possible by reconfiguring the seeder into a reverse flow cyclone separator design [58]. Some success has been reported using cyclone separators [59] but other problems such as particles being "channeled out" from the center of the seeder may arise [60]. An improved seeder design with ball mill grinding to reduce clumping within the seeder is possible but presents safety concerns when working with GO_2 flows. Thus, a reverse cyclone separator appears to be the simplest modification to promise improved seeding.

A commercial-grade aluminum oxide abrasive may not be the best material for LDV flow seeding. The nonsphericity of abrasives promotes agglomeration and poor flow tracking [31]. A laboratory grade of Al_2O_3 may improve the flow seeding and hence, the LDV measurements. Likewise, other materials such as sub-micron ZrO_2 may be better suited for combusting flow measurements [20]. However, finding a low-cost supply of such materials may be difficult.

The practicality of *in-situ* temperature measurements with a thermocouple-based temperature rake was established. Probe survivability was not an issue in an air/GH_2 environment but LOX environments present a severe threat to the survival of the probe. Consequently, suitability of the temperature rake for LOX environments must be evaluated on a case-by-case basis.

Probe survivability could possibly be enhanced by shortening the distance the thermocouples protrude beyond the cooling tube or by using larger diameter thermocouples. However, larger diameters would increase the response time so a balance must be struck between survivability and measurement requirements.

Changing the LOX flow rates or injector configurations can be expected to significantly alter the probe's survivability. Occasional probe failures and destruction can be expected. Given the relatively low cost of fabricating the rakes ($\approx$ \$300), the risk of destruction should be a relatively small price to pay for gathering temperature data.

REFERENCES

1. Foley, T. M., "Mr. Goldin Goes to Washington," *Air & Space Smithsonian, Vol. 10, No. 1,* Smithsonian Institution, Washington, DC, April/May 1995.

2. Anon., *FLUENT Manual Version 2.9 Update,* Creare, Inc., Hanover, NH, 1987.

3. Schuman, M. D. and Beshore, D. G., *Standardized Distributed Energy Release (SDER) Computer Program Final Report,* AFRPL-TR-78-7, 1978.

4. Muss, J. A., Nguyen, T. V. and Johnson, C. W., *User's Manual for Rocket Combustor Interactive Design (ROCCID) and Analysis Computer Program, Vol. 1,* NASA Contractor Report 1087109, May 1991.

5. Liang, P. and Schuman, M. D., "Atomization Modeling in a Multiphase Flow Environment and Comparison With Experiments," AIAA Paper 90-1617, AIAA 21st Fluid Dynamics, Plasma Dynamics and Lasers Conference, Seattle, WA, 18-20 Jun 90.

6. Venkateswaran, S., Weiss, J. M., Merkle, C. L. and Choi, Y. H., "Propulsion-Related Flowfields Using the Preconditioned Navier-Stokes Equations," AIAA Paper 92-3437, AIAA/SAE/ASME/ASEE 28th Joint Propulsion Conference and Exhibit, Nashville, TN, 6-8 Jul 92.

7. Santoro, R. J. and Merkle, C. L., "Research Proposal: An Experimental Study of Characteristic Combustion-Driven Flow for CFD Validation," NRA-90-MSFC-1.

8. Moser, M. D., Merenich, J. J, Pal, S. and Santoro, R. J., "OH-Radical Imaging and Velocity Field Measurements in a Gaseous Hydrogen/Oxygen Rocket," AIAA Paper 93-2036, AIAA 29th Joint Propulsion Conference and Exhibit, Monterey, CA, 28-30 Jun 93.

9. Merenich, J. J., *Laser Doppler Velocimetry in an Optically Accessible Gaseous Hydrogen/Oxygen Rocket,* Masters Thesis, The Pennsylvania State University, University Park, PA, May 1994.

10. Moser, M. D., Pal, S. and Santoro, R. J., "Laser Light Scattering Measurements in a GO_2/GH_2 Uni-Element Rocket Chamber," AIAA Paper 95-0137, 33rd Aerospace Sciences Meeting and Exhibit, Reno, NV, 9-12 Jan 95.

11. Moser, M. D., *Flowfield Characterization in a Uni-Element Rocket Chamber,* Doctoral Thesis, The Pennsylvania State University, University Park, PA, May 1995.

12. Boylan, D. M., "Gas Velocity and Temperature Near a Liquid Rocket Injector Face," NASA CR-12100, NASA Lewis Research Center, OH, Jan 73.

13. Carbon, M., Albert, R. J., and Hawkins, G. A., "The Measurement of Gas Temperatures," *Project Squid,* Purdue University Foundation, Lafayette, IN, 1 May 1947.

14. Durst, F., Melling, A. and Whitelaw, J. H., *Principles and Practice of Laser-Doppler Anemometry,* Academic Press Inc., New York, NY, 1981.

15. Faeth, G. M. *Lectures in Laser-Doppler Anemometry,* The Pennsylvania State University, University Park, PA, 1984.

16. Nejad, A. S. and Davis, D. L., "Velocity Bias in Two-Component Individual Realization Laser Doppler Velocimetry," L.I.A. Vol. 58, ICALEO, 1986, pp. 78-88.

17. Anon., *Aerometrics Phase Doppler Particle Analyzer, Doppler Signal Analyzer, 2-Component Users Manual,* Release 1.0, Jan 93.

18. Dibble, R. W., Hartmann, V. and Schefer, R. W., "Conditional Sampling of Velocity and Scalars in Turbulent Flames Using Simultaneous LDV-Raman Scattering," Experiments in Fluids, Vol. 5, 1987, pp. 103-113.

19. Product No. GB-2000, Micro Abrasives Corp., Westfield, MA

20. Kennedy, I. M., "Some Aspects of Seeding Flames With Refractory Oxide Particles," Combustion Science and Technology, Vol. 27, 1982, pp. 247-252.

21. Rudoff, R. C. and Bachalo, W. D., "Seed Particle Response and Size Characterization in High Speed Flows", Laser Anemometry: Advances and Applications, Vol. 2, American Society of Mechanical Engineers, 1991, 443-447.

22. Menon, R. and Lai, W. T., "Key Considerations in the Selection of Seed Particles for LDV Measurements," Laser Anemometry: Advances and Applications, Vol. 2, American Society of Mechanical Engineers, 1991, 719-730.

23. Witze, P. O. and Baritaud, T. A., "Particle Seeding for Mie Scattering Measurements in Combusting Flows," Sandia Report SAND85-8912, Sandia National Laboratories, Albuquerque, NM, May 1986.

24. Self, S. A. and Whitelaw, J. H., "Laser Anemometry for Combustion Research," Combustion Science and Technology, Vol. 13, 1976, pp. 171-197.

25. Anon., *The Temperature Handbook, Vol. 28,* Omega Engineering Inc., Stamford, CT, 1992.

26. Richardson, Jr., T. F., *The Effects of Temperature, Fuel Concentration, and Fuel Molecular Structure on Soot Formation in Laminar Diffusion Flames,* Doctoral Thesis, The Pennsylvania State University, University Park, PA, May 1993.

27. MathCad Version 5.0, MathSoft Inc., Cambridge, MA, Jan 94.

28. Holman, J. P., *Heat Transfer,* McGraw-Hill Book Company, New York, NY, 1981.

29. McBride, B. J. and Gordon, S., *Computer Program for Calculation of Complex Chemical Equilibrium Compositions, Rocket Performance, Incident and Reflected Shocks, and Chapman-Jouget Detonations,* NASA Lewis Research Center, NASA SP-273, Interim Revision, Mar 76.

30. Personal communication with R. Nessin, Micro Abrasives Corp., Westfield, MA, 24 Mar 94.

31. Personal communication with Dr. R. Hogg, The Pennsylvania State University, University Park, PA, 27 Apr 94.

32. Glass, M. and Kennedy, I. M., "An Improved Seeding Method for High Temperature Laser Doppler Velocimetry," Combustion and Flame, Vol. 29, 1977, pp. 333-335.

33. Correspondence with M. Kanazawa, Sumitomo Chemical America, Inc., 9 May 94.

34. Personal communication with Dr. G. Messing, The Pennsylvania State University, University Park, PA, 6 May 94.

35. Correspondence with V. Caldwell, Aluminum Company of America, 9 May 94.

36. Schlichting, H., *Boundary Layer Theory, Seventh Edition,* New York: McGraw-Hill Book Company, 1979.

37. Kennedy, I. M. and Kent, J. H., "Measurements of a Conserved Scalar In Turbulent Jet Diffusion Flames," *Seventeenth Symposium (International) on Combustion,* The Combustion Institute, Pittsburgh, PA, 1979, pp. 279-287.

38. Starner, S. H. and Bilger, R. W., "Measurement of Scalar-Velocity Correlations in a Turbulent Diffusion Flame," *Eighteenth Symposium (International) on Combustion,* The Combustion Institute, Pittsburgh, PA, 1981, pp. 921-930.

39. Starner, S. H. and Bilger, R. W., "Joint Measurements of Velocity and Scalars in a Turbulent Diffusion Flame," *Twenty-First Symposium (International) on Combustion,* The Combustion Institute, Pittsburgh, PA, 1986, pp. 1569-1577.

40. Tennekes, H. and Lumley, J. L., *A First Course in Turbulence,* Cambridge, MA: The MIT Press, 1992.

41. McLaughlin, D. K. and Tiedermann, W. G., "Biasing Correction for Individual Realization of Laser Anemometer Measurements in Turbulent Flows," The Physics of Fluids, Vol. 16, 1973, pp. 2082-2088.

42. Winter, A. R., Graham, L. J. W., and Bremhorst, K., "Effects of Time Scales on Velocity Bias in LDA Measurements Using Sample and Hold Processing," Experiments in Fluids, Vol. 11, 1991, pp. 147-152.

43. Johnson, D. A., Modarress, D. and Owen, F. K., "An Experimental Verification of Laser-Velocimeter Sampling Bias and Its Correction," Journal of Fluids Engineering, Vol. 106, Mar 84, pp. 5-12.

44. Adams, E. W. and Eaton, J. K., "An LDA Study of the Backward-Facing Step Flow, Including the Effect of Velocity Bias," Journal of Fluids Engineering, Vol. 110, Sep 88, pp. 275-282.

45. Gould, R. D., Stevenson, W. H. and Thompson, H. D., "A Parametric Study of Statistical Velocity Bias," L. I. A. Vol. 58 ICALEO, 1986, pp. 89-96.

46. Edwards, R. V., "How Real Are Particle Bias Errors?," *Laser Velocimetry and Particle Sizing: Proceedings of the Third International Workshop On Laser Velocimetry*, Hemisphere Publishing Corp., New York, NY, 1979, pp. 79-85.

47. Giel, T. V. and Barnett, D. O., "Analytical and Experimental Study of Statistical Bias in Laser Velocimetry," *Laser Velocimetry and Particle Sizing: Proceedings of the Third International Workshop on Laser Velocimetry*, Hemisphere Publishing Corp., New York, NY, 1979, pp. 86-99.

48. Buchhave, P. and George, Jr., W. K., "Bias Corrections in Turbulence Measurements by the Laser Doppler Anemometer," *Laser Velocimetry and Particle Sizing: Proceedings of the Third International Workshop on Laser Velocimetry,* Hemisphere Publishing Corp., New York, NY, 1979, pp. 110-119.

49. Bogard, D. G. and Tiedermann, W. G., "Experimental Evaluation of Sampling Bias in Naturally Seeded Flows," *Laser Velocimetry and Particle Sizing: Proceedings of the Third International Workshop on Laser Velocimetry*, Hemisphere Publishing Corp., New York, NY, 1979, pp. 100-109.

50. Durão, D. F. G. and Whitelaw, J. H., "The Influence of Sampling Procedures on Velocity Bias in Turbulent Flows," Proceedings of the LDA-Symposium, Copenhagen, 1975, pp. 138-149.

51. Craig, R. R., Nejad, A. S., Hahn, E. Y. and Schwartzkopf, K. G., "Approach for Obtaining Unbiased Laser Doppler Velocimetry Data in Highly Turbulent Flows," Journal of Propulsion and Power, Vol. 2, Nov-Dec 86, pp. 541-545.

52. Simpson, R. L. and Chew, Y. T., "Measurements in Steady and Unsteady Separated Turbulent Boundary Layers," *Laser Velocimetry and Particle Sizing: Proceedings of the Third International Workshop On Laser Velocimetry*, Hemisphere Publishing Corp., New York, NY, 1979, pp. 179-196.

53. Foust, M., unpublished data, The Pennsylvania State University, University Park, PA, Sep 94.

54. Personal communication with technical representative, Omega Engineering, Inc., Stamford, CT, Nov 94.

55. Rahman, S. A., Pal, S. and Santoro, R. J., "Swirl Coaxial atomization: Cold-Flow and Hot-Fire Experiments," AIAA paper 95-0381, AIAA 33rd Aerospace Sciences Meeting and Exhibit, Reno, NV, 9-12 Jan 95.

56. Avallone, E. A. and Baumeister III, T., eds., *Mark's Standard Handbook for Mechanical Engineers, Ninth Edition*, McGraw-Hill Book Co., New York, NY, 1987.

57. Personal communication with Dr. M. D. Moser, The Pennsylvania State University, University Park, PA, Jan 95.

58. Perry, J. H., *Chemical Engineers Handbook*, McGraw-Hill, New York, NY, 1963.

59. Glass, M. and Kennedy, I. M., "An Improved Seeding Method for High Temperature Laser Doppler Velocimetry," Combustion and Flame, Vol. 29, 1977, pp. 333-335.

60. Personal communication with Dr. R. Santoro, The Pennsylvania State University, University Park, PA, 5 May 94.

APPENDIX

The following outlines the conditions under which velocity measurements were taken in Penn State's optically accessible rocket chamber under hot-fire conditions. Velocity measurements were taken from 22 Jun 1994 to 1 Jul 1994. A shear coaxial injector was used for these experiments with the oxidizer (gaseous oxygen) flowing through the inner post and the fuel (gaseous hydrogen) flowing through the annulus. This document lists the flow conditions for the velocity measurements in the file: LDVJUN94.DAT.

LDV data acquisition was taken during steady state chamber pressure, which typically was reached 1.0 seconds into the firing.

Pressures were sampled at 200 Hz and temperatures were sampled at 50 Hz during a rocket firing. Mean values for the pressures and temperatures were calculated for each individual firing during the time interval that velocity data acquisition occurred. These mean values were then averaged over all the firings and are given in the first column in the listing below. The equation used was:

$$Xmean = (X1 + X2 + \ldots + XN) / N$$

where X1, X2, ..., XN = mean value for each individual firing
N = total number of firings

The column ""stdA"" gives the standard deviation of the averaged values over all the runs. This represents the variation from firing to firing. The equation used was:

$$stdA = SQRT\{[(X1 - Xmean)^2 + (X2 - Xmean)^2 + \ldots + (XN - Xmean)^2] / N\}$$

where X1, X2, ..., XN = mean value for each individual firing
Xmean = mean value over all firings
N = total number of firings

The standard deviations for each individual firing were averaged over all the firings to give an average standard deviation for a firing. These are given in the column ""stdB."" This represents a variation from the mean value during a typical firing. The equations used were:

$$std\# = SQRT\{[(y1 - X\#)^2 + (y2 - X\#)^2 + \ldots + (yM - X\#)^2] / M\}$$

$$stdB = (std1 + std2 + \ldots + stdN) / N$$

where y1, y2, ..., yM = data point (i.e. P or T) for each

```
                              individual firing
              M  = total number of data points for
                   each individual firing
             X#  = mean value for firing #
              #  = Number of firing (1, 2, ..., N)
           std#  = standard deviation of value for firing #
              N  = total number of firings
```

The seed material used for measuring velocity in these
experiments was aluminum oxide particles with a nominal diameter
of 0.3 microns.

Chamber dimensions   -   279.4 mm long X 50.8 mm X 50.8 mm
                              (11.0 in. X 2.0 in. X 2.0 in.)
* Chamber length was measured from injector face to nozzle throat.

Dimensions for the   - Oxidizer : diameter :   1.778 mm (0.07in.)
critical orifices   :   Cd :   0.93
used for metering   - Fuel   : diameter :   1.778 mm (0.07in.)
the flows   :   Cd :   0.93

Injector dimensions   - Oxidizer post ID   :   7.747 mm (0.305in.)
                      - Fuel annulus ID   :   9.525 mm (0.375in.)
                      - Fuel annulus OD   :   12.70 mm (0.500in.)
                      - Oxidizer post recess :   0.00   mm

Nozzle dimensions   - Entrance angle   : 30 degrees
                      - Exit angle   : 15 degrees
                      - Entrance diameter   : 50.8 mm (2.0in.)
                      - Exit diameter   : 16.0 mm (0.631in.)
                      - Throat diameter   : 11.35 mm (0.447in.)
                      - Length   : 44.45 mm (1.75 in.)

Note : A transition section 25.4 mm (1.0 in.) in length, with
       a 50.8 mm (2.0 in.) square inlet which transitions smoothly
       to a 50.8mm (2.0 in.) diameter exit, preceded the nozzle
       providing a transition from the square combustion chamber to
       the circular nozzle entrance.

Below lists the averages over all runs:

                Oxidizer - gaseous oxygen   stdA   stdB
          Oxidizer Pressure - 7.36 MPa   0.060 MPa   0.035 MPa
       (upstream of orifice)   (1068 psia   9.1 psia   5.1 psia)
         Oxidizer Temperature - 304 K   2.1 K   0.67 K
       (upstream of orifice)   (88.3 F   3.8 F   1.2 F)
         Oxidizer Temperature - 303 K   2.9 K   1.2 K
            (in injector)   (86.0 F   5.2 F   2.2 F)
            Oxidizer flowrate - 0.03873 kg/s   0.00033 kg/s
```

|                                          |   |                   |            |            |
|------------------------------------------|---|-------------------|------------|------------|
|                                          |   | (0.0852 lbm/s     | 0.00073 lbm/s) |        |
| Oxidizer exit velocity                   | - | 52.8 m/s          | 7.67 m/s   |            |
|                                          |   | (173.2 ft/s       | 25.2 ft/s) |            |

|                                          |   |                   | stdA       | stdB       |
|------------------------------------------|---|-------------------|------------|------------|
| Fuel                                     | - | gaseous hydrogen  | stdA       | stdB       |
| Fuel Pressure                            | - | 7.32 MPa          | 0.051 MPa  | 0.104 MPa  |
| (upstream of orifice)                    |   | (1062 psia        | 7.5 psia   | 15.1 psia) |
| Fuel Temperature                         | - | 304 K             | 2.4 K      | 0.89 K     |
| (upstream of orifice)                    |   | (87.4 F           | 4.3 F      | 1.6 F)     |
| Fuel Temperature                         | - | 306 K             | 2.8 K      | 0.94 K     |
| (in injector)                            |   | (91.3 F           | 5.1 F      | 1.7 F)     |
| Fuel flowrate                            | - | 0.0103 kg/s       | 0.00008 kg/s |          |
|                                          |   | (0.0227 lbm/s     | 0.00018 lbm/s) |        |
| Fuel exit velocity                       | - | 184.6 m/s         | 4.66 m/s   |            |
|                                          |   | (605.6 ft/s       | 15.3 ft/s) |            |
| Chamber pressure                         | - | 1.28 MPa          | 0.031 MPa  | 0.014 MPa  |
|                                          |   | (185.5 psia       | 4.5 psia   | 2.0 psia)  |

Rocket firing duration  -  4 seconds total

- Start time for velocity          :  1.4 seconds
  data acquisition                       into rocket firing

- Stop time for velocity           :  3.9 seconds
  data acquisition                       into rocket firing

- Total duration for velocity      :  2.5 seconds
  data acquisition

The LDV data reported here were obtained in the optically accessible rocket from 22 Jun 1994 to 1 Jul 1994.  Radial positions are measured from the centerline of the combustion chamber and are incremented in the vertical direction.

The definitions used for the following table are:

$x$          -  axial position measured downstream from the injector face (mm)

$r$          -  radial position measured from the centerline of the combustion chamber (mm)

umean        -  mean velocity in the axial direction (m/s)

urms         -  rms velocity in the axial direction (m/s)

# runs       -  total number of rocket firings required to obtain total data count

total count  -  total number of measured data points

GO2/GH2 seed  -  marked with an ""X"" if seeded to obtain"
velocity measurements

| x | r | umean | urms | # runs | total coun | Seeding | |
| | | | | | | GO2 | GH2 |
|---|---|---|---|---|---|---|---|
| 1.6 | -4.19 | 33.8 | 8.0 | 1 | 63 | x | |
| 1.6 | -4.06 | 36.8 | 8.2 | 1 | 1087 | x | |
| 1.6 | -3.81 | 44.6 | 7.5 | 1 | 653 | x | |
| 1.6 | -3.56 | 50.1 | 7.5 | 1 | 716 | x | |
| 1.6 | -3.05 | 55.0 | 7.5 | 1 | 615 | x | |
| 1.6 | -2.54 | 58.1 | 7.4 | 1 | 633 | x | |
| 1.6 | -2.03 | 60.0 | 7.0 | 1 | 319 | x | |
| 1.6 | -1.52 | 60.1 | 8.5 | 1 | 384 | x | |
| 1.6 | -1.02 | 62.9 | 6.9 | 1 | 93 | x | |
| 1.6 | -0.51 | 62.9 | 6.7 | 1 | 299 | x | |
| 1.6 | 0.00 | 61.2 | 11.2 | 1 | 264 | x | |
| 1.6 | 0.51 | 62.3 | 7.6 | 1 | 733 | x | |
| 1.6 | 1.02 | 60.3 | 7.4 | 1 | 987 | x | |
| 1.6 | 1.52 | 58.5 | 7.2 | 1 | 407 | x | |
| 1.6 | 2.03 | 57.5 | 7.3 | 1 | 1084 | x | |
| 1.6 | 2.54 | 54.4 | 7.4 | 1 | 1096 | x | |
| 1.6 | 3.05 | 50.8 | 7.3 | 1 | 1064 | x | |
| 1.6 | 3.56 | 40.2 | 7.2 | 1 | 631 | x | |
| 1.6 | 3.68 | 35.2 | 7.5 | 1 | 501 | x | |
| 1.6 | 3.81 | 25.9 | 14.0 | 1 | 34 | x | |
| 1.6 | -11.43 | 0.4 | 1.2 | 1 | 5 | | x |
| 1.6 | -10.16 | -0.3 | 2.6 | 1 | 15 | | x |
| 1.6 | -8.89 | -1.1 | 1.9 | 1 | 203 | | x |
| 1.6 | -7.62 | 2.9 | 3.8 | 1 | 1132 | | x |
| 1.6 | -6.86 | 2.3 | 5.9 | 1 | 280 | | x |
| 1.6 | -6.60 | 10.3 | 10.0 | 1 | 611 | | x |
| 1.6 | -6.35 | 20.9 | 18.7 | 2 | 197 | | x |
| 1.6 | 6.10 | 5.0 | 4.5 | 1 | 51 | | x |
| 1.6 | 6.35 | 1.1 | 5.7 | 1 | 102 | | x |
| 1.6 | 6.86 | -1.1 | 1.8 | 1 | 72 | | x |
| 1.6 | 7.62 | 0.2 | 2.0 | 1 | 87 | | x |
| 1.6 | 8.89 | -0.5 | 1.6 | 1 | 93 | | x |
| 6.4 | -20.32 | -0.8 | 4.8 | 1 | 61 | | x |
| 6.4 | -19.05 | -0.4 | 4.6 | 1 | 96 | | x |
| 6.4 | -17.78 | -0.5 | 5.2 | 1 | 70 | | x |
| 6.4 | -16.51 | -0.8 | 5.0 | 1 | 107 | | x |
| 6.4 | -15.24 | -1.8 | 4.8 | 1 | 110 | | x |
| 6.4 | -13.97 | -0.5 | 4.4 | 1 | 295 | | x |
| 6.4 | -12.70 | -0.1 | 3.9 | 1 | 364 | | x |
| 6.4 | -11.43 | -0.3 | 5.1 | 1 | 92 | | x |
| 6.4 | -10.16 | 1.6 | 3.9 | 1 | 107 | | x |
| 6.4 | -8.89 | 4.9 | 7.2 | 1 | 320 | | x |
| 6.4 | -7.62 | 6.4 | 21.4 | 1 | 675 | | x |

| | | | | | | | |
|---|---|---|---|---|---|---|---|
| 6.4 | -6.86 | 20.5 | 29.0 | 1 | 231 | | x |
| 6.4 | -6.35 | 48.4 | 23.6 | 1 | 3687 | | x |
| 6.4 | -6.22 | 64.3 | 36.6 | 1 | 316 | | x |
| 6.4 | -6.10 | 142.9 | 55.7 | 1 | 220 | | x |
| 6.4 | -5.84 | 88.7 | 26.0 | 1 | 882 | | x |
| 6.4 | -5.72 | 174.4 | 49.8 | 1 | 189 | | x |
| 6.4 | -5.59 | 142.0 | 55.5 | 2 | 460 | | x |
| 6.4 | -5.46 | 141.7 | 50.8 | 1 | 304 | | x |
| 6.4 | -5.33 | 138.6 | 58.4 | 2 | 529 | | x |
| 6.4 | -5.21 | 174.5 | 49.4 | 1 | 299 | | x |
| 6.4 | -5.08 | 168.1 | 49.9 | 2 | 550 | | x |
| 6.4 | -4.95 | 137.4 | 51.0 | 2 | 369 | | x |
| 6.4 | -4.83 | 143.1 | 46.3 | 2 | 756 | | x |
| 6.4 | -4.57 | 113.9 | 43.7 | 1 | 93 | | x |
| 6.4 | -4.32 | 80.9 | 43.0 | 2 | 159 | | x |
| 6.4 | -4.06 | 41.6 | 6.7 | 1 | 9 | | x |
| 6.4 | 5.08 | 128.7 | 65.5 | 1 | 5 | | x |
| 6.4 | 5.33 | 175.2 | 47.0 | 1 | 155 | | x |
| 6.4 | 5.46 | 199.0 | 32.2 | 1 | 11 | | x |
| 6.4 | 5.59 | 175.9 | 49.4 | 1 | 114 | | x |
| 6.4 | 5.72 | 186.6 | 38.5 | 1 | 241 | | x |
| 6.4 | 5.84 | 147.2 | 72.1 | 1 | 102 | | x |
| 6.4 | 5.97 | 145.5 | 61.2 | 1 | 484 | | x |
| 6.4 | 6.10 | 113.4 | 71.2 | 1 | 85 | | x |
| 6.4 | 6.22 | 107.1 | 61.3 | 1 | 169 | | x |
| 6.4 | 6.35 | 62.2 | 59.3 | 1 | 31 | | x |
| 6.4 | 6.60 | 32.2 | 40.2 | 1 | 286 | | x |
| 6.4 | 6.86 | 24.5 | 28.9 | 1 | 361 | | x |
| 6.4 | 7.62 | 4.7 | 20.5 | 1 | 342 | | x |
| 6.4 | 8.89 | 1.7 | 4.9 | 1 | 22 | | x |
| 6.4 | -4.83 | 108.9 | 38.7 | 1 | 18 | x | |
| 6.4 | -4.57 | 93.7 | 29.6 | 1 | 73 | x | |
| 6.4 | -4.32 | 54.7 | 26.5 | 2 | 102 | x | |
| 6.4 | -4.06 | 41.6 | 18.9 | 1 | 1566 | x | |
| 6.4 | -3.81 | 39.8 | 14.8 | 1 | 7431 | x | |
| 6.4 | -3.18 | 47.0 | 16.5 | 1 | 8856 | x | |
| 6.4 | -2.54 | 52.2 | 15.9 | 1 | 6557 | x | |
| 6.4 | -1.91 | 56.6 | 17.1 | 1 | 9728 | x | |
| 6.4 | -1.27 | 57.4 | 14.8 | 1 | 14158 | x | |
| 6.4 | -0.64 | 58.9 | 15.3 | 1 | 15100 | x | |
| 6.4 | 0.00 | 59.5 | 16.8 | 1 | 13432 | x | |
| 6.4 | 0.64 | 59.0 | 12.3 | 1 | 2797 | x | |
| 6.4 | 1.27 | 58.5 | 15.9 | 1 | 3107 | x | |
| 6.4 | 1.91 | 56.0 | 12.8 | 1 | 8413 | x | |
| 6.4 | 2.54 | 53.4 | 15.5 | 1 | 6895 | x | |
| 6.4 | 3.18 | 47.6 | 13.4 | 1 | 6673 | x | |
| 6.4 | 3.81 | 40.8 | 18.4 | 1 | 3849 | x | |
| 6.4 | 4.06 | 38.4 | 14.2 | 1 | 3906 | x | |
| 6.4 | 4.32 | 41.3 | 14.6 | 1 | 601 | x | |
| 6.4 | 4.57 | 61.9 | 25.3 | 1 | 40 | x | |

| | | | | | | | |
|---|---|---|---|---|---|---|---|
| 12.7 | -24.13 | 0.0 | 2.3 | 1 | 2180 | | x |
| 12.7 | -22.86 | 1.6 | 2.5 | 1 | 78 | | x |
| 12.7 | -21.59 | 1.4 | 4.7 | 1 | 69 | | x |
| 12.7 | -20.32 | 0.1 | 4.5 | 1 | 66 | | x |
| 12.7 | -19.05 | 0.0 | 3.9 | 1 | 58 | | x |
| 12.7 | -17.78 | 0.4 | 3.3 | 1 | 115 | | x |
| 12.7 | -16.51 | -1.0 | 3.5 | 1 | 427 | | x |
| 12.7 | -15.24 | -0.5 | 5.3 | 1 | 151 | | x |
| 12.7 | -13.97 | 1.6 | 4.5 | 1 | 473 | | x |
| 12.7 | -12.70 | 0.5 | 4.3 | 1 | 592 | | x |
| 12.7 | -11.43 | 3.1 | 4.2 | 1 | 867 | | x |
| 12.7 | -10.16 | 3.6 | 5.5 | 1 | 2272 | | x |
| 12.7 | -8.89 | 10.7 | 11.4 | 1 | 3427 | | x |
| 12.7 | -8.26 | 17.1 | 14.2 | 1 | 4386 | | x |
| 12.7 | -7.62 | 40.1 | 26.4 | 1 | 1598 | | x |
| 12.7 | -6.99 | 60.9 | 23.7 | 1 | 1836 | | x |
| 12.7 | -6.35 | 98.7 | 40.5 | 1 | 654 | | x |
| 12.7 | -5.59 | 156.3 | 53.9 | 1 | 65 | | x |
| 12.7 | 5.08 | 120.0 | 33.1 | 1 | 16 | | x |
| 12.7 | 5.59 | 136.9 | 45.4 | 1 | 130 | | x |
| 12.7 | 6.35 | 82.8 | 32.3 | 1 | 401 | | x |
| 12.7 | 6.99 | 55.7 | 23.9 | 1 | 846 | | x |
| 12.7 | 7.62 | 34.5 | 22.6 | 1 | 1830 | | x |
| 12.7 | 8.26 | 18.5 | 15.8 | 1 | 2254 | | x |
| 12.7 | 8.89 | 9.5 | 10.5 | 1 | 2390 | | x |
| 12.7 | 10.16 | 3.3 | 5.2 | 1 | 902 | | x |
| 12.7 | -5.08 | 92.7 | 37.4 | 1 | 202 | x | |
| 12.7 | -4.83 | 67.2 | 31.9 | 1 | 829 | x | |
| 12.7 | -4.57 | 49.7 | 14.7 | 2 | 6255 | x | |
| 12.7 | -4.32 | 45.9 | 9.4 | 1 | 6114 | x | |
| 12.7 | -4.06 | 45.1 | 8.7 | 1 | 11783 | x | |
| 12.7 | -3.81 | 46.3 | 8.2 | 1 | 10700 | x | |
| 12.7 | -3.23 | 50.4 | 8.2 | 1 | 9471 | x | |
| 12.7 | -2.54 | 55.0 | 8.2 | 1 | 14035 | x | |
| 12.7 | -1.91 | 56.8 | 8.1 | 1 | 12123 | x | |
| 12.7 | -1.27 | 58.9 | 8.0 | 1 | 7826 | x | |
| 12.7 | -0.64 | 59.3 | 7.7 | 1 | 10265 | x | |
| 12.7 | 0.00 | 59.6 | 7.7 | 1 | 9624 | x | |
| 12.7 | 0.64 | 59.8 | 8.1 | 1 | 8306 | x | |
| 12.7 | 1.27 | 58.4 | 8.4 | 1 | 7169 | x | |
| 12.7 | 1.91 | 55.7 | 8.7 | 1 | 5418 | x | |
| 12.7 | 2.54 | 52.1 | 8.8 | 1 | 5766 | x | |
| 12.7 | 3.18 | 49.1 | 10.2 | 1 | 1190 | x | |
| 12.7 | 3.81 | 44.0 | 9.0 | 1 | 2662 | x | |
| 12.7 | 4.06 | 46.1 | 11.3 | 1 | 2275 | x | |
| 12.7 | 4.33 | 62.7 | 29.9 | 1 | 822 | x | |
| 12.7 | 4.57 | 93.2 | 30.6 | 1 | 489 | x | |
| 12.7 | 4.83 | 47.0 | 11.2 | 1 | 14 | x | |